1-1-2019

Digital Image Processing And Metabolic Parameter Linearity To Noninvasively Detect Analyte Concentration

Joseph Allen Jr

DIGITAL IMAGE PROCESSING AND METABOLIC PARAMETER LINEARITY TO NON-INVASIVELY DETECT ANALYTE CONCENTRATION

by

Joseph David Allen, Jr.
Bachelor of Arts, University of North Dakota, 2010

A Thesis
Submitted to the Graduate Faculty

of the

University of North Dakota

in partial fulfillment of the requirements

for the degree of

Master of Science

Grand Forks, North Dakota

May
2019

This thesis, submitted by Joseph D. Allen, Jr. in partial fulfillment of the requirements for the Degree of Master of Science from the University of North Dakota, has been read by the Faculty Advisory Committee under whom the work has been done and is hereby approved.

S. Noghanian
Sima Noghanian, PhD

Reza Fazel-Rezai
Reza Fazel-Rezai, PhD

Eric Johnson, MD

Ivan T. Lima Jr.
Ivan Lima, PhD

This thesis is being submitted by the appointed advisory committee as having met all of the requirements of the School of Graduate Studies at the University of North Dakota and is hereby approved.

Chris Nelson
Dean of the School of Graduate Studies

4/16/19
Date

PERMISSION

Title Digital Image Processing and Metabolic Parameter Linearity to Non-Invasively Detect Analyte Concentration

Department Biomedical Engineering

Degree Master of Science

In presenting this thesis in partial fulfillment of the requirements for a graduate degree from the University of North Dakota, I agree that the library of this University shall make it freely available for inspection. I further agree that permission for extensive copying for scholarly purposes may be granted by the professor who supervised my thesis work or, in his absence, by the Chairperson of the department or the dean of the School of Graduate Studies. It is understood that any copying or publication or other use of this thesis or part thereof for financial gain shall not be allowed without my written permission. It is also understood that due recognition shall be given to me and to the University of North Dakota in any scholarly use which may be made of any material in my thesis.

Joseph D. Allen, Jr.
April 22, 2019

TABLE OF CONTENTS

LIST OF FIGURES

LIST OF TABLES

ACKNOWLEDGMENTS

I wish to express my sincere appreciation to my advisor Dr. Sima Noghanian and the members of my advisory Committee for their guidance and support during my time in the master's program at the University of North Dakota. I also thank my professor Dr. Reza Fazel-Rezai for his guidance with regards to the technical aspect of the device development. I would also like to thank Mr. Dave Molmen, Dr. Jon Allen, Dr. Rashid Ahmed, Dr. Eric Johnson, Altru Health System Research Center personnel, and the volunteers who participated in the clinical trial for their assistance during the project. Funding for this research was provided by the North Dakota Department of Commerce.

This thesis is dedicated to my mother and father, Yolanda and Dr. Joseph Allen, Sr.

ABSTRACT

Spectroscopy is the scientific technique of quantifying and measuring electromagnetic, or light, reflectance or absorption. Atoms emit and/or absorb light when light passes through. The excitations provide specific energy signatures that relate to the element that is emitting or absorbing the light. Non-invasive biosensors monitor physical health properties such as heart rate, oxygen saturation, and tissue blood flow as a result of spectroscopy. Several attempts have been made to non-invasively detect metabolic chemical, or analyte, concentration with various spectroscopic techniques. The primary limitation is due to signal-to-noise ratio. This research focuses on a unique method that combines emission spectroscopy and machine learning to non-invasively detect glucose and other metabolic analyte concentrations. Artificial neural network is applied to train a predictive model that enables the remote sensing capability. The data acquisition requires capturing digital images of the spectral reflectance. Image processing and segmentation determines discrete variables that correlate with the metabolic analytes. The clinical trial protocol includes n=90 subjects, and a venipuncture comprehensive metabolic panel blood test within two minutes prior to a non-invasive spectral reading. Results indicate a strong correlation between the spectral system and the clinical gold standard, relative to metabolic analyte concentration.

1. INTRODUCTION

Non-invasive (NI) biosensor devices offer promise for continuously monitoring a subject's health [1]. The technological advancement aims to provide greater efficiency in the delivery of quality health care. Currently, NI health monitoring solutions integrate an optical sensor to detect physical parameters (e.g. heart rate) and tests such as an electrocardiogram (ECG). The optical sensor beams a light through the skin, which some of the light is absorbed. Changes in the portion of light that is reflected back to the sensor returns the information for interpretation, a process known as photo plethysmography (PPG). Advances in complimentary technology (i.e., digital signal processing and machine learning), resulting from an increase in computing power, enable the optical sensor technology to be scaled down to the size of a wrist watch for the purpose of tracking certain physical health and fitness parameters. The advancement also opens avenues for diverse biomedical sensor applications [2, 3]. This research aims to expand the NI detection capability to the 14 health parameters found in a comprehensive metabolic panel (CMP) clinical blood test. The CMP test measurers blood sugar (i.e. glucose) level, electrolyte and fluid balance, kidney function, and liver function. The CMP test is routinely preformed to assess overall health, diagnose, and guide treatment of numerous diseases. The CMP blood test is the second most reimbursed blood test in the United States with over 40 million tests performed in 2015, based on Medicare payments [4, 5, 6]. This thesis focuses on combining optical sensor technology with machine learning to enable the NI detection capability of a CMP blood test.

1.1 *Motivation*

Given the aging population, wearable and NI biomedical monitoring applications are in demand [7]. NI point-of-care health monitoring leads to convenient and timely access to vital information that is important in the diagnostic decision-making process. The applications, or effects, of this type of technological advancement in medicine include remote health monitoring, early detection, and increase compliance activity; therefore, potentially curbing the rising cost of healthcare [8]. More importantly, the innovation can positively impact patient lives.

Today, the CMP blood test requires drawing a vial of blood to conduct the analysis. This venipuncture method poses a challenge in the case of neonatal, elderly, and hemophobic patients. Moreover, the NI solution is of particular interest because the application enables continuous monitoring of the subject's health status. For example, diabetes management requires regular glucose monitoring to maintain optimal health. Monitoring drug efficacy is another area in which continuous measurements is of great importance.

Real-time vital information, as a result of NI health monitoring, allows individuals to change their lifestyle to maintain optimal health status. NI chemical sensors, unlike physical sensors for monitoring vital-signs (e.g., heart rate, ECG, etc.), are still in their infancy. Electrochemical biosensors detect electrolytes and metabolites in sweat, tears, or saliva through the use of transducers. Several optical techniques (e.g., Raman spectroscopy, near/mid-infrared absorption, and florescence) have been attempted to detect metabolic analytes [9, 10]. Previous attempts involving optical techniques to detect metabolic chemistry levels fail to generate reliable results however. The challenge in developing a NI optical biosensor capable of detecting human biological chemistry includes identifying significant predictors that relate to the imaging technique and the metabolic analytes of interest to develop a reliable model. Our focus in this thesis is the

development of a novel NI optical imaging clinical blood testing application capable of detecting the concentration of metabolic chemistry analytes.

1.2 *Thesis Outline*

1.2.1 *Chapter 2: Literature Review*

In this chapter, we introduce previous non-invasive analyte, particularly glucose, concentration detection methods. The significance, causes of failure with respect to unsuccessful previous attempts, and the differentiating factors relating to prior attempts and the current method are described. This section also provides background information pertaining to the innovative machine learning approach, image processing, and statistical analysis to substantiate and validate the device development.

1.2.2 *Chapter 3: Materials and Procedure*

This chapter discusses the custom hardware, software, and clinical trial relating to the NI CMP (NICMP) device. It provides an overview of the Institutional Review Board (IRB) approved protocol to cross-validate the NI device against the standard venipuncture CMP test. This section also describes the specific machine learning technique to develop the predictive model to enable the NI feature. Moreover, this section discusses the binary image thresholding and conversion process necessary to analyze the fundamental aspect by determining the underlying error distribution.

1.2.3 *Chapter 4: Results*

This chapter provides a summary of the NICMP predictive model results, including mean squared error, correlation, covariance, and correlation coefficient. Additionally, the predictive model coefficient of determination generalizes the overall correlation, relative to the venipuncture method. Graphical representation of the results with respect to each metabolic parameter are available in this section. This section also provides the analysis relating to the binary image, or underlying, error distribution.

1.2.4 *Chapter 5: Discussion*

This chapter interprets the statistical analysis of the NICMP device. The section discusses the accuracy of the NICMP predictive model, underlying error distribution, and the relationship between the CMP analyte concentrations and certain biological factors.

1.2.5 *Chapter 6: Conclusion*

This section provides the study outcome, and further considerations regarding the NICMP predictive model development. It outlays enhancements to potentially increase the device reliability and accuracy. Finally, this chapter also discusses the NICMP limitations.

2. LITERATURE REVIEW

2.1 *Previous Non-Invasive Analyte (Glucose) Monitoring Attempts*

NI analyte monitoring has been attempted through several different methods throughout the years. This section will have an emphasis on the glucose analyte. This particular analyte is important in mitigating diabetes mellitus. Diabetes is considered a pandemic and affects approximately 8.3% of the world's population, or 380 million people. This figure is anticipated to rise to 592 million people by 2035 [11]. Diabetes is a medical condition that occurs when an individual's glucose, or blood sugar, is too high. The pancreas is responsible for producing the insulin hormone. Insulin helps the glucose from food enter your cells and convert it into energy. The common types of diabetes are type 1, type 2, and gestational diabetes. Type 1 diabetes occurs when your body does not produce insulin, and usually is diagnosed in children and young adults. This is a result of the immune system attacking and destroying cells in the pancreas that make insulin. Type 2 diabetes occurs when your body does not make or use insulin well. Type 2 diabetes most commonly affects middle-aged and older people, and is the most common type of diabetes. Both type 1 and type 2 diabetes can affect individuals at any age however. Gestational diabetes affects some women during pregnancy. This type of diabetes usually goes away after the baby is born. Women with gestational diabetes have a greater chance of developing type 2 diabetes later in life [12]. Individuals diagnosed with diabetes must closely monitor the prevalent chronic disease by controlling glucose level to mitigate severe health risk. Current methods to control blood glucose and assist with insulin intervention include venipuncture, finger-stick, and invasive continuous glucose monitoring devices.

2.1.1 *Methods Attempted*

Electrochemical transducers dominate the role in clinical diagnostics. This technology enables hand-held analyzers to detect metabolic analytes. These sensors rely on blood samples, which inhibits diverse biomedical applications. This presents an opportunity for clinical translation of NI systems to address unmet clinical needs [13].

Glucose can be found in different parts of the body, including interstitial fluid, saliva, tears, urine, and sweat. Several attempts have been made to detect glucose with NI biosensors through these mediums [14]. Figure 1 summarizes the various NI glucose measurement techniques that have been investigated. We will focus on NI optical techniques for the purpose of comparison. Commercial attempts to develop an optical NI glucose monitor include Raman spectroscopy, near-infrared (NIR) spectroscopy, and radio wave spectroscopy.

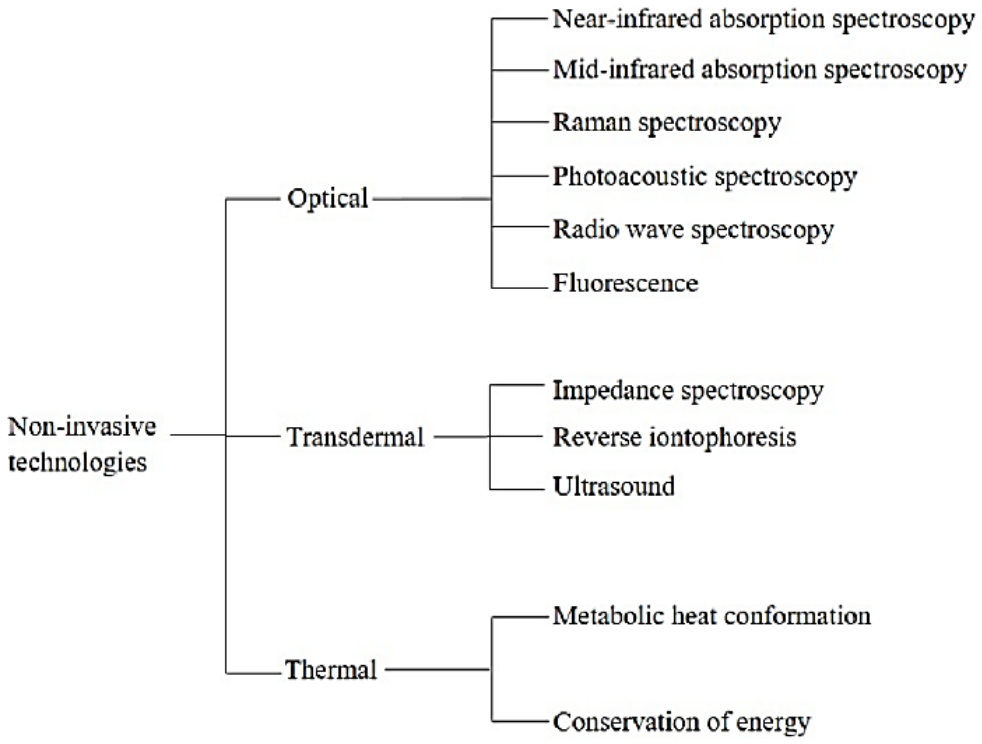

Figure 1. Blood Glucose Measurement Techniques [10]

The basis of Raman spectroscopy is on the detection of scattering light resulting from the rotation of molecules interacting with a laser. The vibration and rotation of a molecule correlates to its concentration. Raman bands between 8,333 nm to 11,111 nm are specific to glucose *in vitro* [15]. Animal models *in vivo* prove good correlation with respect to glucose concentration mainly on the eye [16, 17]. Raman spectroscopy on humans indicate 92% of the values within the A and B zones of the Clarke Error Grid, suggesting potential clinical usefulness. (95% of values should be within zone A, and no more than 5% of the values in zone B to be clinically acceptable.) Limitations concerning lipid structure on human skin causes different results however. Better calibration and mathematical models are necessary to eliminate the limitations due to other compounds. The approach is impractical due to the size of the device and its limitations [18].

NIR spectroscopy concept involves transmitting a band of NIR light through a vascular area (finger, ear, tongue, etc.). Certain calculations provide glucose concentration *in vivo* from the information obtained at the receiver [19, 20]. Producing corresponding glucose measurements is done by combining the NIR spectroscopy technique with certain multivariate analysis techniques. In fact, this method produces glucose measurements in complex biological matrices and synthetic mixtures [21, 22, 23]. The NIR spectroscopy method through the skin has been unsuccessful due to sensitivity concerns, and environmental variations that result in a number of factors that interfere with the glucose measurements however [24].

The radio wave spectroscopy method entails transmitting a low-powered radio signal through the area between the thumb and forefinger via two facing patch antennas. The permittivity changes across the signal transmission path depends on analyte concentration. The sensing system operates at 60 GHz on the millimeter wave band to function as a spectroscopic method for material characterization. One unique feature is the ability for this method to detect very low levels of

glucose. It can detect glucose concentration in controlled water-based samples as low as 24.42 mg/dL, and 72.07 mg/dL in humans. This method is currently still in development [25].

The spectroscopy approach to generating a signal with either a laser or LED light source in the visible to NIR frequency range for analysis with respect to certain physical health parameters is clinically proven. The approach generates a reliable application to remotely detect physical health parameters such as heart rate, blood pressure, and oxygen saturation by PPG processing. Clinical PPG systems to monitor certain vital signs normally require direct contact with the skin in the form of a finger clip. An evolutionary version of the spectroscopic PPG has been developed to function without direct contact with the tissue through a camera-based imaging approach [26]. This particular advancement indicates the versatility of spectroscopy. Furthermore, it validates the image-based method of data acquisition for the purpose of developing a NICPM biosensor. It is clear why researchers have attempted to detect glucose analyte concentration with spectroscopy. The technology has proven useful in providing NI, continuous, and real-time measurement of arterial pressure with infrared light transmitted through a finger. Implementing the aforementioned technology to detect analyte concentration poses a challenge however. The attempts involving spectroscopy have come close by identifying correlations, with respect to glucose concentration, in various biological compartments through different spectroscopic techniques (i.e., absorption, transmission, and reflectance) and wavelengths.

2.1.2 *Primary Cause of Failure*

The main reason for the unsuccessful attempts is particularly due to unfavorable signal-to-noise ratio (SNR) [27]. The SNR issues with regards to NI optical methods are primarily due to environmental factors including body temperature, skin moisture, skin thickness and motion. These factors cause interference with the excitation path of the light in an optical system [28]. One application combined three physical properties to develop a multi-sensor unit, which includes ultrasound, conductivity, and heat capacity. This multi-sensor approach increased sensitivity by simultaneously activating each sensor, reducing the contribution of noise, to improve the SNR. This particular method performs better than several previous NI approaches and attempts [29]. Research suggests that advancements in transducers and de-noising algorithms can overcome the challenges in the development of a NI optical glucose analyte measurement instrument.

The development of a NICMP involving reflectance spectroscopy through imaging aims to provide a discrete signal for analysis. The common theme relative to previous NI attempts include measurements relating to coefficients from various spectroscopic approaches (e.g., heat, ultrasound, NIR transmission, etc.). The method herein involves capturing images of laser reflectance with a CCD or complementary metal-oxide semiconductor photo (CMOS) detector. These type of image sensors convert light into electrons. This particular optical approach allows identifying variables that are discrete, and significantly correlate with various analyte concentration. The digital images, as a result of capturing laser reflectance with a CCD or CMOS photo detector, provide discrete intensity values between 0 and 255, relative to certain features. The discrete values are computed as the input variables, or predictors, in machine learning analysis to generate an algorithm, or predictive model, to detect glucose and other metabolic analyte concentration. The primary objective of this method is to address the problem concerning SNR.

2.2 *Laser Speckle Contrast Imaging*

2.2.1 *Background*

Spectroscopy is an integral part in the development of most fundamental theories, including physics and quantum mechanics. Because its techniques are extremely sensitive, spectroscopy is also applicable in several science and technology fields [30]. Because of the research of spectra in different chemical elements in flames, we know each element produces a set of certain characteristics. Thus, spectra can help identify individual elements. For example, astronomers apply spectroscopy to determine the chemical composition of matter (e.g., stars and planets) in the universe [31, 32]. Another application is magnetic resonance spectroscopy (MRS), and magnetic resonance imaging (MRI). MRS provides an analysis relating to the concentrations of different chemical components within a tissue such as hydrogen ions or protons. MRI provides an anatomic image of the brain to detect the location of a tumor. These particular spectroscopic techniques include a magnet and radio waves to enable the non-invasive analysis [33]. We will focus on optical (i.e., visible light and NIR) spectroscopy, and its clinical application. This NICMP research involves applying machine learning to optical spectroscopy, and training a predictive model for future analysis. This optical spectroscopy approach is an emission, or reflectance, application that detects the reflecting spectral flux with a photo detector. Currently, NIR optical spectroscopy provides a clinical tool to non-invasively monitor microvascular perfusion, or tissue blood flow. Techniques such as Laser-Doppler Flowmetry (LDF), Scanning Laser Doppler Imaging (SLDI), and Laser Speckle Contrast Imaging (LSCI) represent the evolution of optical emission spectroscopy with respect to its NI clinical application to continuously monitor microvascular perfusion.

2.2.2 *Emission Spectroscopic Techniques*

LDF utilizes the Doppler shift principle. It is a reliable and accurate method to measure the total microcirculation changes in tissue. A low power laser light is led by an optical fiber to a measuring head, or probe, that beams the laser light through the tissue. The light reflects off the red blood cells (RBC) and the frequency changes as a result of the moving objects (i.e. RBC). Hence, the light undergoes a Doppler shift. Measuring depth depends on the wavelength, and on the distance between the illumination source and the detector. Surrounding tissue also reflects the laser light. This particular reflectance is unshifted however. The illumination reflectance includes an unshifted light and a Doppler signal. Moreover, the magnitude of Doppler shift is a function of the number of moving RBC and their velocity. LDF is also applicable in early determination of burn depth [34, 35].

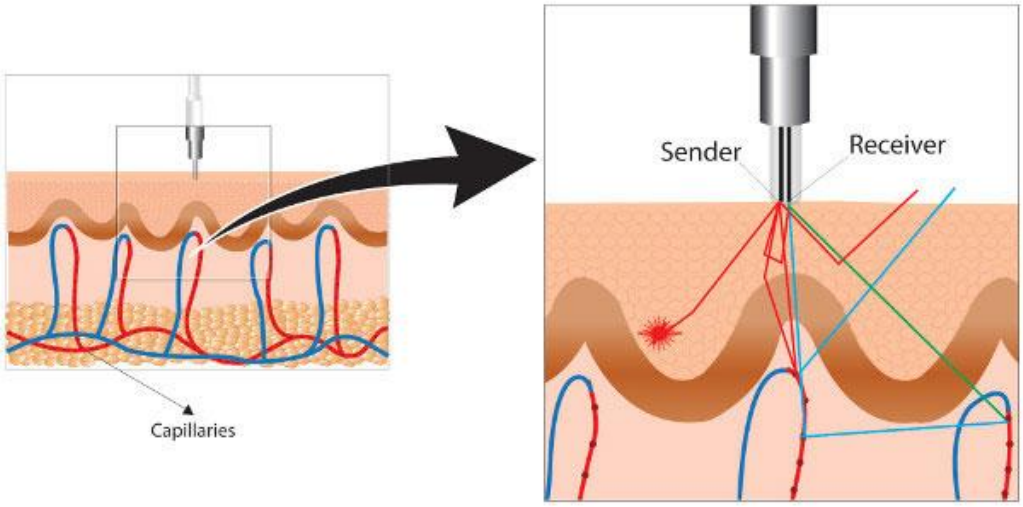

Figure 2. LDF probe and blood capillaries [43]

SLDI performs a high-definition topography that involves LDF scanning an area of tissue. This particular scanning method provides a real-time full field technique to assess microvascular perfusion. SLDI allows continuous videos of perfusion to be acquired while covering a wide area, relative to LDF, coherence tomography, and photo-acoustic tomography. SLDI also enables monitoring microvascular perfusion in the retina. It is a sensitive, proven, and reliable method to assess microvascular related health issues [36, 37].

LSCI provides a microvascular perfusion visualization method that combines high resolution and speed, based on the principle of LDF. LCSI generates an interference, or speckle, pattern by illuminating the tissue and capturing the changes of backscattered light overtime. The contrast between the static and dynamic interference, or unshifted and Doppler shift respectively, is known as speckle contrast. The contrast is the ratio between the standard deviation of intensity and the mean of the intensity. LCSI provides a method which produces excellent spatial and temporal resolution. Similar to SLDI, LSCI can detect RBC relative mean velocity and concentration. The main difference between SLDI and LSCI is that LSCI is faster at producing the results [38, 39]. Moreover, M. Roustit el al research findings outlay the inter-day reproducibility of post-occlusive reactive hyperemia (PORH) and local thermal hyperemia (LTH) performance by LDF, SLDI, and LSCI. The researcher experiments also gauges whether microcirculatory assessment by LDF and LSCI correlate to each other. Reproducibility of PORH is better with LSCI than LDF. Inter-day reproducibility of LTH is better with LSCI or SLDI than LDF. LSCI technique produces very good inter-day reproducibility for assessing PORH and LTH. Additionally, LSCI significantly correlates with single-point LDF for PORH [40]. This research indicates that LSCI is a reliable method of determining microvascular reactivity, given different conditions (i.e., post-

occlusion and heat). The NICMP development involves applying digital image processing and machine learning to LSCI technique to determine analyte concentration.

2.2.3 *Equipment*

The equipment to perform NI microvascular monitoring requires an illumination light source such as a laser in the red or NIR radiation spectrum, a photo detector (i.e. camera) to capture the reflectance, and software to display the perfusion activity. Illuminating the skin surface with a laser is considered safe. In fact, laser illumination in the red frequency range induces cell healing. Research determines that cells irradiated with 5 J/cm2 at 632.8 nm shows complete wound closure, and an increase in viability and basic fibroblast growth factor expression. It is important to note that not all wavelengths or combination of multiple wavelengths, nor dosage, produce similar results. Different wavelengths, combinations, and energy dosage can cause a negative effect with respect to cell healing [41]. In addition to red laser illumination inducing cell healing, another unique aspect of LSCI is its ability to perform consistently with different equipment grades. For example, a consumer-grade webcam can be used as the photo detector to visualize microvascular perfusion. Thus, inexpensive instrumentation can be used to image microcirculatory flows with accuracy comparable to a traditional LSCI system. The accuracy of a webcam against a high performance monochrome CCD camera indicates excellent agreement both *in vitro* and *in vivo* [42].

2.2.4 *Advantages of Laser Speckle Contrast Imaging*

LSCI offers an *in vivo* evaluation of microcirculation by coherent light scattering. Moreover, LSCI measures blood perfusion within the skin by evaluating the dynamics of the laser speckle pattern. The laser beam forms a spot on the skin with a diameter of approximately 1.5 mm,

and penetrates the skin. Part of the light is scattered back to the surface by the RBC in the capillaries [43]. Investigations in patients with leg ulcers show that measurements in open wounds utilizing LSCI technique is practical, and the ability to define different degrees of burns. The main benefits of spectroscopy and its LSCI application includes reliable NI monitoring of microvascular RBC relative volume and perfusion velocity, nonscanning full-field detection, and a consistent Doppler signal during burn wound scenarios. The nonscanning feature enables the analysis with a single target area which eliminates the need to scan an area of tissue to capture the data. The burn wound analysis indicates that the Doppler signal is consistent, given different textures, artifacts, or obtrusions on the skin surface that could potentially obscure the signal, because detection of different degrees of burns and depth is plausible. This raises the research question, can LSCI and statistical methods remotely detect and predict metabolic analyte concentration?

2.3 *Digital Image Processing and Machine Learning*

2.3.1 *Background*

Image processing with regards to the digital images that represent laser emission reflectance is necessary to 1) quantify image intensity features, and 2) analyze the underlying linearity between certain image characteristics and metabolic analyte concentration. Image segmentation (i.e. feature extraction) and binary threshold conversion are the image processing techniques relevant to the NICMP research. A Gray Level Co-Occurrence Matrix (GLCM) extracts and quantifies certain image feature values from the reflectance images which describe the image. Moreover, the GLCM analysis provides the input variables and their corresponding image intensity values for the predictive model development. Secondarily, the original reflectance images are gray scale. The digital images require conversion to their binary equivalent to assess the correlation on a fundamental level. The binary conversion technique involves applying certain thresholds to

convert the individual gray scale pixel values to either 1 or 0. The threshold techniques include adaptive, Otsu, and averaging thresholds. These particular threshold techniques are useful to convert the original spectral grayscale image intensity to binary values. This procedure enables assessing the underlying linearity between the binary image values and metabolic analyte concentration. Additionally, digital image processing is typically relevant to improve image data by removing unwanted distortions, and/or by enhancing image features for further processing. For example, pre-processing methods include pixel brightness enhancement, geometric transformations, and image restoration using knowledge about the entire image. Other image pre-processing methods exist. Because this NICMP research involves the development of a proof-of-concept device version, the image processing methods (i.e., segmentation and conversion) considers the raw images, thus pre-processing methods are not applied.

The predictive modeling approach involves a technique referred to as classification, which is a type of supervised machine learning. The process of classification in machine learning involves training an algorithm with externally supplied instances (i.e., predictor or feature data) and corresponding responses to make predictions about future instances. Machine learning consists of several different types of classification algorithms. The type of algorithm relevant to the NICMP research is the artificial neural network (ANN). ANN gathers knowledge by detecting the patterns and relationships in data. This process is also known as pattern recognition, or prediction [44].

2.3.2 *Digital Image Processing*

Research indicates that grayscale textural-features are good input, or predictor, variables in a broad range of image-classification applications [45]. GLCM enables the measurement of texture of an image. The GLCM calculates how often pairs of pixel with specific values and in a

specified spatial relationship occur in an image to extract statistical measures from the matrix. The NI imaging device incorporates a LABVIEW developer toolkit to perform a texture analyses utilizing GLCM function to quantify the texture features of the grayscale reflectance images. This process allows the quantification of certain texture features, and generate numeric values that describe the reflectance image texture. Given $\boldsymbol{P}(\boldsymbol{i},\boldsymbol{j})$ is the operator, or matrix of relative frequencies, each $(i,j)^{th}$ entry in the matrix represents the probability of transferring from one pixel with a gray level of i^n to another with a grey level of j^n under a preordained distance and angle. Specifically, the digital image process requires initially normalizing the GLCM to extract the numerical values that represent the texture features, or Haralick values. Normalizing procedures requires certain computations, given the following definitions:

$\boldsymbol{N_g}$ is the number of distinct gray levels in the image post-quantization. $\boldsymbol{p_x}$ and $\boldsymbol{p_y}$ are the i-th and j-th entry in the marginal-probability matrix obtained by summing the rows and columns of $p(i,j)$, respectively.

$$p_x(i) = \sum_{j=1}^{N_g} \quad p(i,j) \tag{1}$$

$$p_y(j) = \sum_{i=1}^{N_g} p_y(j) = \sum_{i=1}^{N_g} \quad p(i,j)\, p(i,j) \tag{2}$$

$$p_{x+y}(k) = \sum_{i=1}^{N_g} \quad \sum_{j=1}^{N_g} \quad \delta_{i+j,k} p(i,j), k = 2,3,\ldots,2N_g \tag{3}$$

$$p_{x-y}(k) = \sum_{i=1}^{N_g} \quad \sum_{j=1}^{N_g} \quad \delta_{|i-j|,k} p(i,j), k = 0,1,\ldots,N_g - 1 \tag{4}$$

where the Kronecker delta function $\delta_{m,n}$ is defined by

$$\delta_{m,n} = \begin{cases} 1 & \text{when } m = n \\ 0 & \text{when } m \neq n \end{cases} \tag{5}$$

Subsequently, normalizing procedures require the following operations:

Sum all elements, or neighboring resolution cell pairs, of the co-occurrence frequency matrix to formulate the normalizing constant.

$$R = \sum_{i=1}^{N_g} \quad \sum_{j=1}^{N_g} \quad P(i,j) \tag{6}$$

Normalize the frequency matrix to probabilities by dividing each cell by **R** to generate the (i,j)th entry in the normalized gray-tone spatial dependence matrix.

$$p(i,j) = \frac{P(i,j)}{R} \tag{7}$$

Post-normalization, the relevant Haralick value extraction computations are as follows:

Angular Second Moment or Energy, f_1, is a measure of the sum of squared elements in the GLCM.

$$f_1 = \sum_{i=1}^{N_g} \quad \sum_{j=1}^{N_g} (\frac{P(i,j)}{R})^2 = \sum_i \quad \sum_j \quad p(i,j)^2 \tag{8}$$

The contrast, f_2, is the difference moment of the P matrix and is a measure of the contrast or the amount of local variations present in the image.

$$f_2 = \sum_{k=0}^{N_g-1} \quad k^2\{\sum_{i=1}^{N_g} \quad \sum_{j=1}^{N_g} \quad \delta_{|i-j|,k} p(i,j)\} = \sum_{k=0}^{N_g-1} \quad k^2 p_{x-y}(k) \tag{9}$$

Correlation, f_3, measures the linear dependency, or joint probability, of gray levels of neighboring pixels.

$$f_3 = \frac{\sum_{i=1}^{N_g} \quad \sum_{j=1}^{N_g} \quad (ij)p(i,j) - \mu_x \mu_y}{\sigma_x \sigma_y} \tag{10}$$

where μ_x, μ_y, σ_x, σ_y are the means and standard deviations of p_x and p_y

Entropy, f_4, gives a measure of complexity of the image. Complex texture values tend to have higher entropy.

$$f_4 = -\sum_{i=1}^{N_g} \quad \sum_{j=1}^{N_g} \quad p(i,j)\log(p(i,j)) \tag{11}$$

Homogeneity, f_5, measurers the closeness of the distribution of elements in the GLCM to the GLCM diagonal.

$$f_5 = \sum_{\mathrm{i,j}} \frac{\mathrm{p(i,j)}}{1+|\mathrm{i}-\mathrm{j}|} \tag{12}$$

Standard deviation, σ, measurers the dispersion of the data set relative to its mean.

$$\sigma^2 = \sum_{i=0}^{n-1} \frac{(x_i - \mu)^2}{w} \quad (13)$$

where **x** is the input sequence, σ^2 is the variance, μ is the mean, and *w* is *n* when weighting is set to population and (*n*-1) when weighting is set to sample [46].

Texture feature extraction is necessary to quantify the grayscale images to provide input values for predictive modeling, and thus enable the NI detection capability. The second digital image processing technique includes binary conversion. This method is essential to convert the grayscale reflectance images to binary images. The purpose of the conversion process is to assess the underlying error distribution between binary image values and analyte concentration on a fundamental level. The image intensity values as a result of the GLCM analysis provide numeric values that represent certain pixel relationships, given individual pixel intensity values. Thus, the GLCM analysis is a function of image intensity values. The binary conversion involves applying certain thresholds to convert the grayscale image to binary and assess the linearity with a basic method of determining the image value. The three threshold techniques including adaptive, average, and Otsu to binarize the image. The adaptive approach uses first-order statistics to choose the threshold based on the local mean intensity in the neighborhood of each pixel [47]. The averaging method requires calculating the sum of grayscale intensity values and dividing the amount by the total number of pixels in the image to determine the threshold value. The Otsu's methods minimizes the intraclass variance of the black and white pixels by computing a global threshold from histogram counts [48].

2.3.3 *Artificial Neural Network*

ANN and artificial intelligence (AI) simulate the way the human brain works by connecting thousands of processing elements. This is similar to the neural structure of the brain, which

contains approximately 100 billion neurons. The human brain is an excellent classification and prediction tool. It learns patterns through experience, and has the ability to recognize objects as a result. AI is not as powerful as the human brain when it comes to pattern recognition because the brain has many more neurons than AI has processing elements. ANNs are still able to process large amounts of data to make accurate predictions however. The type of classification system relevant is a supervised network containing an input layer, output layer, and hidden layers in between.

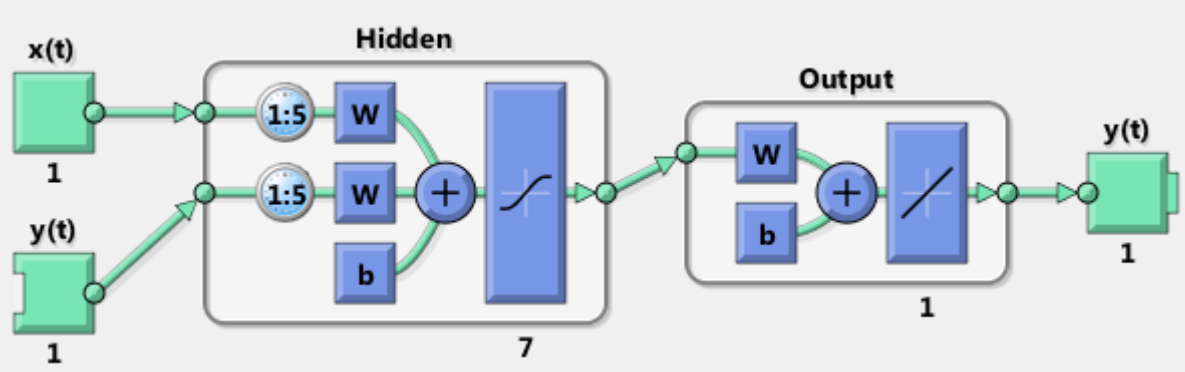

Figure 3. NARX neural network graphical diagram with 5 delays and 7 processing elements in the hidden layer

Supervised learning algorithms involve sample input and output, or target responses, data pairs in the training set. Conversely, unsupervised learning include only input data and not output variables. Unsupervised learning requires the system to figure out how to classify the input data features to predict future outcomes. Supervised learning is an excellent method for classification and prediction purposes [49]. Moreover, the applicable ANN supervised learning technique to predict outcomes is the nonlinear autoregressive network with exogenous inputs (NARX). NARX is a time series recurrent dynamic network model. The nonlinear dynamic model considers the input and output target values to be not proportional overtime. In other words, the changes in the relationship between the variables overtime may seem chaotic or unpredictable, thus opposite of linear systems. The time series analysis involves the use of a model to predict future values by

considering the internal structure (e.g., autocorrelation, trend, etc.) of previous observations. The equation defining NARX is the following [50]:

$$y(t) = f(y(t-1), y(t-2), \dots, y(t-ny), u(t-1), u(t-2), \dots, u(t-nu)) \quad (14)$$

Bayesian Regularization is the specific algorithm relevant to the machine learning NARX technique for the purpose of this research. It is a backpropagation algorithm training technique that enables improving the generalization of a predictive model. This is possible by modifying the performance function to include the mean of the sum of squares (MSE) with regards to the network weights and biases. This technique minimizes a combination of squared errors and weights to determine the correct combination to produce a network that generalizes well [51, 52].

2.4 *Input Variable Transformation*

Variable transformation techniques are useful in the fundamental statistical analysis portion to determine the linearity relative to the spectral image features and the CMP parameters. The objective of the input variable transform is to assess the residual error distribution from the binary conversion technique with regards to normality. This method can ensure the reliability of the machine learning model predictions. The transformations to assess the error distribution include reciprocal, logarithm, cube root, square root, and square. The initial three transformation are most common in statistical analysis. If the standard deviation is proportional to the mean squared, then a reciprocal transformation is meaningful. Logarithmic transformation is ideal if the standard deviation is proportional to the mean. Square root transformation is typical if the variance is proportional to the mean. This transformation method considers a broad range of arithmetical formulations to transform the data and assess the relationship between the given input variables and prediction error [53, 54].

2.5 *Summary*

LSCI is a reliable spectroscopic technique for continuous blood flow monitoring. The application is proven to display excellent inter-day reproducibility under PORH and LTH conditions, making it a reliable method to capture blood cell reflectance spectral images. The method instrumentation can be inexpensive to implement while maintaining a level of accuracy comparable to traditional LSCI systems. The technique is also effective in burn wound scenarios, penetrating the tissue to reflect the corresponding speckle pattern to the skin surface for analysis. This feature is important to maintain consistency when the skin is discolored, mutated, or when other objects are present making for undesired imperfections. Diabetic wounded cells respond best with a wavelength illumination of 632.8 nm as compared to other frequencies, thus serving as the initial wavelength of choice for developing the NI system. The method under investigation involves capturing spectral texture features and images reflecting from capillary blood cells with a 630 nm (+-5 nm) laser and analyzing the images to determine a correlation between the texture analysis and glucose/metabolic levels. LSCI is proven in the clinical application of continuous blood flow monitoring and might also be practicable in remote sensing analyte concentration. It provides much higher spatial resolution than that of laser Doppler perfusion imaging. This NICMP research involves classifying LSCI image features to remotely detect and predict analyte concentration with a coherent light source and digital image processing. The approach addresses the problem concerning SNR by providing a discrete signal for machine learning predictive modeling.

3. MATERIALS AND PROCEDURE

3.1 *Introduction*

The initial NICMP device development stage involved spectral image and CMP data collection. The spectral images were processed to extract texture features that characterize the grayscale images. The values derived from the feature extraction stage served as input variables to train the predictive model, given the known CMP data as output variables. The predictive model output was cross-validated to determine the NICMP accuracy, relative to the CMP test data.

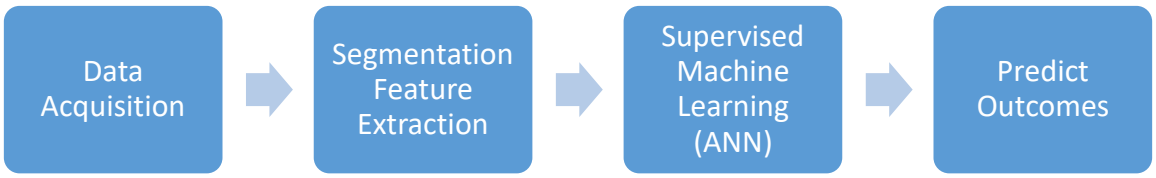

Figure 4. NICMP development method overview

3.2 *Non-Invasive Imaging Device*

3.2.1 *Introduction*

A custom LSCI device was developed to collect individual subject's spectral data. The device optical sensor, comprised of a red laser and a CCD camera, was configured to penetrate the palm area of either hand. The light reflectance generated from the laser was recorded via the camera, thus a video (i.e., multiple frames) was captured each instance the device was utilized. The laser and camera angle was arbitrarily configured. A predetermined angle was not considered because the camera and laser placement was consistent in the stationary device throughout the experiment. The custom device software visualized the laser generated reflectance, and quantified the spectral image to output numerical data to further describe perfusion activity. The quantified data was generated via a developer toolkit embedded in the custom application to construct a GLCM on the image, and extract the Haralick values. The individual frames of the speckle pattern video were automatically saved as .PNG images on the computer hard disk. The quantified data that describes the speckle pattern was also stored on the hard disk in the form of a text file.

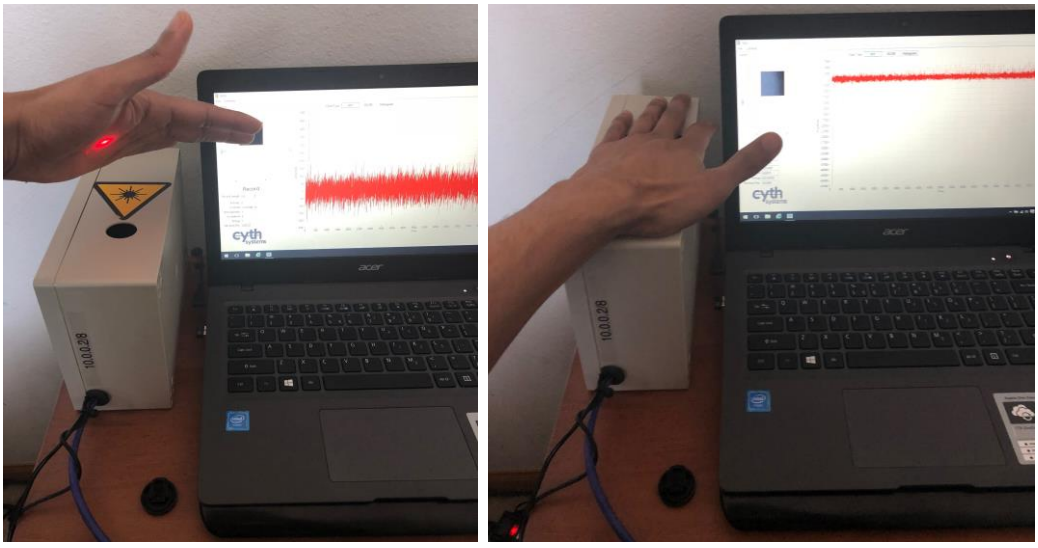

Figure 5. Custom LSCI device and subject palm placement to capture NI spectral data

3.2.2 *Configuration*

The spectral device optical sensor was comprised of a Balser ACA640-100GM camera with an Edmund Optics 58000 8.5mm F/1.3 lens, and an Edmund Optics NA090325027 635 nm laser. The spectral images were captured at 100 pixels x100 pixels at the rate of 100 frames-per-second. Each digital image sample captured with the device included 100-200 frames, which represented 1-2 seconds of the subject's microvascular perfusion. The custom application and interface was developed with LABVIEW (National Instruments Corp.) Haralick values module embedded in the application, and performed the GLCM on the images to extract and output quantified Haralick values.

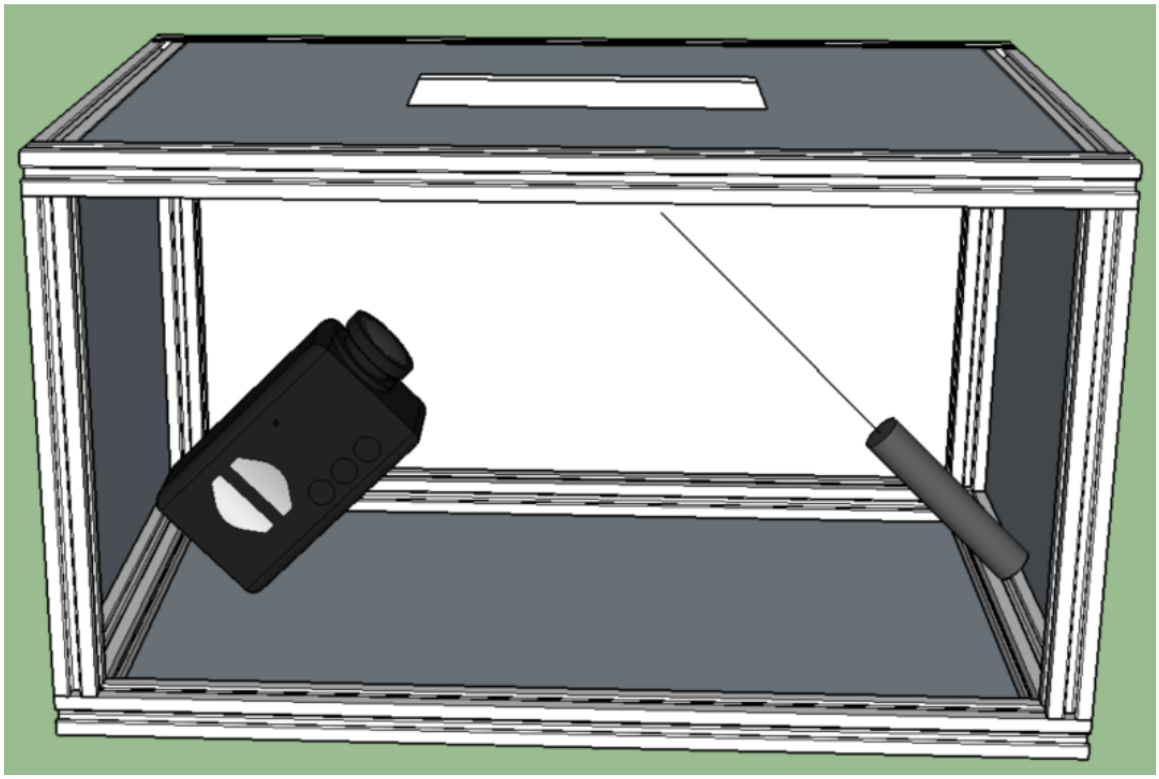

Figure 6. LSCI device optical sensor (i.e., laser and camera) arbitrarily configured

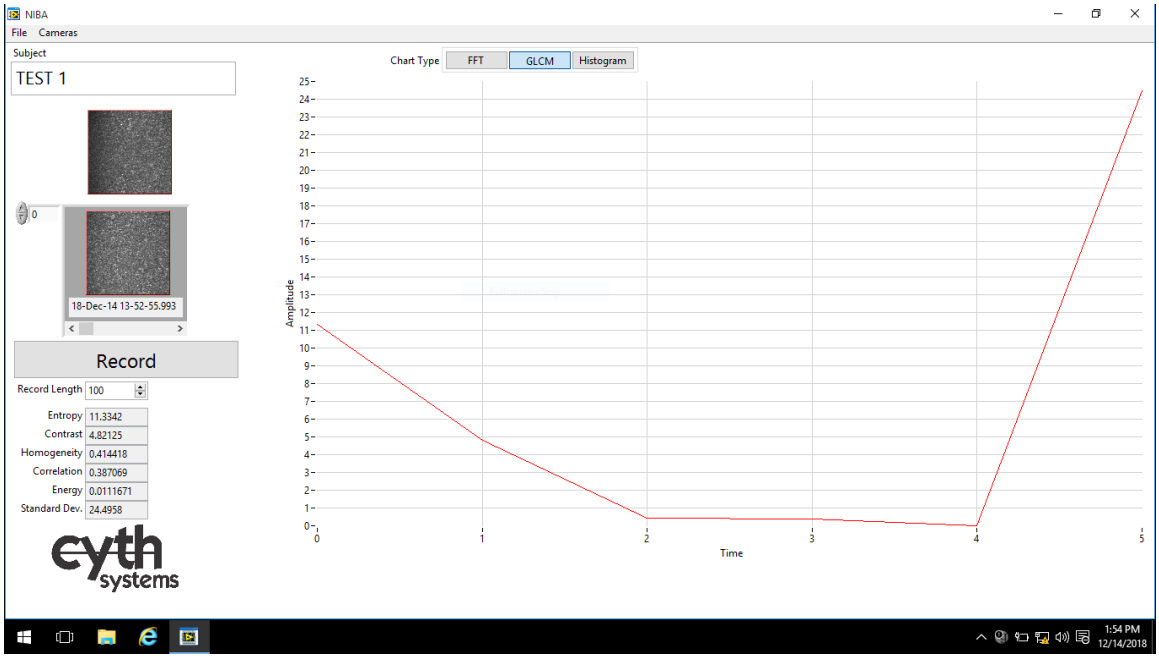

Figure 7. LSCI application interface displayed microvascular perfusion spectral images and Haralick values

3.3 *Clinical Data Collection*

3.3.1 *Introduction*

Determined by the Food & Drug Administration (FDA), the clinical trial was classified as a nonsignificant risk device study. The clinical trial included a cross-sectional study design. Subjects were recruited at random by distributed IRB approved marketing material. The primary objective of the standardized clinical trial was to cross-validate the NICMP output against the CMP test results to evaluate the accuracy of the NI system.

3.3.2 *Clinical Trial Protocol*

The clinical study was overseen by the University of North Dakota and Altru Health System IRBs, and included n=90 subjects. The study protocol excluded pregnant women, minor children, and any patients diagnosed with a chronic disease that requires routine medical attention.

The protocol included volunteers from the community under non-fasting conditions. The study procedure involved a CMP blood test and spectral data collected with the custom LSCI device. Spectral data was captured within two minutes after the CMP blood draw was performed. The CMP blood test was drawn from either arm. Additionally, spectral data was captured from the center of either palm. Both regions of interest were based on the individual subject's preference. The CMP blood test and spectral data was performed by clinical specialists after the subject's consent to participate in the research study was obtained. The clinical trial and CMP labs were executed and resulted at Altru Health System. The clinical data collection outcome included 90 CMP blood test results and spectral data that corresponded (< 2 min.) with the blood tests. In other words, the clinical study resulted in n=90 CMP and related spectral endpoints. Each subject participated in the clinical study once.

3.4 *Innovative Approach*

3.4.1 *Introduction*

The NICMP device predictive model was programmed with data collected from subjects as their own control. The predictive model was used to describe the relationship between the CMP and spectral data intended to predict outcomes in the future, given a different set of input (i.e. spectral) data. The spectral data produced by the NI device was programmed into the machine learning analysis as input values, while the CMP results were considered the target output values. Moreover, two NICMP predictive models were developed to determine how an increase in the number of training data endpoints affected the test results. The NICMP predictive model *beta* was developed to serve as reference model, and contains fewer training data endpoints for comparison. NICMP predictive model *one* includes more training data endpoints and represents the initial

predictive model iteration that produced test results within a certain range, relative to regulatory guidance.

3.4.2 *Machine Learning*

A Neural Net Times Series (NNTS) analysis was conducted in MATLAB to develop a predictive model through machine learning to predict future outcomes. The NNTS was configured to conduct the analysis with a NARX algorithm. The spectral values were inserted as the training data; the CMP values were set as the test data. The training and test data set was formatted in matrix row, given the layout of the collected data endpoints. The data was then randomly divided into a training, validation, and testing groups, also known as timesteps. The data set percent allocated for each timestep, relative to NICMP predictive models *beta* and *one* for each of the biological parameters in the CMP blood test, are displayed in Table 1 and 2, respectively. The timesteps are configured in MATLAB based on the percentage values. The configured network architecture settings are also displayed in Table 1. Included variables are time delays and processing elements, or neurons, and were configured in MATLAB prior to model development. The predictive model was trained with the Bayesian Regularization algorithm for each CMP blood level parameter. The training epoch consisted of up to 1,000 iterations to generate the “best-fit” model for each of the parameters in the CMP.

TABLE I

BETA TIMESTEP SETTINGS

CMP Parameter	Training (%)	Validation (%)	Testing (%)	Neurons	Delays
BUN	70	10	20	20	2
Sodium	70	10	20	10	2
Potassium	70	10	20	20	2
Chloride	70	10	20	20	4
CO2	70	10	20	20	2
Glucose	70	10	20	15	2
Creatinine	70	10	20	15	2
Calcium	70	10	20	15	2
Anion Gap	70	10	20	20	2
Albumin	70	10	20	20	2
Alkaline Phosphatase	70	10	20	2	2
AST	70	10	20	2	2
ALT	70	10	20	2	2
Bilirubin Total	70	10	20	2	2
Protein Total	70	10	20	2	2

Table 1. Machine learning timesteps configured in MATLAB to generate the NICMP beta predictive model

TABLE II

ONE TIMESTEP SETTINGS

CMP Parameter	Training (%)	Validation (%)	Testing (%)	Neurons	Delays
BUN	90	5	5	20	2
Sodium	90	5	5	10	2
Potassium	90	5	5	20	2
Chloride	90	5	5	20	4
CO2	90	5	5	20	2
Glucose	60	35	5	15	2
Creatinine	90	5	5	15	2
Calcium	90	5	5	15	2
Anion Gap	90	5	5	20	2
Albumin	90	5	5	20	2
Alkaline Phosphatase	90	5	5	2	2
AST	90	5	5	2	2
ALT	90	5	5	2	2
Bilirubin Total	90	5	5	2	2
Protein Total	90	5	5	2	2

Table 2 Machine learning timesteps configured in MATLAB to generate the NICMP one predictive model

3.5 *Statistical Analysis*

3.5.1 *Introduction*

The analysis included a statistical summary of the NICMP predictive model, covariance and correlation coefficient analysis, and an underlying analysis with respect to the original grayscale spectral images converted to binary with three different threshold techniques applied. The predictive model summary statistics were generated via MATLAB. The grayscale spectral image intensity values were converted to binary values via a custom MATLAB script. Moreover, the predictive model summary described the accuracy in terms of error and correlation. One grayscale image per sample was converted to binary to determine the underlying error distribution.

3.5.2 *Predictive Model Summary*

The machine learning model considered the averaged grayscale Haralick values, or texture, performed via LABVIEW. The predictive model analysis involved an MSE minimized approach. The machine learning method required a validation parameter to minimize error with each subsequent iteration until good generalization occurred. The applied machine learning technique generated the MSE and correlation figures that described the predictive model performance, and direction of the relationship (i.e., positive or negative). The coefficient of determination figure was calculated to determine the overall strength of the minimized error model. The predictive model statistical analysis is imperative to determine the prediction capability of the NICMP device, given the machine learning approach. The covariance and correlation coefficient was also determined to assess the interrelationships between any pair of metabolic analytes, given the digital image processing technique. Positive values with respect to covariance implies that the variables, or analytes in this case, move together in the same direction while negative values mean the analytes

move inversely, relative to each other. The correlation coefficient is a function of covariance, and also describes the degree to which any two analytes are related. For example, a correlation coefficient of -1 implies that the analytes move inversely, a value of 0 indicates an interrelationship does not exist, and a value of 1 implies the analytes move together in the same direction. Sample data was considered for the covariance while the population was considered for the correlation coefficient to increase the analysis cross-section. Statistical analyses involving sample data usually considers 1 degree of freedom, and is the case for this research.

3.5.3 *Binary Image Error Distribution*

The binary analysis involved conversion of one grayscale spectral image from each sample with three different threshold techniques applied. The original grayscale images were converted to binary by averaging, adaptive, and Otsu threshold techniques. The outcome included three binary image values per grayscale image. The binary values were transformed and processed as input variables in the MATLAB regression learner app, given the CMP values as the target data. The regression model types included linear regression, regression trees, support vector machines, Gaussian process regression, and ensemble of trees. Each regression model type also included multiple sub-types. The analysis considered all regression model types and sub-types to train the regression models. This produced the root mean squared error for each binary image. The error values were compared to the standard deviation of the mean to determine the distribution of error, given the binary image values.

4. RESULTS

4.1 *Machine Learning Model*

4.1.1 *Predictive Model Statistical Analysis*

Figure 8 displays the original grayscale spectral image from a sample of 100-200 images. The predictive model development considers the average Haralick values and additional statistics, given the total number of images in the sample and the CMP analyte concentration as the target output. Table 3 displays the average Haralick values and statistics of the sample pertaining to the representative image.

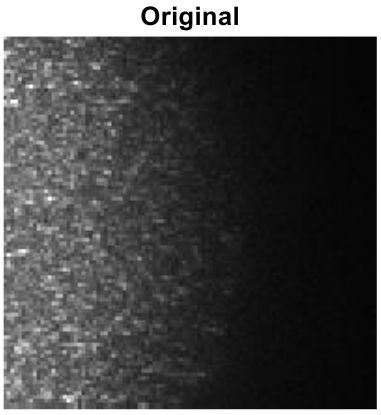

Figure 8. Original grayscale spectral image representative of a sample containing 100-200 images

TABLE III
GRAYSCALE SPECTRAL IMAGE TEXTURE FEATURES AND VALUES

Entropy	Contrast	Homogeneity	Correlation	Energy	Standard Deviation
8.332874	4.406495	0.618372	0.865251	0.050193	45.0444

Table 3 Original grayscale spectral image average texture values given the total number of images in the sample

The results of the cross-validation trial includes the analysis describing the NICMP machine learning predictive model as it relates to the venipuncture CMP. Moreover, the results

compare the testing data against the target output data. The test data set does not include endpoints included in the training data set during model development. The method of comparison includes the MSE and correlation to determine the accuracy and strength of the model. The machine learning approach provides a comprehensive analysis as it considers the image intensity values during perfusion (i.e., 1-2 seconds). The objective is to develop a model capable of predicting future observations. The statistical analysis provides a reliable method to determine the repeatability of the device. Tables 4 and 5 indicate the clinical data descriptive statistics and the performance of NICMP predictive model *beta (B)* and *one* with regards to the venipuncture CMP results, respectively.

TABLE IV

CLINICAL DATA SAMPLE DATA DESCRIPTIVE STATISTICS[1]

CMP Parameter	N	Minimum	Maximum	$\overline{X}$	s	$CI\mu/_{95}$ (+/-)
BUN	90	4.0	24.0	13.0	3.8	0.79
Sodium	90	135.0	143.0	139.0	1.8	0.36
Potassium	90	3.4	5.6	4.1	0.4	0.07
Chloride	90	99.0	109.0	105.0	1.9	0.39
CO2	90	19.2	32.1	25.8	2.4	0.49
Glucose	90	61.0	157.0	98.0	17.0	3.51
Creatinine	90	0.6	1.3	0.9	0.2	0.03
Calcium	90	8.6	10.9	9.5	0.4	0.08
Anion Gap	90	2.9	13.1	8.1	1.6	0.32
Albumin	90	3.9	5.2	4.4	0.3	0.05
Alkaline Phosphatase	90	13.0	165.0	70.0	22.8	4.70
AST	90	9.0	94.0	20.0	9.7	2.00
ALT	90	7.0	82.0	21.0	11.8	2.44
Bilirubin Total	90	0.2	1.7	0.6	0.3	0.07
Protein Total	90	6.2	8.3	7.2	0.4	0.09

Table 4 Clinical data descriptive statistics

[1] The CPM parameter refers to the comprehensive metabolic panel analyte of interest. "N" refers to the sample size. The minimal and maximum values are indicative of the analyte concentration range in the clinical study. X-bar references the sample mean. The lowercase "s" represents the sample standard deviation. $CI\mu_{/95}$ indicates the 95% confidence interval of the population mean.

TABLE V

PREDICTIVE MODEL SUMMARY STATISTICS[2]

CMP Parameter	MSE(B)	R(B)	R^2(B)	MSE	R	R^2
BUN	9.1	0.41	0.2	1	-1.00	1.0
Sodium	3.7	0.42	0.2	1	-1.00	1.0
Potassium	0	0.34	0.1	0	-1.00	1.0
Chloride	1.3	0.40	0.2	1	0.70	0.5
CO2	4	-0.40	0.2	0	-1.00	1.0
Glucose	124	0.27	0.1	5	-0.90	0.8
Creatinine	0.02	0.44	0.2	0	-1	1.0
Calcium	0.2	-0.45	0.2	0	-1	1.0
Anion Gap	3.3	-0.51	0.3	0	1	1.0
Albumin	0.09	-0.5	0.3	0	1	1.0
Alkaline Phosphatase	182.5	0.3	0.1	20	1	1.0
AST	19	0.36	0.1	1	1	1.0
ALT	45	0.3	0.1	4	0.9	0.8
Bilirubin Total	0.05	0.4	0.2	0	1	1.0
Protein Total	3.8	-0.41	0.2	0	1	1.0

Table 5 Statistical analysis for NICMP predictive models beta and one (n=90)

The covariance and correlation coefficient is taken into consideration for the CMP actual measurements and NICMP predictive model output, or predictions. NICMP predictive models *beta* and *one* includes n=18 (20%) and n=5 (5%) cross-validation endpoints, respectively. Therefore, the same number of CMP actual measurements are taken into consideration to compare the correlation coefficients, relative to the predictive models. The n=18 cross-validation endpoints differ from the n=5 endpoints. Table VI displays the percent of positive and negative values, given the covariance and correlation coefficient matrices.

[2] MSE refers to the predictive model mean squared error, relative to the test output. The R values refers to the predictive model correlation. The R-squared value refers to the predictive model coefficient of determination. Note: (B) indicates the NICMP *beta* predictive model summary statistics.

TABLE VI

COVARIANCE AND VARIANCE RELATIONSHIP PERCENT SUMMARY

	Positive/Negative (%)
CMP 1 (n=18)	65/35
NICMP predictive model beta	57/43
CMP 2 (n=5)	57/52
NICMP predictive model one	52/48

Table 6 Ratio of positive and negative covariance and correlation coefficient values

Tables 7-14, the covariance and correlation coefficient matrices, indicate the distribution of positive and negative values, relative to the covariance and correlation coefficient for the CMP measurements and NICMP predictive model outputs. The average correlation coefficient for CMP 1 (n=18) and NICMP *beta* predictive model is 0.1169 and -0.396, respectively. The average correlation coefficient for CMP 2 (n=5) and NICMP predictive model is -0.0624 and 0.0085, respectively.

TABLE VII

CMP 1 COVARIANCE

	BUN	Sodium	Potassium	Chloride	CO2	Glucose	Creatinine	Calcium	Anion_Ga	Albumin	Alkaline_I	AST	ALT	Bilirubin_	Protein_T	**(y)**
BUN		-0.35294	0.258824	-0.52941	0.894118	-13.2353	0.111765	0.129412	-0.71765	0.535294	-11.6471	-0.29412	4.764706	-0.02941	0.194118	
Sodium	-0.35294		-0.37843	1.735294	0.231373	9.676471	0.036275	-0.02451	1.121569	0.079412	10.80392	2.362745	3.77451	0.009804	0.223529	
Potassium	0.258824	-0.37843		-0.15882	0.095033	-2.22157	-0.00876	-0.00203	-0.31464	-0.02961	-2.07582	0.363399	0.847712	0.009085	-0.03098	
Chloride	-0.52941	1.735294	-0.15882		-0.71765	-15.6765	-0.06765	-0.36765	-2.04706	-0.17353	21.41176	4.911765	5.852941	0.041176	-0.27059	
CO2	0.894118	0.231373	0.095033	-0.71765		7.233333	0.01817	0.148497	-0.22771	0.01549	-0.7183	0.10719	0.675817	0.026209	-0.1449	
Glucose	-13.2353	9.676471	-2.22157	-15.6765	7.233333		0.769608	2.783333	18.11961	1.097059	-23.451	-7.12745	-32.6569	0.643137	1.247059	
Creatinine	0.111765	0.036275	-0.00876	-0.06765	0.01817	0.769608		0.021993	0.085752	0.028333	0.786928	0.458497	1.04281	0.004183	0.038431	
Calcium	0.129412	-0.02451	-0.00203	-0.36765	0.148497	2.783333	0.021993		0.194641	0.049314	-1.03595	0.468954	0.761111	0.018562	0.059804	
Anion_Ga	-0.71765	1.121569	-0.31464	-2.04706	-0.22771	18.11961	0.085752	0.194641		0.237451	-9.88954	-2.65621	-2.75425	-0.05758	0.63902	
Albumin	0.535294	0.079412	-0.02961	-0.17353	0.01549	1.097059	0.028333	0.049314	0.237451		-1.2549	0.159804	0.812745	0.00451	0.114118	
Alkaline_I	-11.6471	10.80392	-2.07582	21.41176	-0.7183	-23.451	0.786928	-1.03595	-9.88954	-1.2549		36.49673	55.69281	0.588889	-1.99804	
AST	-0.29412	2.362745	0.363399	4.911765	0.10719	-7.12745	0.458497	0.468954	-2.65621	0.159804	36.49673		93.52614	0.922222	0.813725	
ALT	4.764706	3.77451	0.847712	5.852941	0.675817	-32.6569	1.04281	0.761111	-2.75425	0.812745	55.69281	93.52614		1.224183	2.131373	
Bilirubin_	-0.02941	0.009804	0.009085	0.041176	0.026209	0.643137	0.004183	0.018562	-0.05758	0.00451	0.588889	0.922222	1.224183		0.013137	
Protein_T	0.194118	0.223529	-0.03098	-0.27059	-0.1449	1.247059	0.038431	0.059804	0.63902	0.114118	-1.99804	0.813725	2.131373	0.013137		
(x)																

Table 7 Covariance of CMP actual measurements (n=18)

TABLE VIII

CMP 1 CORRELATION COEFFICIENT

	BUN	Sodium	Potassium	Chloride	CO2	Glucose	Creatinine	Calcium	Anion_Ga	Albumin	Alkaline_I	AST	ALT	Bilirubin_T	Protein_T	**(y)**
BUN		-0.06172	0.211499	-0.0767	0.253305	-0.21025	0.212826	0.146699	-0.11967	0.516429	-0.15864	-0.01171	0.112417	-0.06011	0.115185	
Sodium	-0.06172		-0.5726	0.465491	0.121372	0.284625	0.127902	-0.05145	0.34631	0.14186	0.272488	0.174121	0.164896	0.037098	0.245596	
Potassium	0.211499	-0.5726		-0.19908	0.232944	-0.30534	-0.1443	-0.01987	-0.45397	-0.24715	-0.24464	0.125138	0.17305	0.160638	-0.15905	
Chloride	-0.0767	0.465491	-0.19908		-0.31186	-0.38199	-0.19759	-0.63928	-0.52362	-0.2568	0.447371	0.299861	0.211823	0.129077	-0.24629	
CO2	0.253305	0.121372	0.232944	-0.31186		0.344675	0.103788	0.504945	-0.1139	0.044828	-0.02935	0.012797	0.04783	0.160665	-0.25792	
Glucose	-0.21025	0.284625	-0.30534	-0.38199	0.344675		0.246497	0.530691	0.508222	0.178021	-0.05373	-0.04771	-0.1296	0.221066	0.124463	
Creatinine	0.212826	0.127902	-0.1443	-0.19759	0.103788	0.246497		0.50268	0.288316	0.551136	0.216117	0.367923	0.49607	0.172357	0.45979	
Calcium	0.146699	-0.05145	-0.01987	-0.63928	0.504945	0.530691	0.50268		0.389577	0.571036	-0.16937	0.224019	0.215536	0.455303	0.425929	
Anion_Ga	-0.11967	0.34631	-0.45397	-0.52362	-0.1139	0.508222	0.288316	0.389577		0.404481	-0.23784	-0.18666	-0.11474	-0.20777	0.6695	
Albumin	0.516429	0.14186	-0.24715	-0.2568	0.044828	0.178021	0.551136	0.571036	0.404481		-0.17461	0.064969	0.19588	0.094145	0.691711	
Alkaline_I	-0.15864	0.272488	-0.24464	0.447371	-0.02935	-0.05373	0.216117	-0.16937	-0.23784	-0.17461		0.209491	0.189508	0.173565	-0.17099	
AST	-0.01171	0.174121	0.125138	0.299861	0.012797	-0.04771	0.367923	0.224019	-0.18666	0.064969	0.209491		0.929882	0.794204	0.203474	
ALT	0.112417	0.164896	0.17305	0.211823	0.04783	-0.1296	0.49607	0.215536	-0.11474	0.19588	0.189508	0.929882		0.624971	0.315942	
Bilirubin_T	-0.06011	0.037098	0.160638	0.129077	0.160665	0.221066	0.172357	0.455303	-0.20777	0.094145	0.173565	0.794204	0.624971		0.168676	
Protein_T	0.115185	0.245596	-0.15905	-0.24629	-0.25792	0.124463	0.45979	0.425929	0.6695	0.691711	-0.17099	0.203474	0.315942	0.168676		
(x)																

Table 8 Correlation coefficient of CMP actual measurements (n=18)

TABLE IX

NICMP BETA PREDICTIVE MODEL COVARIANCE

	BUN	Sodium	Potassium	Chloride	CO2	Glucose	Creatinine	Calcium	Anion_Ga	Albumin	Alkaline_I	AST	ALT	Bilirubin_	Protein_T	**(y)**
BUN		1.1176471	-0.18903	9.326797	1.266687	-144.503	-0.02593	-0.88226	6.855133	-0.76506	-60.7908	121.281	-60.4314	1.084482	8.213423	
Sodium	1.117647		0.49956	-0.85294	2.070812	-121.029	-0.18886	0.700125	-0.50152	-0.25473	107.9118	35.79412	4.352941	0.728563	-0.53224	
Potassium	-0.18903	0.49956		0.170087	1.173859	18.55775	-0.03341	0.258793	-0.03985	-0.07171	-9.50195	-5.0857	6.509822	0.055193	0.888851	
Chloride	9.326797	-0.8529412	0.170087		-4.57394	97.5719	0.112148	0.528958	-4.48538	0.177639	-97.1601	-30.9771	-20.7451	0.796648	1.057858	
CO2	1.266687	2.0708116	1.173859	-4.57394		-45.6652	-0.20132	1.322084	-6.61983	-0.45092	229.5513	-49.1251	-6.50583	-0.91882	6.321637	
Glucose	-144.503	-121.02941	18.55775	97.5719	-45.6652		0.126611	14.2929	-75.9947	3.16909	-3913.9	-1130.79	-1326.08	7.190852	88.88134	
Creatinine	-0.02593	-0.1888572	-0.03341	0.112148	-0.20132	0.126611		-0.0492	-0.26607	0.00802	-12.843	-1.00665	-0.76822	-0.00313	-0.16331	
Calcium	-0.88226	0.7001246	0.258793	0.528958	1.322084	14.2929	-0.0492		-0.56553	-0.00259	38.13427	-4.92831	2.142205	0.079793	0.469473	
Anion_Ga	6.855133	-0.5015208	-0.03985	-4.48538	-6.61983	-75.9947	-0.26607	-0.56553		-0.46385	136.0326	86.32295	107.9449	-0.05321	2.281317	
Albumin	-0.76506	-0.2547283	-0.07171	0.177639	-0.45092	3.16909	0.00802	-0.00259	-0.46385		4.431514	-1.47335	-3.91986	-0.05739	-0.08442	
Alkaline_I	-60.7908	107.91176	-9.50195	-97.1601	229.5513	-3913.9	-12.843	38.13427	136.0326	4.431514		1970.141	1127.549	-13.5502	-70.7631	
AST	121.281	35.794118	-5.0857	-30.9771	-49.1251	-1130.79	-1.00665	-4.92831	86.32295	-1.47335	1970.141		219.6275	-1.27534	-11.1407	
ALT	-60.4314	4.3529412	6.509822	-20.7451	-6.50583	-1326.08	-0.76822	2.142205	107.9449	-3.91986	1127.549	219.6275		2.677918	-4.55343	
Bilirubin_	1.084482	0.7285627	0.055193	0.796648	-0.91882	7.190852	-0.00313	0.079793	-0.05321	-0.05739	-13.5502	-1.27534	2.677918		-0.19016	
Protein_T	8.213423	-0.5322409	0.888851	1.057858	6.321637	88.88134	-0.16331	0.469473	2.281317	-0.08442	-70.7631	-11.1407	-4.55343	-0.19016		
(x)																

Table 9 Covariance of NICMP beta predictive model output (n=18)

TABLE X

NICMP BETA PREDICTIVE MODEL CORRELATION COEFFICIENT

	BUN	Sodium	Potassium	Chloride	CO2	Glucose	Creatinine	Calcium	Anion_Ga	Albumin	Alkaline_I	AST	ALT	Bilirubin_	Protein_T	**(y)**
BUN		0.0272371	-0.02388	0.273232	0.02083	-0.15305	-0.01458	-0.11465	0.13683	-0.19571	-0.03593	0.361002	-0.12999	0.197441	0.263323	
Sodium	0.027237		0.187733	-0.07433	0.101298	-0.38132	-0.31588	0.270649	-0.02978	-0.19384	0.189714	0.31694	0.027853	0.394577	-0.05076	
Potassium	-0.02388	0.1877334		0.076836	0.297664	0.303089	-0.28965	0.518598	-0.01227	-0.28289	-0.08659	-0.23343	0.215929	0.154951	0.439431	
Chloride	0.273232	-0.0743305	0.076836		-0.26896	0.369542	0.225486	0.245807	-0.32015	0.162497	-0.20533	-0.32972	-0.15957	0.518648	0.121278	
CO2	0.02083	0.1012985	0.297664	-0.26896		-0.09708	-0.22721	0.344862	-0.26523	-0.23154	0.272312	-0.29351	-0.02809	-0.33578	0.406817	
Glucose	-0.15305	-0.3813182	0.303089	0.369542	-0.09708		0.009203	0.240127	-0.1961	0.104807	-0.29904	-0.43515	-0.36877	0.169253	0.368396	
Creatinine	-0.01458	-0.3158791	-0.28965	0.225486	-0.22721	0.009203		-0.43879	-0.3645	0.140798	-0.52093	-0.20565	-0.11341	-0.03905	-0.35934	
Calcium	-0.11465	0.2706485	0.518598	0.245807	0.344862	0.240127	-0.43879		-0.17906	-0.01051	0.357495	-0.2327	0.073094	0.230439	0.238753	
Anion_Ga	0.13683	-0.0297785	-0.01227	-0.32015	-0.26523	-0.1961	-0.3645	-0.17906		-0.2891	-0.2891	0.195876	0.565724	-0.0236	0.1782	
Albumin	-0.19571	-0.1938402	-0.28289	0.162497	-0.23154	0.104807	0.140798	-0.01051	-0.2891		0.081779	-0.13694	-0.26328	-0.32625	-0.08451	
Alkaline_I	-0.03593	0.1897139	-0.08659	-0.20533	0.272312	-0.29904	-0.52093	0.357495	0.195876	0.081779		0.423046	0.174966	-0.17796	-0.16366	
AST	0.361002	0.3169403	-0.23343	-0.32972	-0.29351	-0.43515	-0.20565	-0.2327	0.626038	-0.13694	0.423046		0.171649	-0.08436	-0.12977	
ALT	-0.12999	0.0278533	0.215929	-0.15957	-0.02809	-0.36877	-0.11341	0.073094	0.565724	-0.26328	0.174966	0.171649		0.128012	-0.03833	
Bilirubin_	0.197441	0.3945766	0.154951	0.518648	-0.33578	0.169253	-0.03905	0.230439	-0.0236	-0.32625	-0.17796	-0.08436	0.128012		-0.13548	
Protein_T	0.263323	-0.05076	0.439431	0.121278	0.406817	0.368396	-0.35934	0.238753	0.1782	-0.08451	-0.16366	-0.12977	-0.03833	-0.13548		
(x)																

Table 10 Correlation coefficient of NICMP beta predictive model output (n=18)

TABLE XI

CMP 2 COVARIANCE

	BUN	Sodium	Potassium	Chloride	CO2	Glucose	Creatinine	Calcium	Anion_Ga	Albumin	Alkaline_I	AST	ALT	Bilirubin_T	Protein_T	**(y)**
BUN		-1.9	0.07	0.35	0.46	1.65	0.14	0.2	-2.71	0.525	-62.3	-113.25	-61.35	1.1	-0.02	
Sodium	-1.9		-0.11	0.45	-0.38	-1.95	-0.02	-0.1	0.63	-0.025	1.9	16.25	7.55	2.08E-17	-0.14	
Potassium	0.07	-0.11		-0.11	0.089	-1.315	-0.004	0.04	-0.089	-0.025	-1.22	2.2	0.11	-4.2E-17	0.037	
Chloride	0.35	0.45	-0.11		-0.48	-4.7	0.005	-0.075	-0.27	0.175	-28.1	-7	-6.95	0.1	-0.065	
CO2	0.46	-0.38	0.089	-0.48		1.405	0.003	0.065	-0.177	-0.045	6.14	-2.15	-0.27	-0.05	0.086	
Glucose	1.65	-1.95	-1.315	-4.7	1.405		0.17	-0.475	1.345	-0.025	187.1	-90	11.45	-1.225	0.065	
Creatinine	0.14	-0.02	-0.004	0.005	0.003	0.17		-8.9E-18	-0.028	0.0075	-0.49	-1.525	-0.705	0.01	-0.001	
Calcium	0.2	-0.1	0.04	-0.075	0.065	-0.475	-8.9E-18		-0.09	-0.0075	-0.95	-0.475	-0.675	0.005	0.025	
Anion_Ga	-2.71	0.63	-0.089	-0.27	-0.177	1.345	-0.028	-0.09		-0.155	23.86	25.4	14.77	-0.05	-0.161	
Albumin	0.525	-0.025	-0.025	0.175	-0.045	-0.025	0.0075	-0.0075	-0.155		-5.6	-6.225	-3.35	0.035	-0.0025	
Alkaline_I	-62.3	1.9	-1.22	-28.1	6.14	187.1	-0.49	-0.95	23.86	-5.6		533.5	428.6	-6.5	-0.53	
AST	-113.25	16.25	2.2	-7	-2.15	-90	-1.525	-0.475	25.4	-6.225	533.5		584.25	-8.05	0.175	
ALT	-61.35	7.55	0.11	-6.95	-0.27	11.45	-0.705	-0.675	14.77	-3.35	428.6	584.25		-5.55	0.215	
Bilirubin_T	1.1	2.08E-17	-4.2E-17	0.1	-0.05	-1.225	0.01	0.005	-0.05	0.035	-6.5	-8.05	-5.55		-0.09	
Protein_T	-0.02	-0.14	0.037	-0.065	0.086	0.065	-0.001	0.025	-0.161	-0.0025	-0.53	0.175	0.215	-0.09		
(x)																

Table 11 Covariance of CMP actual measurements (n=5)

TABLE XII

CMP 2 CORRELATION COEFFICIENT

	BUN	Sodium	Potassium	Chloride	CO2	Glucose	Creatinine	Calcium	Anion_Ga	Albumin	Alkaline_I	AST	ALT	Bilirubin_T	Protein_T	**(y)**
BUN		-0.64752	0.073873	0.091101	0.24921	0.053033	0.892607	0.360668	-0.74458	0.669456	-0.54033	-0.93451	-0.96412	0.647003	-0.02111	
Sodium	-0.64752		-0.48661	0.49099	-0.86297	-0.26272	-0.53452	-0.75593	0.725577	-0.13363	0.069077	0.562085	0.497357	5.13E-17	-0.61932	
Potassium	0.073873	-0.48661		-0.37166	0.625877	-0.54863	-0.33104	0.936329	-0.31741	-0.4138	-0.13735	0.235645	0.022439	-3.2E-16	0.506849	
Chloride	0.091101	0.49099	-0.37166		-0.83255	-0.48364	0.102062	-0.43301	-0.2375	0.714435	-0.78027	-0.18493	-0.34967	0.188311	-0.21961	
CO2	0.24921	-0.86297	0.625877	-0.83255		0.300919	0.127458	0.781094	-0.32406	-0.38237	0.354859	-0.11822	-0.02827	-0.19597	0.60478	
Glucose	0.053033	-0.26272	-0.54863	-0.48364	0.300919		0.428496	-0.33864	0.146092	-0.0126	0.641525	-0.2936	0.071136	-0.28485	0.027118	
Creatinine	0.892607	-0.53452	-0.33104	0.102062	0.127458	0.428496		-1.3E-15	-0.6033	0.75	-0.33328	-0.98685	-0.86885	0.461266	-0.08276	
Calcium	0.360668	-0.75593	0.936329	-0.43301	0.781094	-0.33864	-1.3E-15		-0.54848	-0.21213	-0.18276	-0.08694	-0.23529	0.065233	0.585206	
Anion_Ga	-0.74458	0.725577	-0.31741	-0.2375	-0.32406	0.146092	-0.6033	-0.54848		-0.66794	0.699342	0.708311	0.784409	-0.09939	-0.57419	
Albumin	0.669456	-0.13363	-0.4138	0.714435	-0.38237	-0.0126	0.75	-0.21213	-0.66794		-0.76178	-0.80566	-0.82571	0.322886	-0.04138	
Alkaline_I	-0.54033	0.069077	-0.13735	-0.78027	0.354859	0.641525	-0.33328	-0.18276	0.699342	-0.76178		0.469634	0.718538	-0.40786	-0.05967	
AST	-0.93451	0.562085	0.235645	-0.18493	-0.11822	-0.2936	-0.98685	-0.08694	0.708311	-0.80566	0.469634		0.931894	-0.48057	0.018745	
ALT	-0.96412	0.497357	0.022439	-0.34967	-0.02827	0.071136	-0.86885	-0.23529	0.784409	-0.82571	0.718538	0.931894		-0.631	0.043858	
Bilirubin_T	0.647003	5.13E-17	-3.2E-16	0.188311	-0.19597	-0.28485	0.461266	0.065233	-0.09939	0.322886	-0.40786	-0.48057	-0.631		-0.68714	
Protein_T	-0.02111	-0.61932	0.506849	-0.21961	0.60478	0.027118	-0.08276	0.585206	-0.57419	-0.04138	-0.05967	0.018745	0.043858	-0.68714		
(x)																

Table 12 Correlation coefficient of CMP actual measurements (n=5)

TABLE XIII

NICMP PREDICTIVE MODEL COVARIANCE

	BUN	Sodium	Potassium	Chloride	CO2	Glucose	Creatinine	Calcium	Anion_Ga	Albumin	Alkaline_P	AST	ALT	Bilirubin_T	Protein_T	**(y)**
BUN		-21.2	2.47456	3.75	-20.8292	-6.85	0.878988	-2.92152	23.74367	1.44558	176.1	35.85	-188.65	3.108084	6.136958	
Sodium	-21.2		-0.8104	1.25	4.650797	-64.9	-0.27609	0.146274	-10.3602	0.766475	-110.6	9.15	91.4	-0.61408	-0.35022	
Potassium	2.47456	-0.8103954		-0.35071	-0.9446	-3.06382	0.026004	-0.15804	0.682271	-0.02181	20.75407	2.98993	-5.48136	0.033793	0.112954	
Chloride	3.75	1.25	-0.35071		-0.41971	-0.75	0.034791	0.019683	0.526047	0.546029	-62.75	-1.25	-4.25	0.462083	0.83379	
CO2	-20.8292	4.6507971	-0.9446	-0.41971		18.22524	-0.26066	1.611008	-7.44696	-0.41881	-193.683	-56.5561	107.2607	-1.64885	-2.34914	
Glucose	-6.85	-64.9	-3.06382	-0.75	18.22524		0.398492	8.499468	37.82498	-7.59935	-51.8	-239.8	-389.55	0.759378	-8.4047	
Creatinine	0.878988	-0.2760938	0.026004	0.034791	-0.26066	0.398492		-0.02802	0.287652	0.009491	2.393622	0.354131	-2.48925	0.035996	0.0614	
Calcium	-2.92152	0.1462742	-0.15804	0.019683	1.611008	8.499468	-0.02802		-0.5094	-0.10479	-16.6643	-5.82662	4.98481	-0.11464	-0.30073	
Anion_Ga	23.74367	-10.36023	0.682271	0.526047	-7.44696	37.82498	0.287652	-0.5094		-0.10723	82.8476	3.509754	-87.0871	1.01065	1.309485	
Albumin	1.44558	0.7664751	-0.02181	0.546029	-0.41881	-7.59935	0.009491	-0.10479	-0.10723		-11.0469	2.456909	1.781401	0.109057	0.301882	
Alkaline_P	176.1	-110.6	20.75407	-62.75	-193.683	-51.8	2.393622	-16.6643	82.8476	-11.0469		513.05	-1052.7	4.550328	2.805941	
AST	35.85	9.15	2.98993	-1.25	-56.5561	-239.8	0.354131	-5.82662	3.509754	2.456909	513.05		-124.7	3.017693	6.430716	
ALT	-188.65	91.4	-5.48136	-4.25	107.2607	-389.55	-2.48925	4.98481	-87.0871	1.781401	-1052.7	-124.7		-11.1058	-11.7175	
Bilirubin_T	3.108084	-0.6140839	0.033793	0.462083	-1.64885	0.759378	0.035996	-0.11464	1.01065	0.109057	4.550328	3.017693	-11.1058		0.339769	
Protein_T	6.136958	-0.3502214	0.112954	0.83379	-2.34914	-8.4047	0.0614	-0.30073	1.309485	0.301882	2.805941	6.430716	-11.7175	0.339769		
(x)																

Table 13 Covariance of NICMP predictive model output (n=5)

TABLE XIV

NICMP PREDICTIVE MODEL CORRELATION COEFFICIENT

	BUN	Sodium	Potassium	Chloride	CO2	Glucose	Creatinine	Calcium	Anion_Ga	Albumin	Alkaline_P	AST	ALT	Bilirubin_T	Protein_T	**(y)**
BUN		-0.6317419	0.643094	0.261593	-0.48769	-0.02819	0.976443	-0.66497	0.850187	0.356115	0.324159	0.278351	-0.67533	0.732118	0.804563	
Sodium	-0.63174		-0.51588	0.213589	0.26673	-0.65423	-0.75127	0.081552	-0.90868	0.46251	-0.49869	0.17402	0.801464	-0.35432	-0.11247	
Potassium	0.643094	-0.5158806		-0.52263	-0.47246	-0.26935	0.617089	-0.76845	0.521882	-0.11477	0.816113	0.495922	-0.41918	0.170042	0.316342	
Chloride	0.261593	0.2135894	-0.52263		-0.05635	-0.0177	0.221617	0.025689	0.108008	0.771311	-0.66234	-0.05565	-0.08724	0.62413	0.626801	
CO2	-0.48769	0.2667302	-0.47246	-0.05635		0.144353	-0.5573	0.705716	-0.5132	-0.19857	-0.68617	-0.84513	0.738999	-0.7475	-0.59273	
Glucose	-0.02819	-0.6542315	-0.26935	-0.0177	0.144353		0.14975	0.654434	0.458172	-0.6333	-0.03226	-0.62985	-0.47175	0.06051	-0.37275	
Creatinine	0.976443	-0.7512701	0.617089	0.221617	-0.5573	0.14975		-0.58245	0.940525	0.213503	0.402337	0.251075	-0.81371	0.774238	0.735037	
Calcium	-0.66497	0.081552	-0.76845	0.025689	0.705716	0.654434	-0.58245		-0.34126	-0.483	-0.57392	-0.84641	0.333867	-0.50524	-0.73764	
Anion_Ga	0.850187	-0.9086819	0.521882	0.108008	-0.5132	0.458172	0.940525	-0.34126		-0.07775	-0.07775	0.448867	-0.9176	0.700693	0.505296	
Albumin	0.356115	0.4625101	-0.11477	0.771311	-0.19857	-0.6333	0.213503	-0.483	-0.07775		-0.41177	0.386289	0.129135	0.520191	0.801427	
Alkaline_P	0.324159	-0.4986886	0.816113	-0.66234	-0.68617	-0.03226	0.402337	-0.57392	0.448867	-0.41177		0.602745	-0.57021	0.162182	0.055662	
AST	0.278351	0.1740204	0.495922	-0.05565	-0.84513	-0.62985	0.251075	-0.84641	0.080208	0.386289	0.602745		-0.28491	0.453669	0.538073	
ALT	-0.67533	0.8014643	-0.41918	-0.08724	0.738999	-0.47175	-0.81371	0.333867	-0.9176	0.129135	-0.57021	-0.28491		-0.76979	-0.45204	
Bilirubin_T	0.732118	-0.3543169	0.170042	0.62413	-0.7475	0.06051	0.774238	-0.50524	0.700693	0.520191	0.162182	0.453669	-0.76979		0.862485	
Protein_T	0.804563	-0.112467	0.316342	0.626801	-0.59273	-0.37275	0.735037	-0.73764	0.505296	0.801427	0.055662	0.538073	-0.45204	0.862485		
(x)																

Table 14 Correlation coefficient of NICMP predictive model output (n=5)

4.1.2 *Response and Error*

In addition to statistical analysis describing the predictive model, the error histogram and response charts for each metabolic parameter provides the graphical representation of the model output. Figures 9-68 displays the NICMP *beta* and *one* predictive model error histogram and response plots, relative to the target output values. The graphs are a result of the machine learning analysis in MATLAB, and relate to the machine learning output data in Table 5.

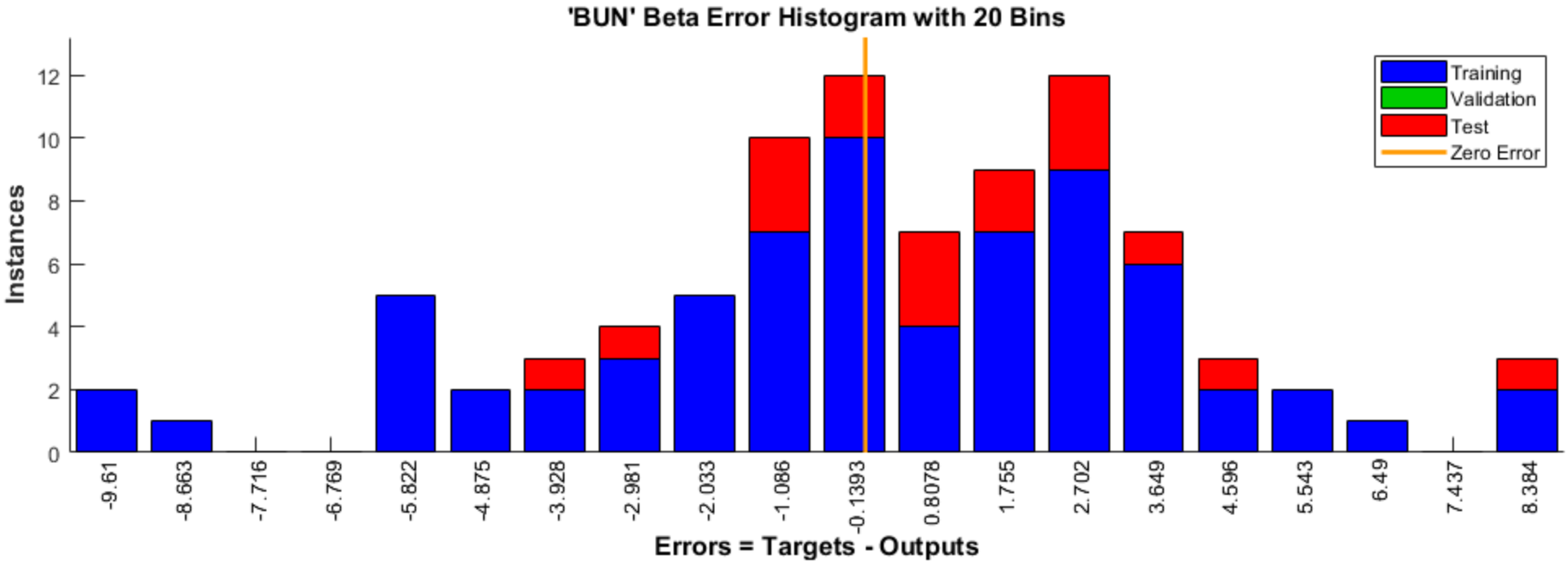

Figure 9. BUN beta error histogram

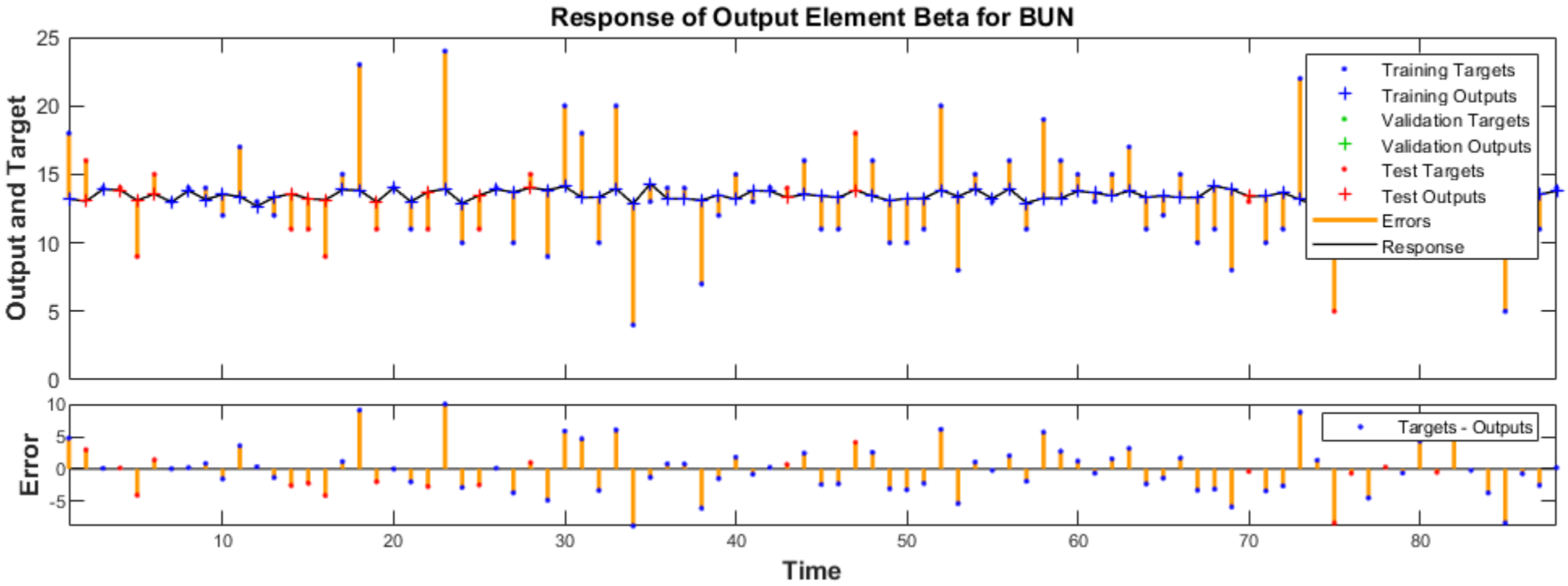

Figure 10 BUN beta response and error plot

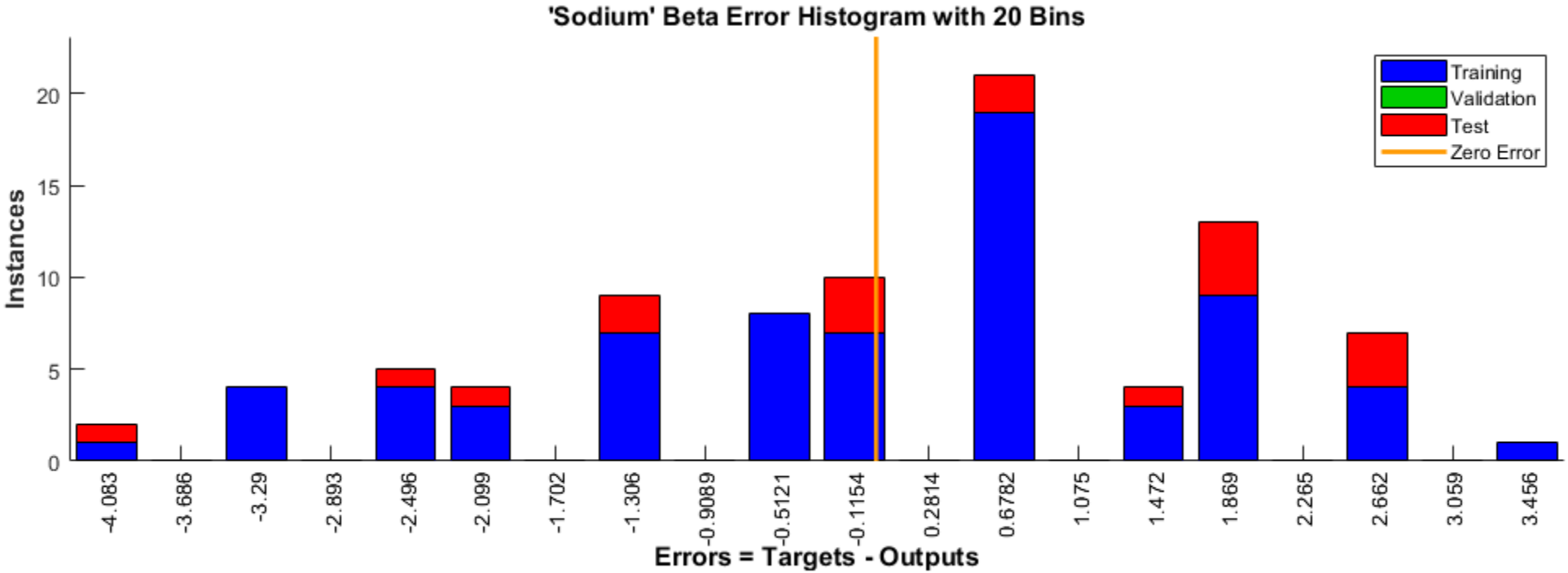

Figure 11 Sodium beta error histogram

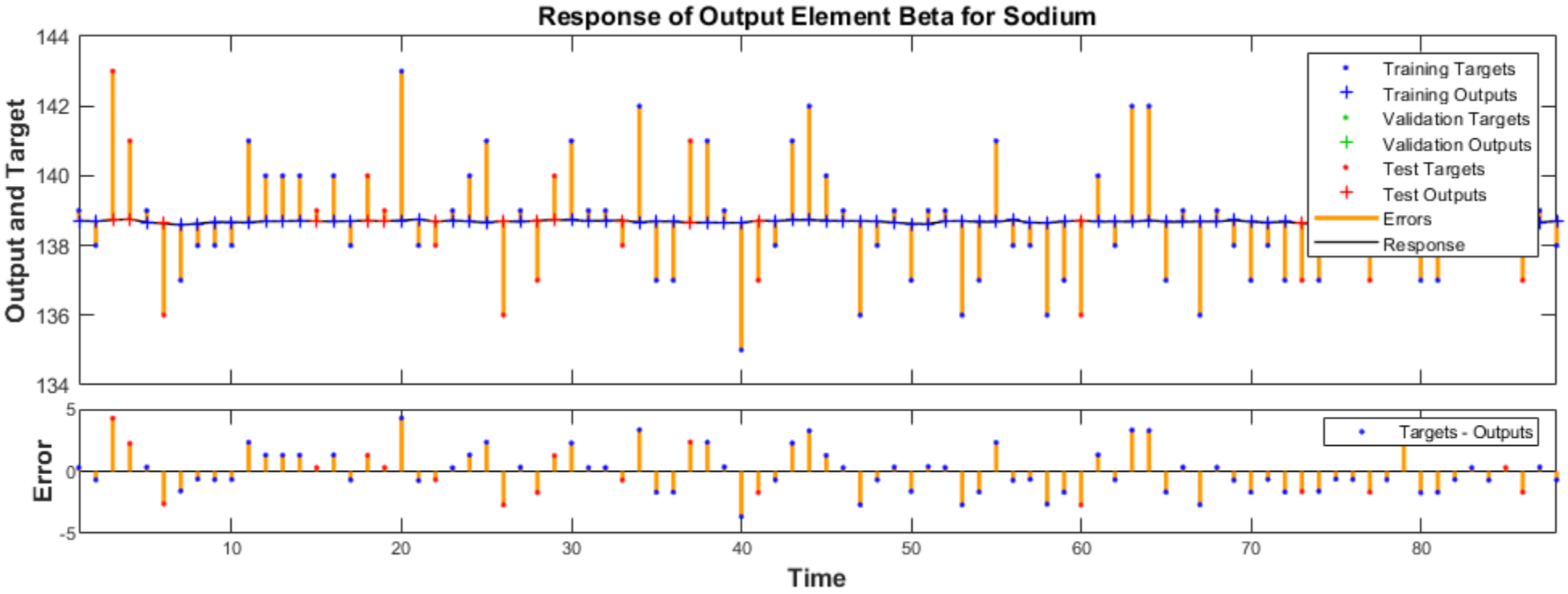

Figure 12 Sodium beta repsonse and error plot

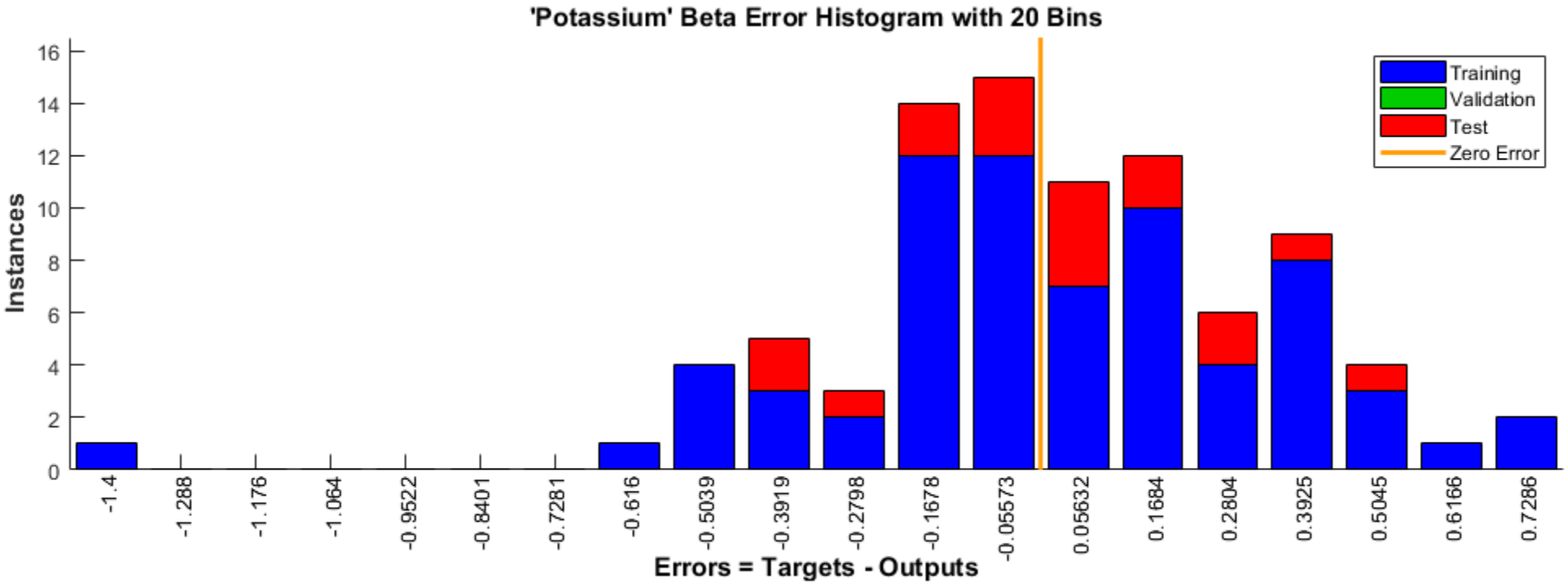

Figure 13 Potassium beta error histogram

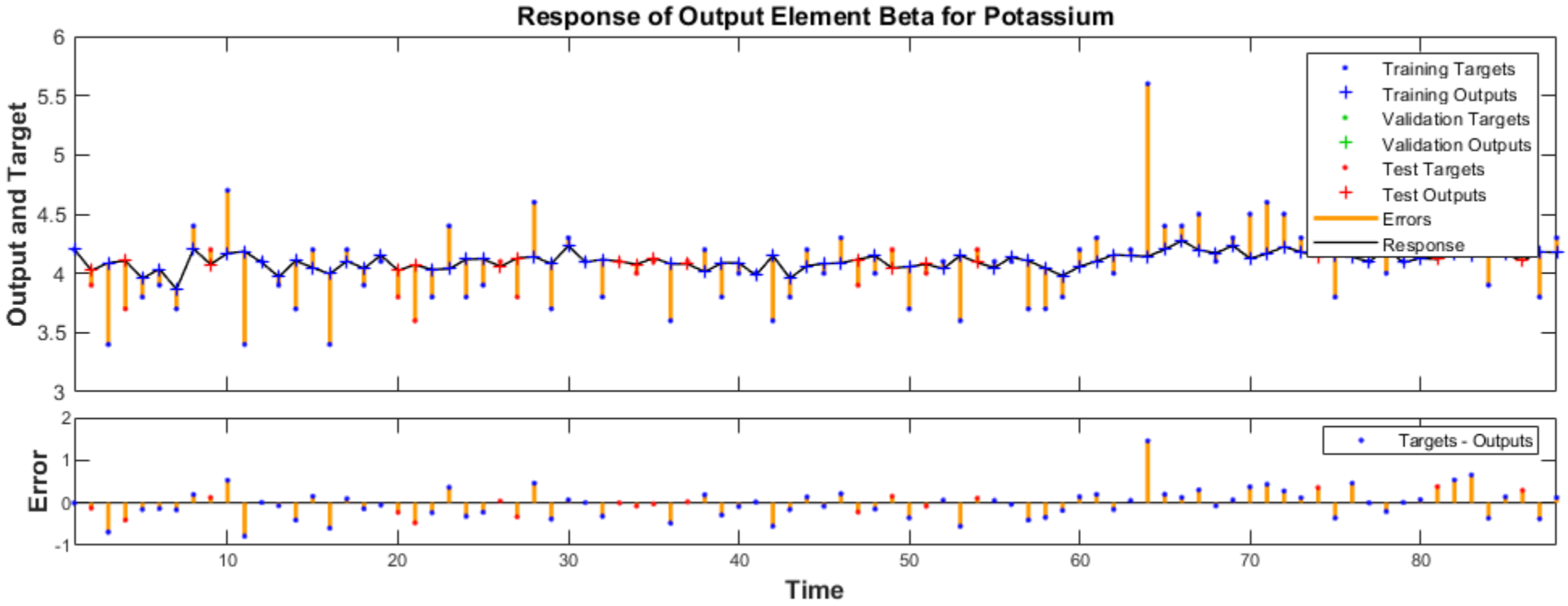

Figure 14 Potassium beta response and error plot

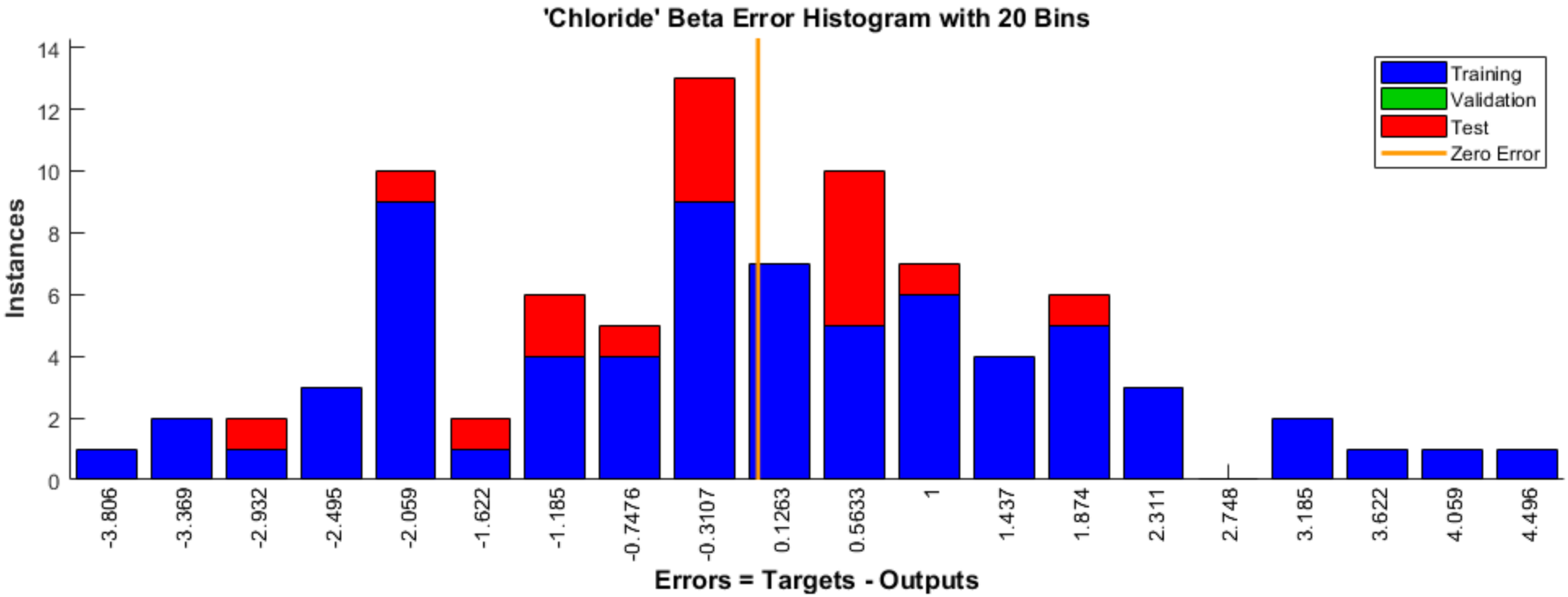

Figure 15 Chloride beta error histogram

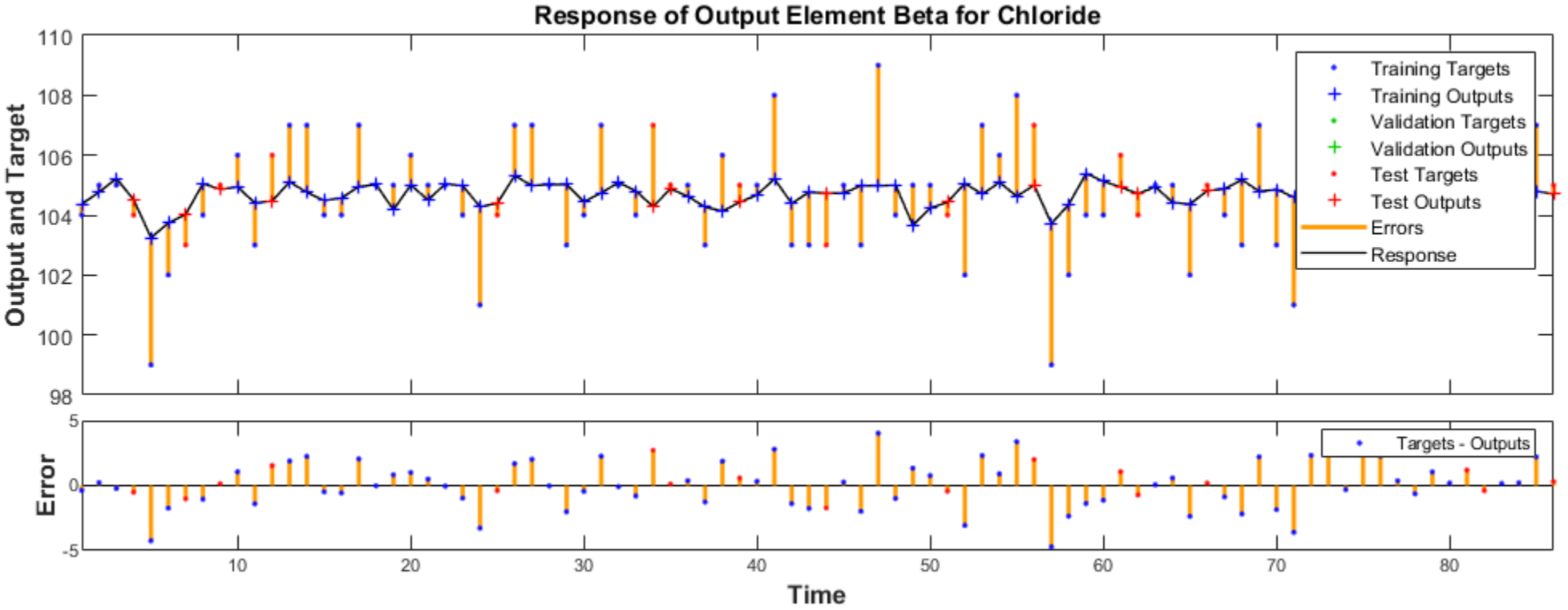

Figure 16 Chloride beta response and error plot

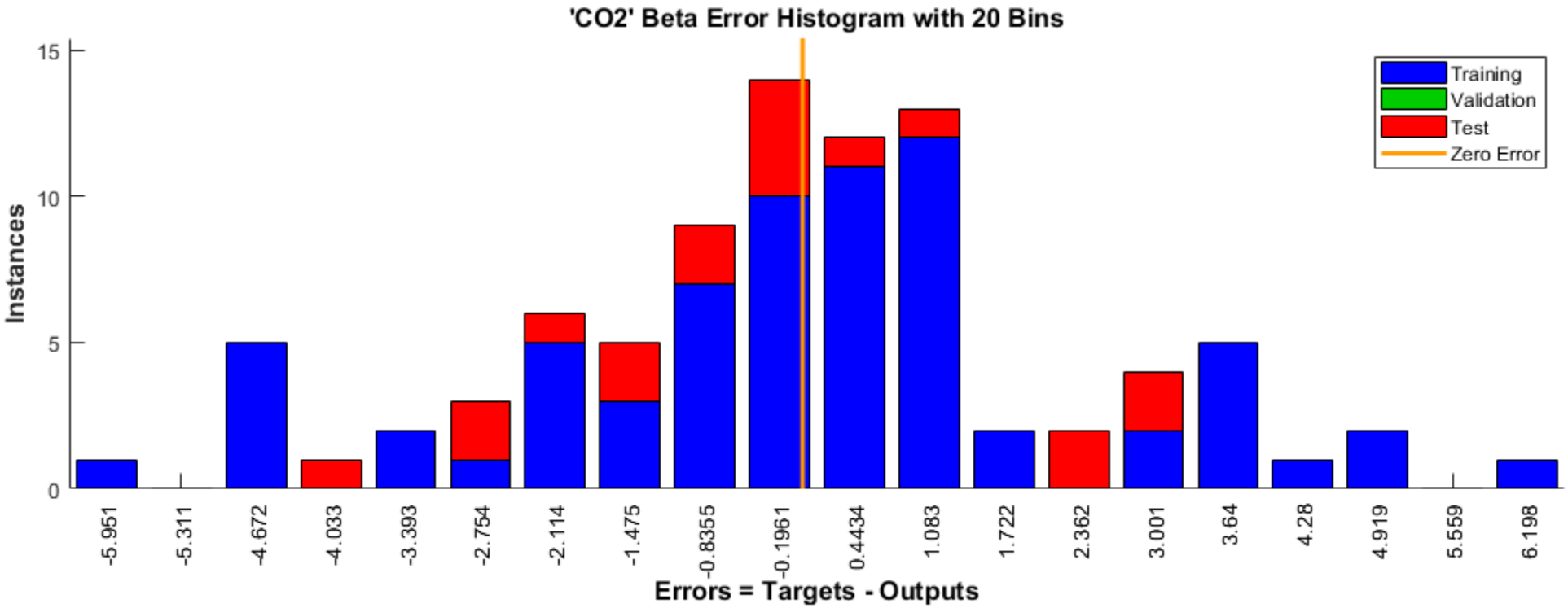

Figure 17 CO2 beta error histogram

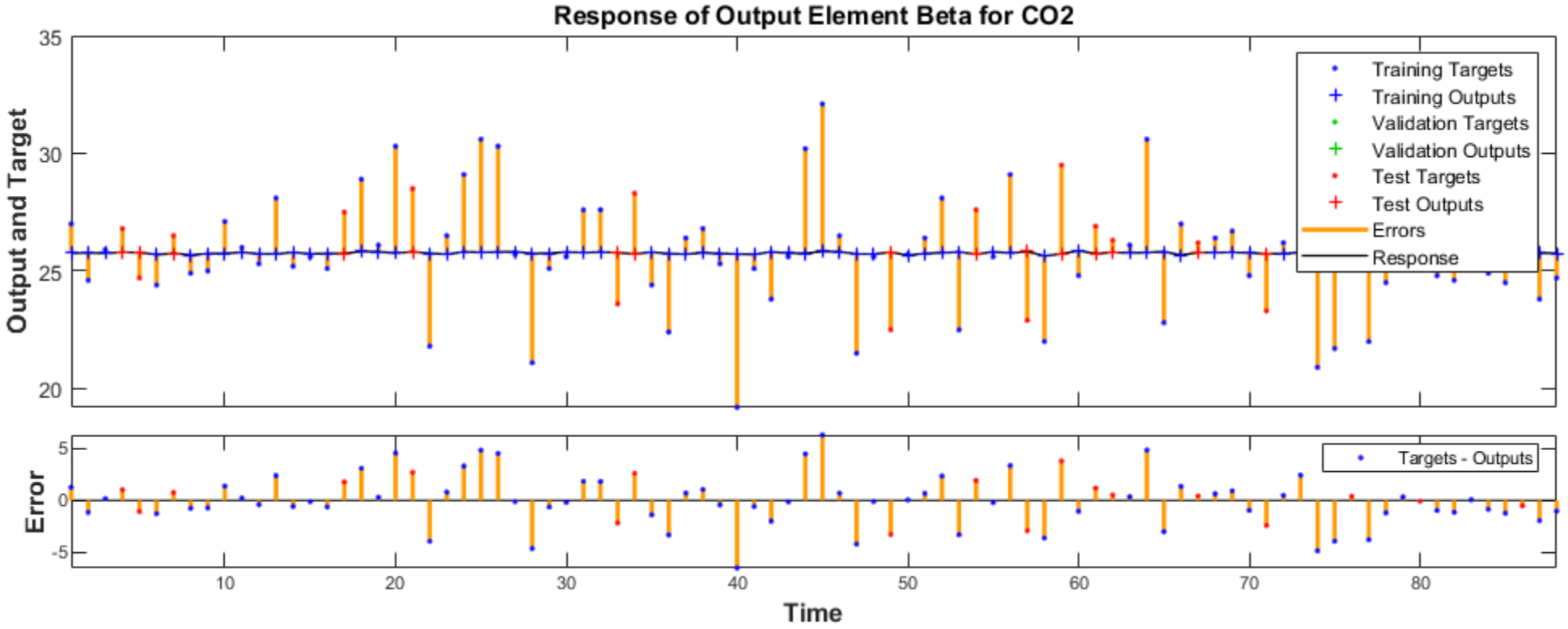

Figure 18 CO2 beta response and error plot

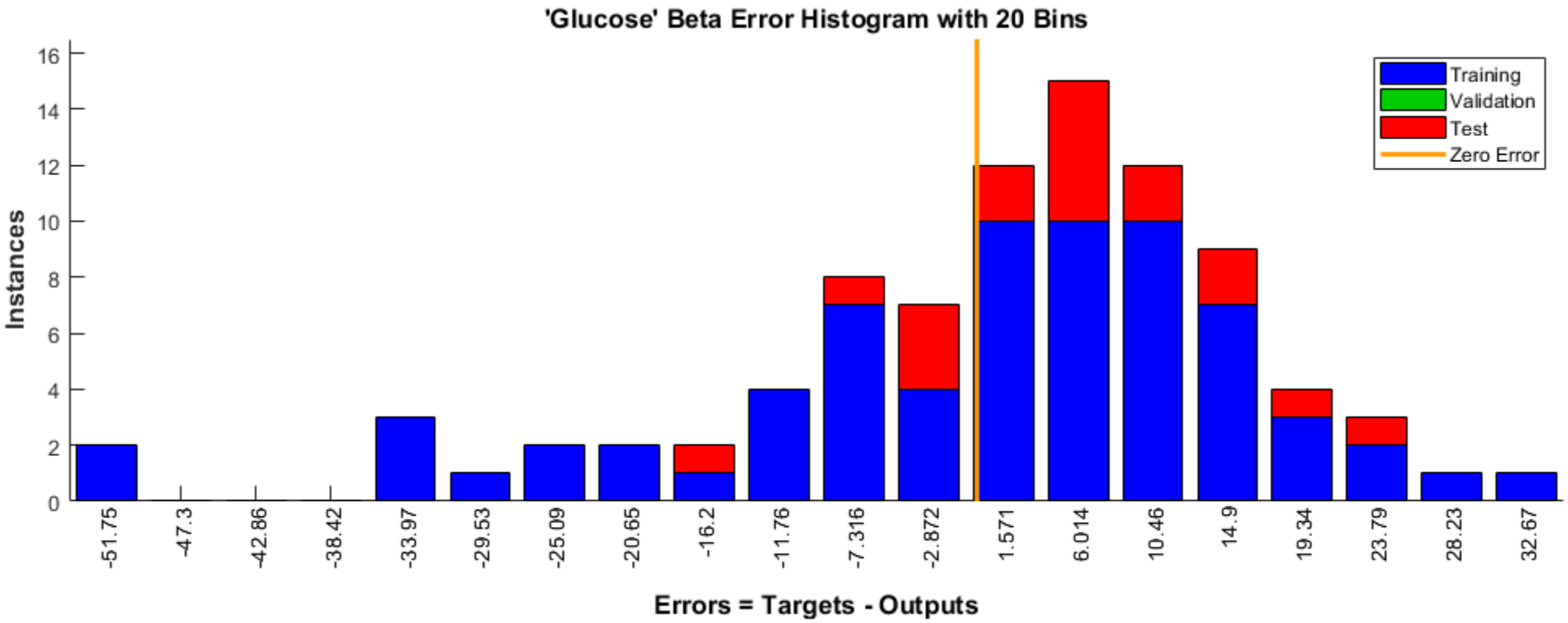

Figure 19 Glucose beta error histogram

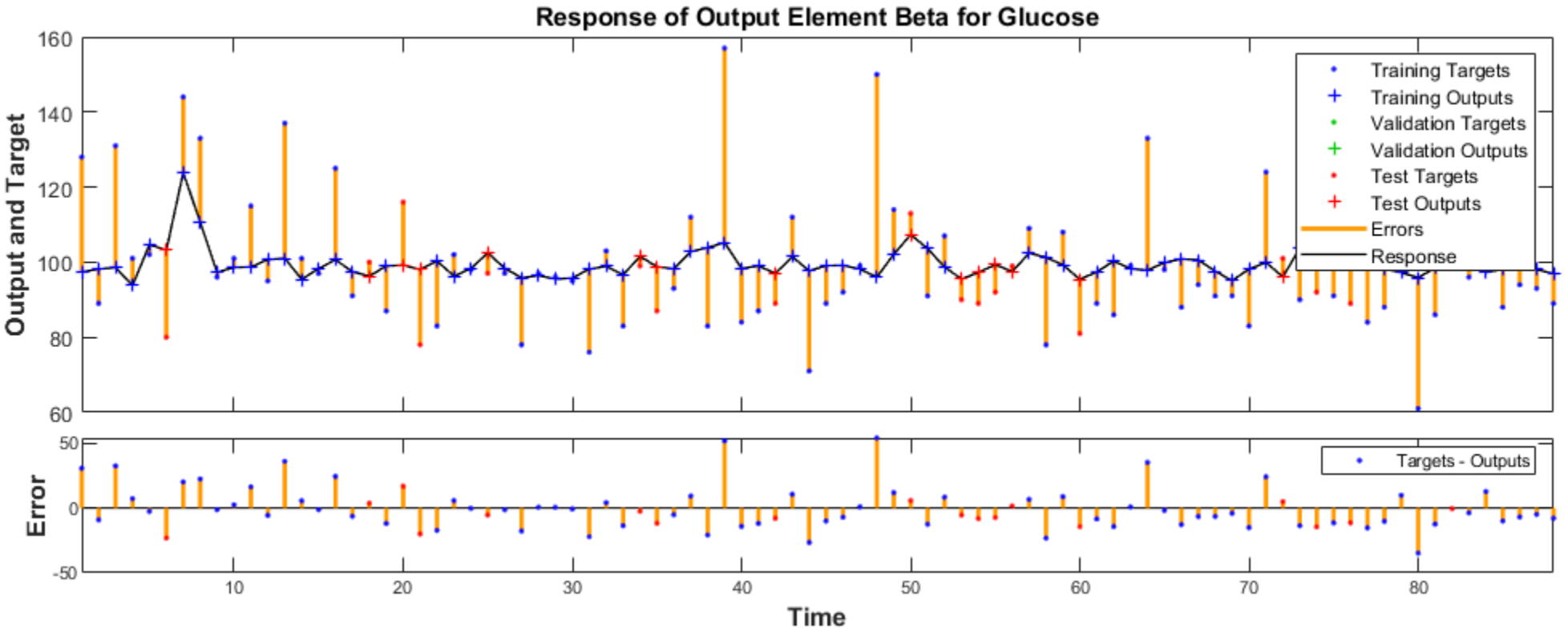

Figure 20 Glucose beta response and error plot

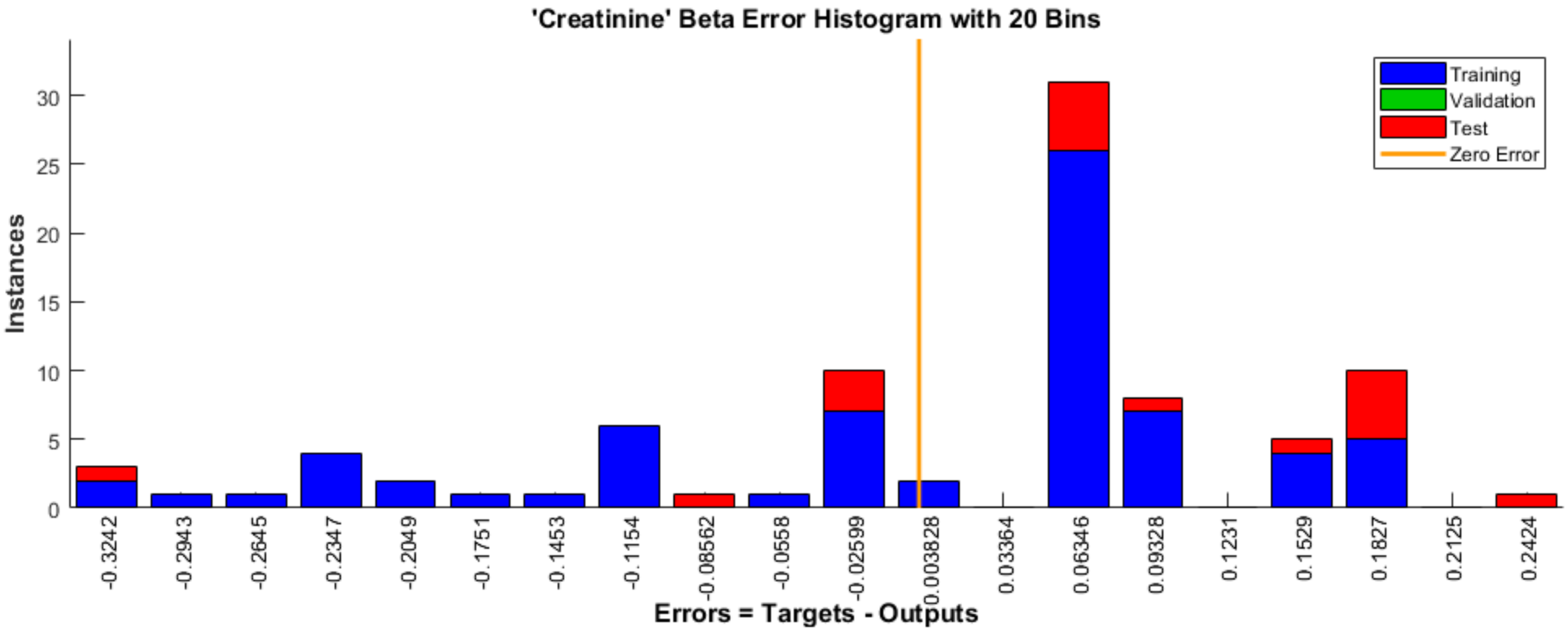

Figure 21 Creatinine beta error histogram

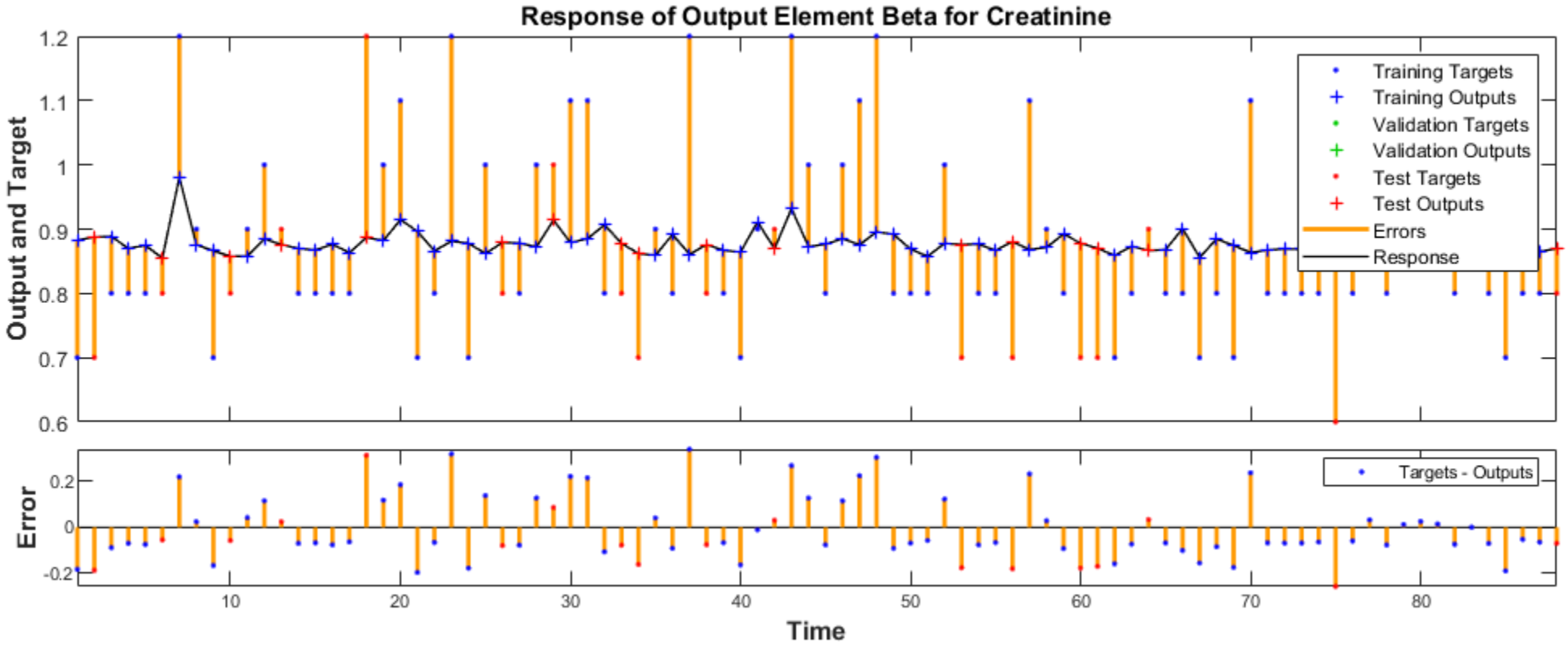

Figure 22 Creatinine beta response and error plot

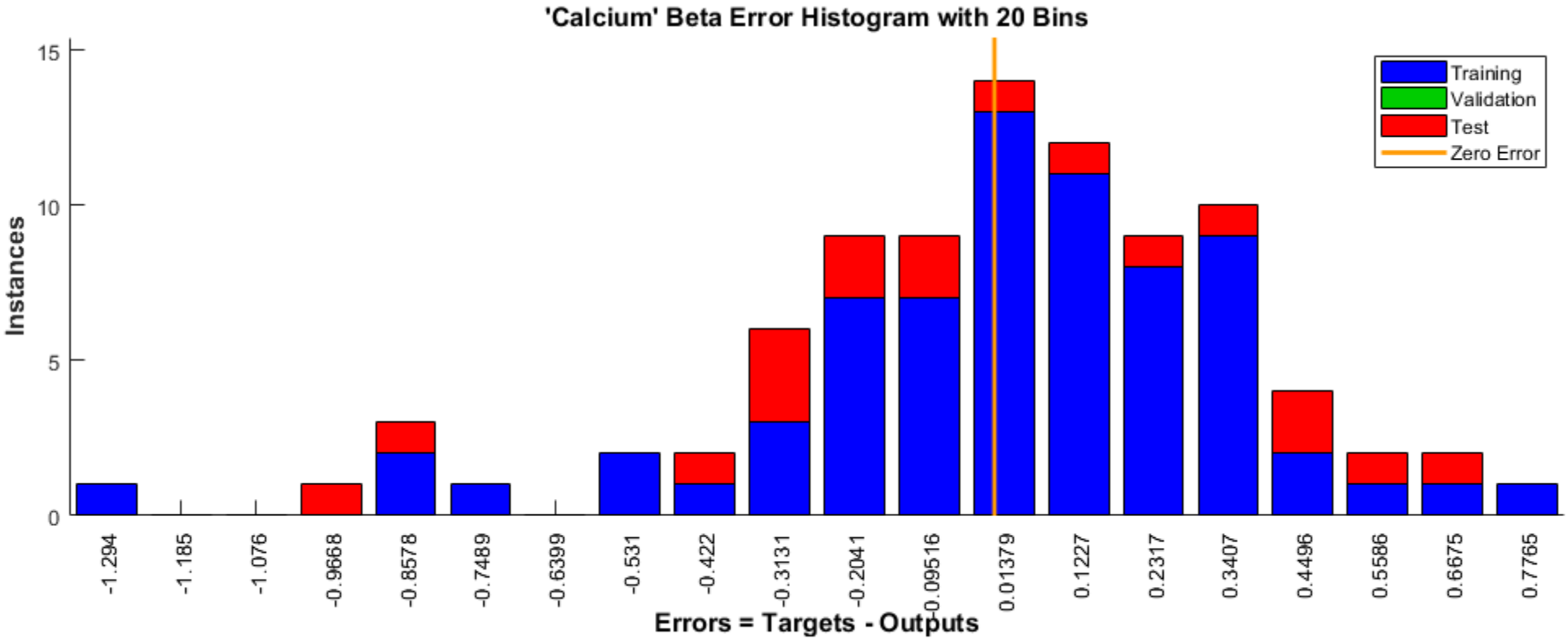

Figure 23 Calcium beta error histogram

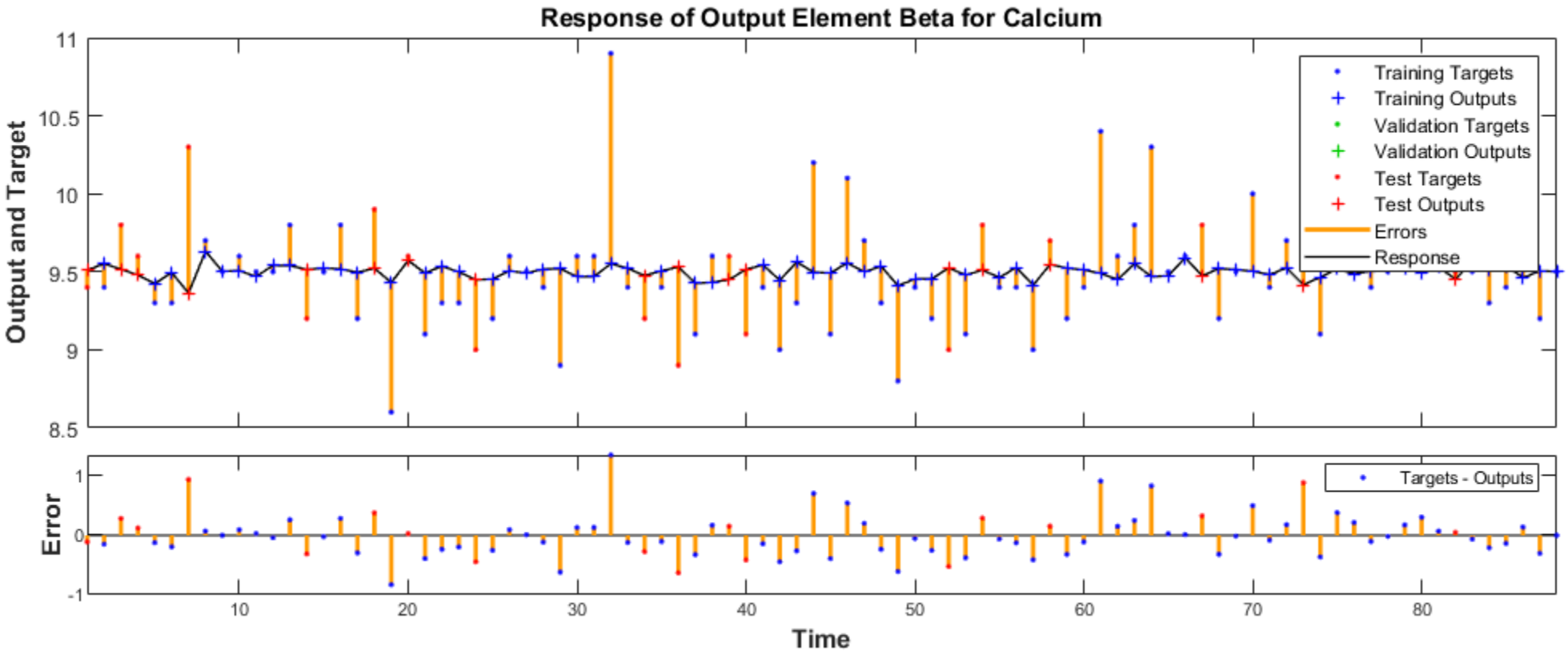

Figure 24 Calcium beta response and error plot

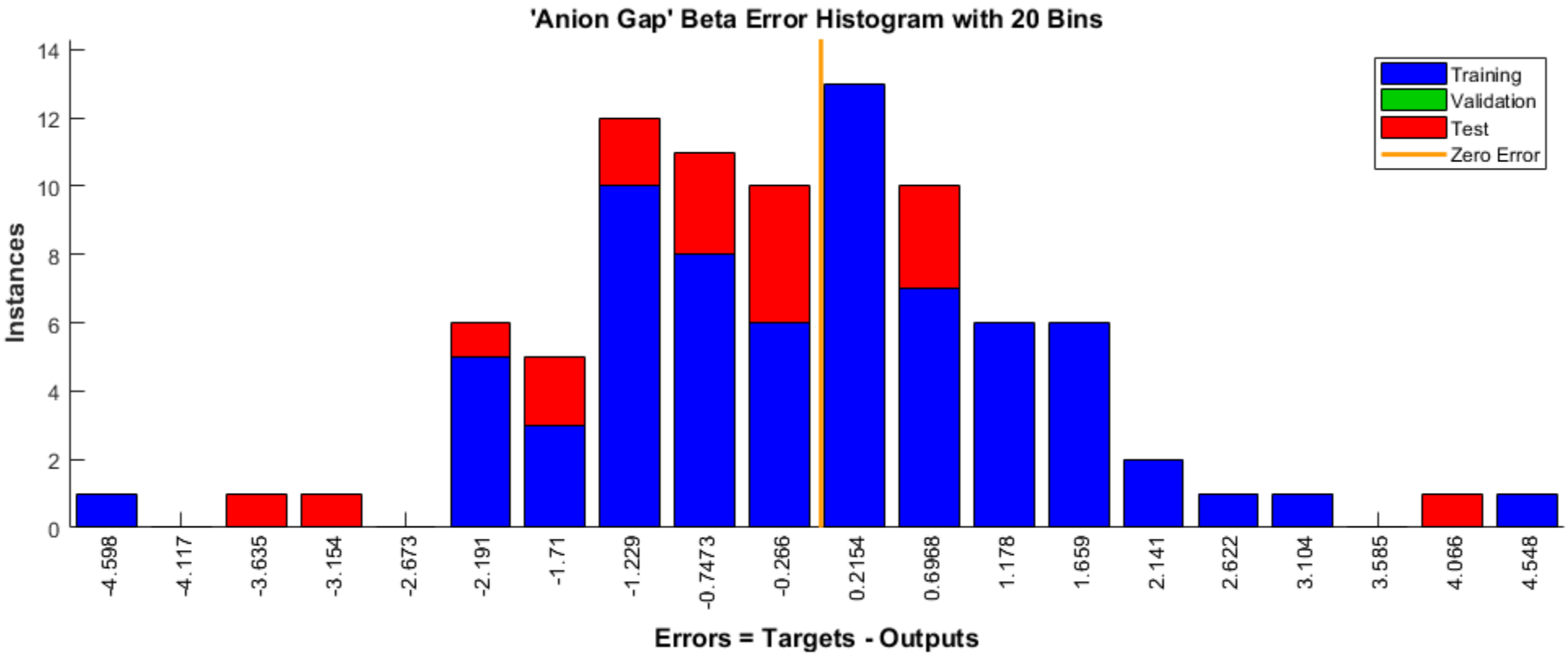

Figure 25 Anion Gap beta error histogram

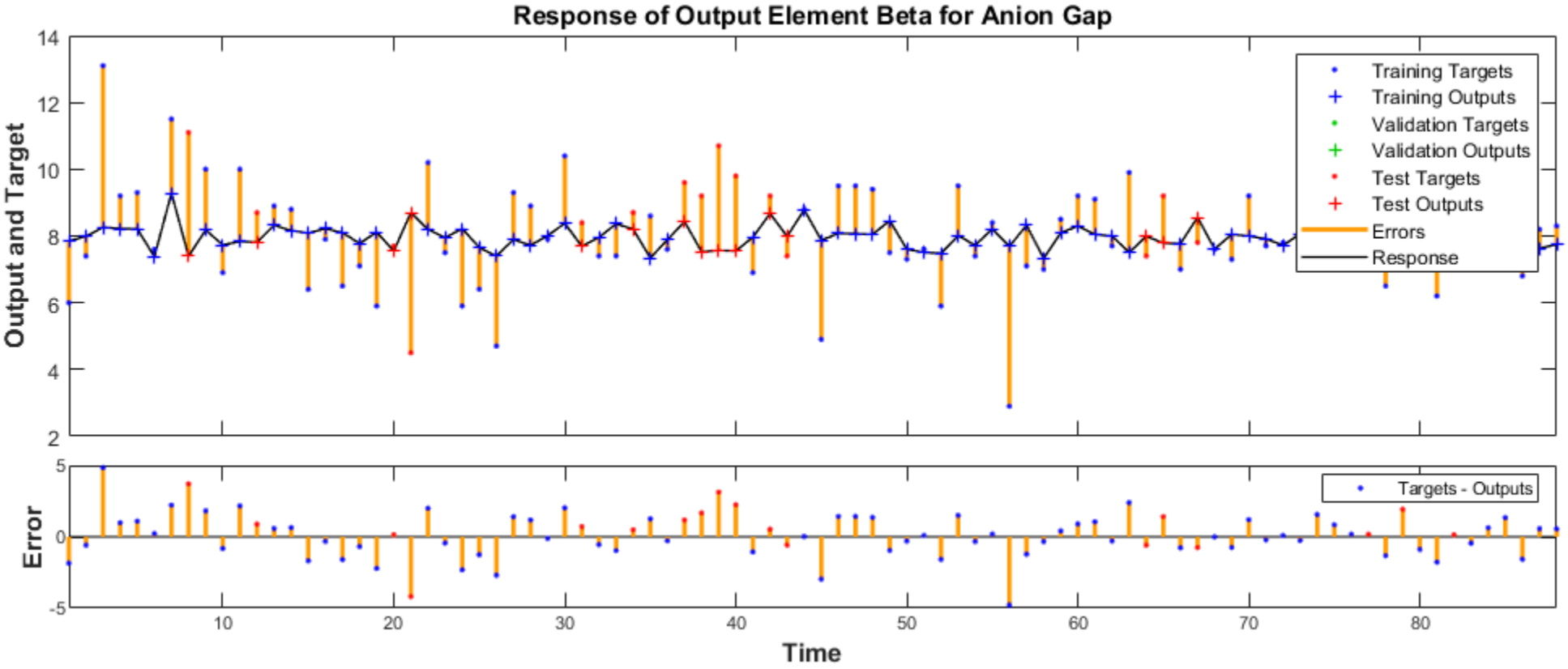

Figure 26 Anion Gap beta response and error plot

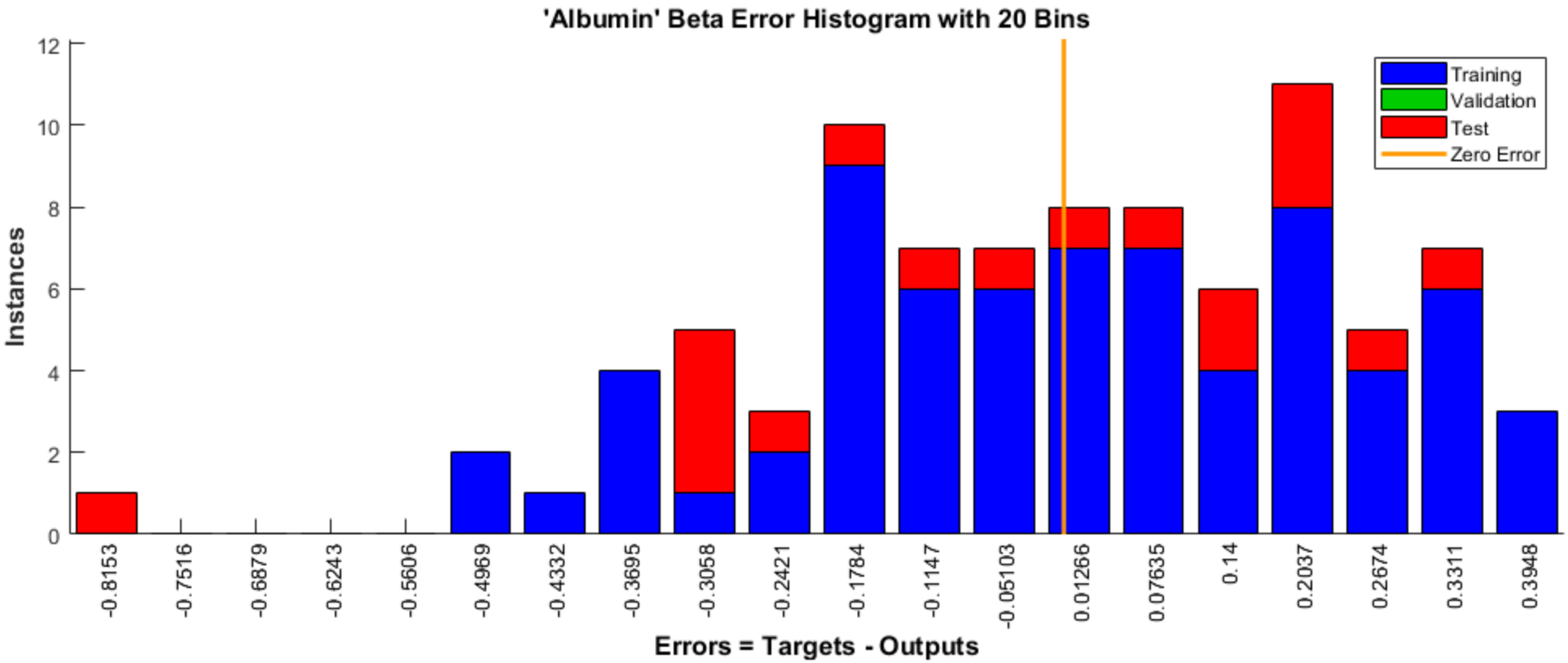

Figure 27 Albumin beta error histogram

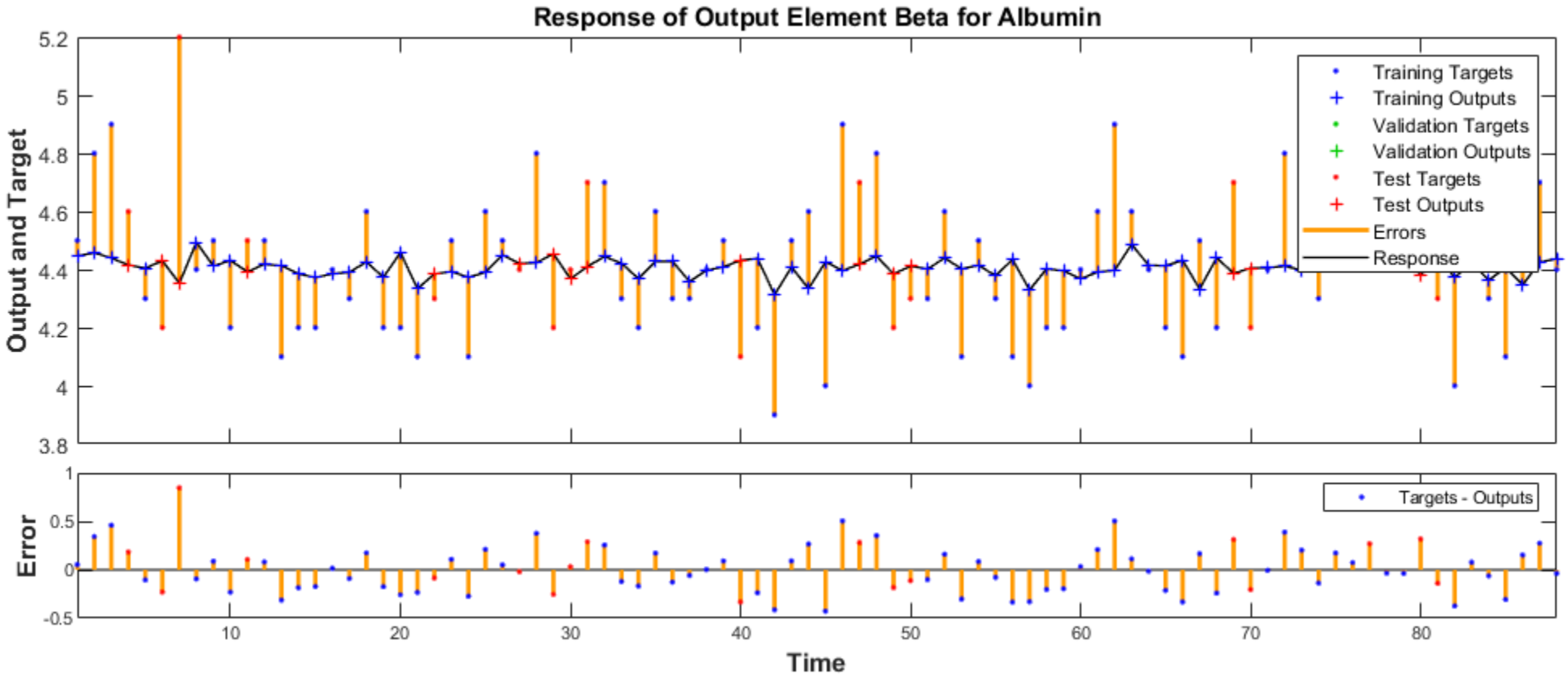

Figure 28 Albumin beta response and error plot

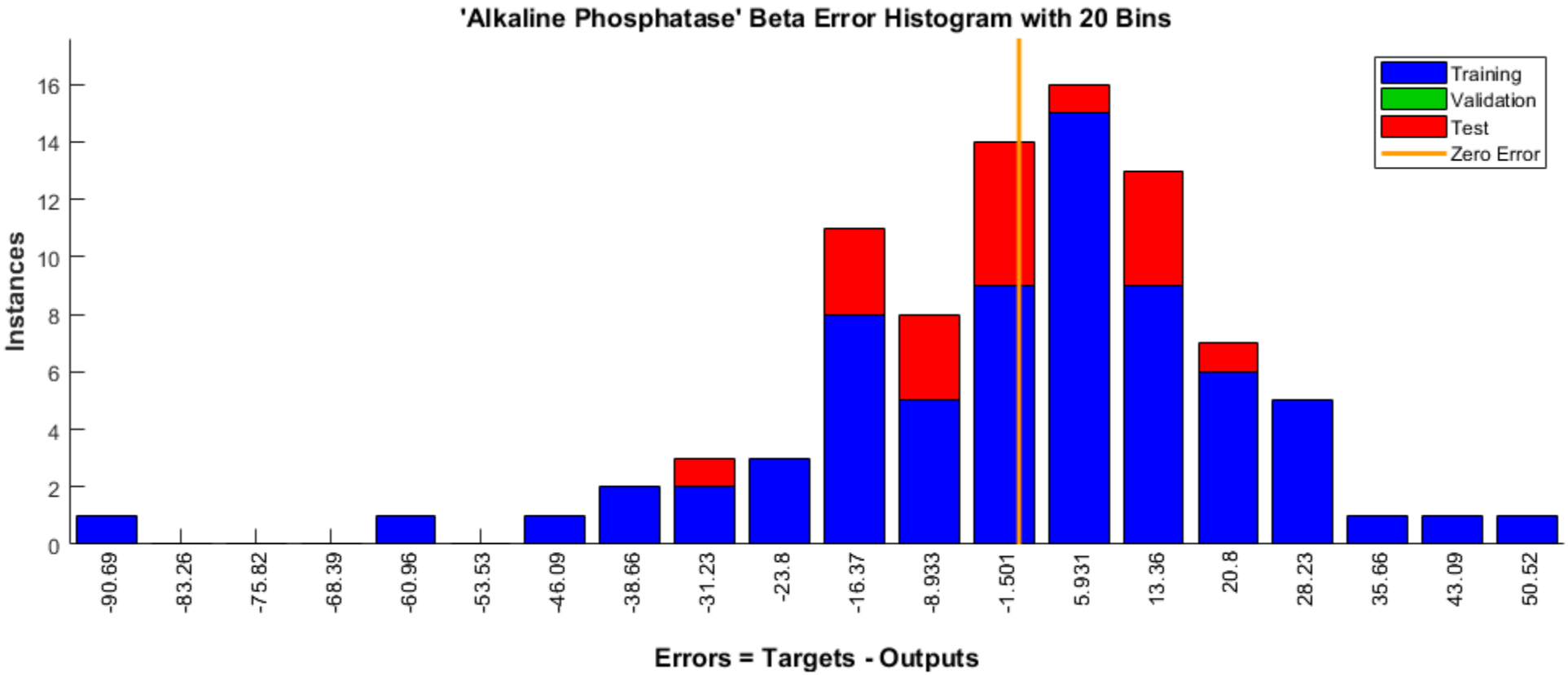

Figure 29 Alkaline Phosphatase beta error histogram

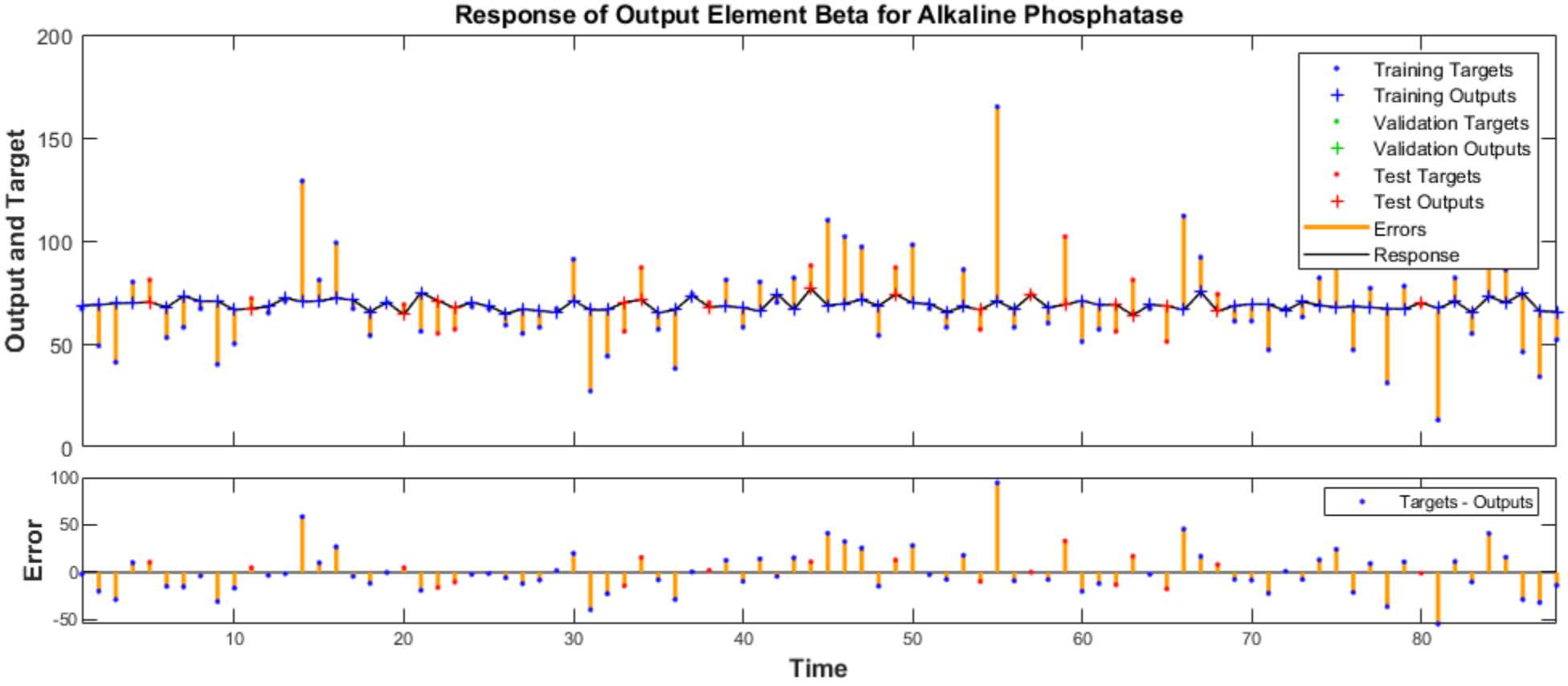

Figure 30 Alkaline Phosphatase beta response and error plot

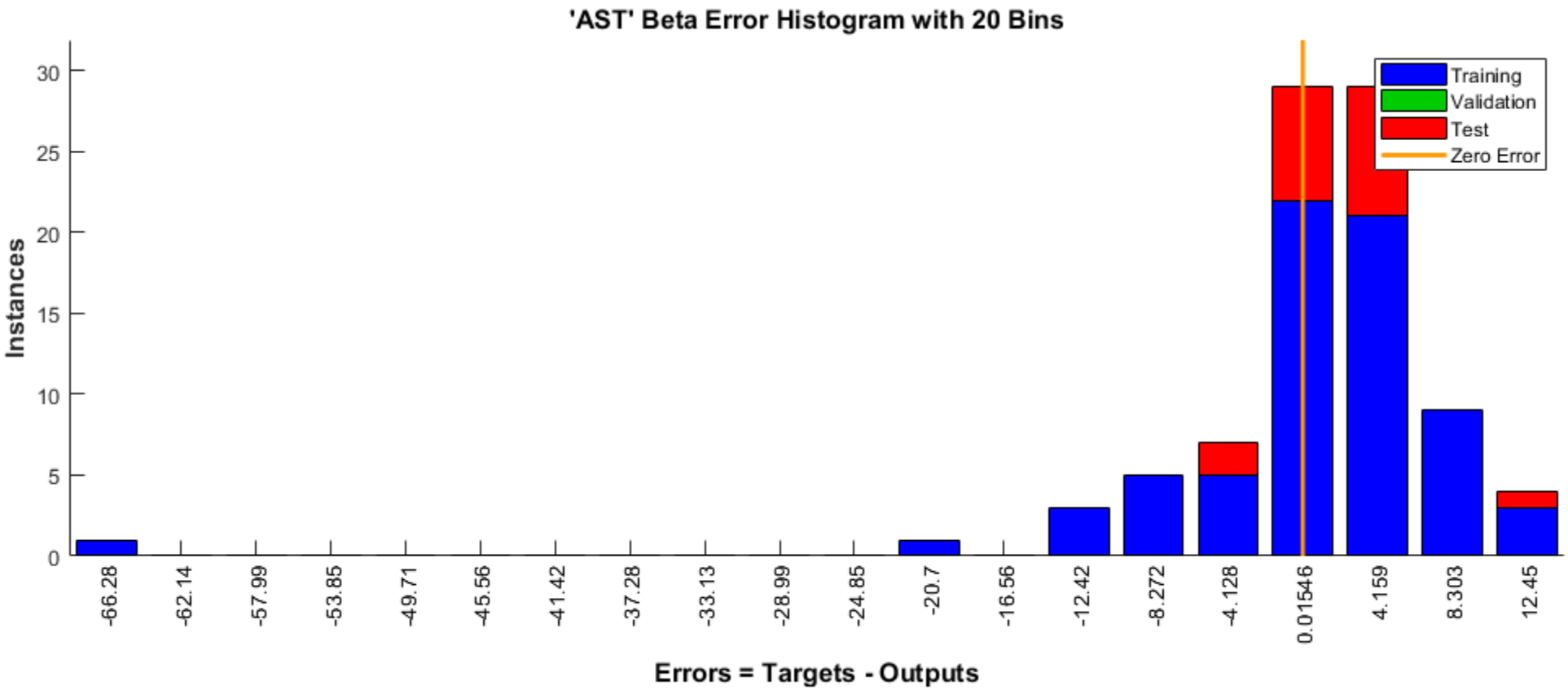

Figure 31 AST beta error histogram

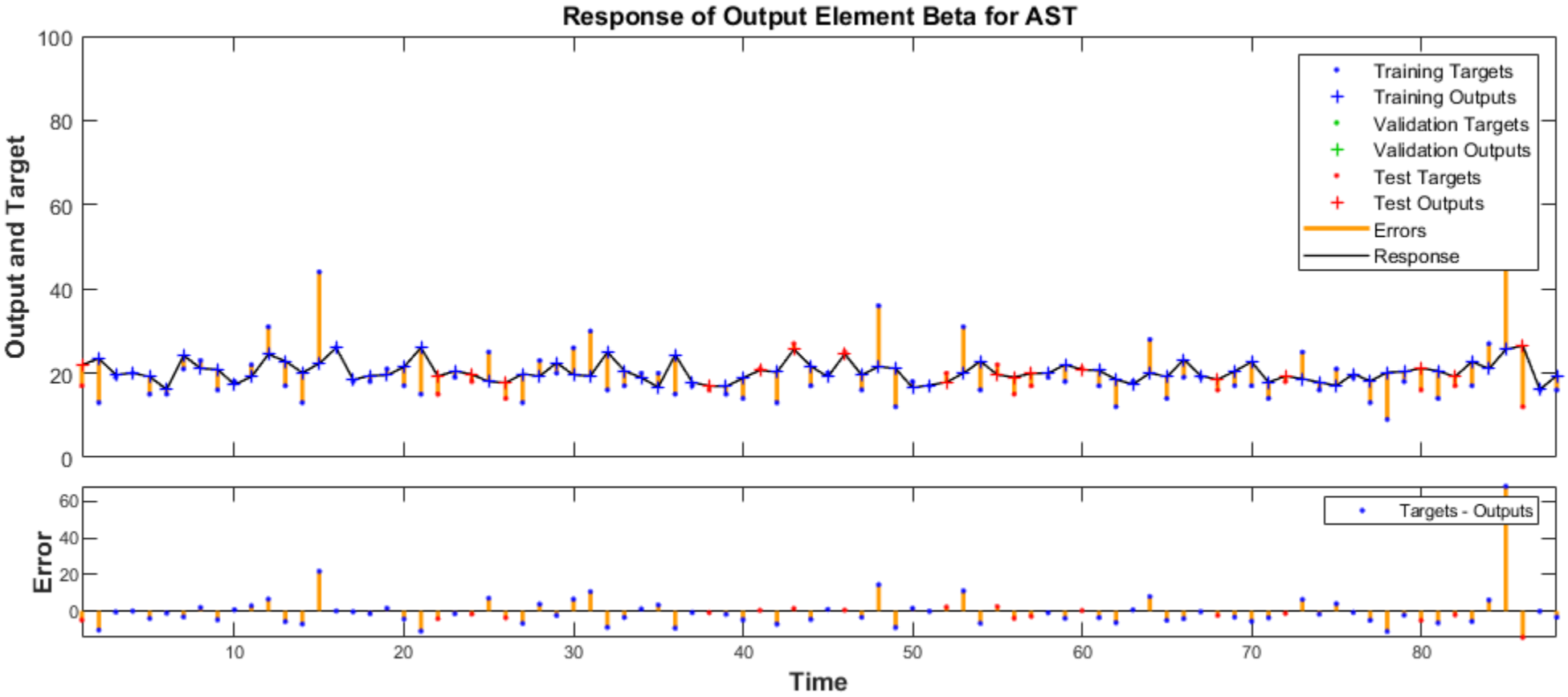

Figure 32 AST beta response and error plot

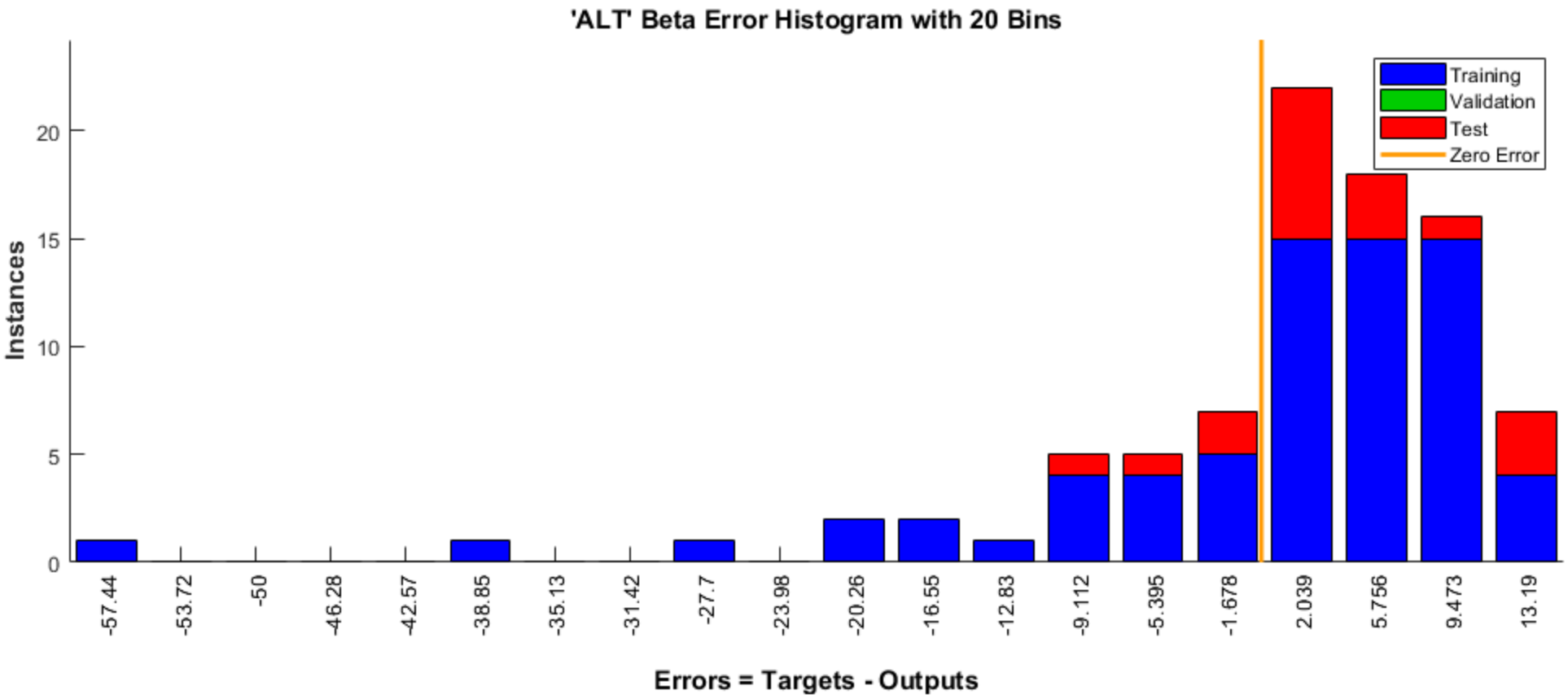

Figure 33 ALT beta error histogram

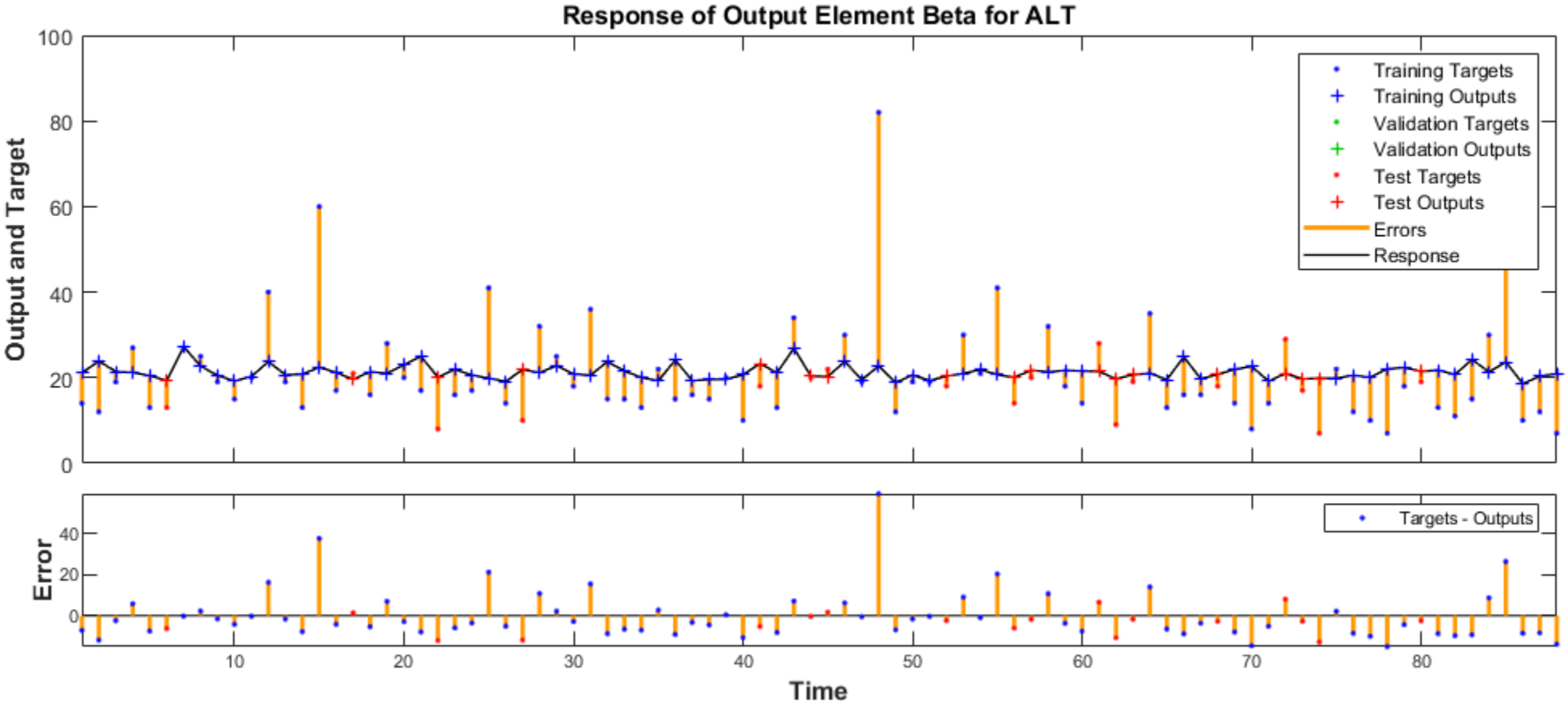

Figure 34 ALT beta response and error plot

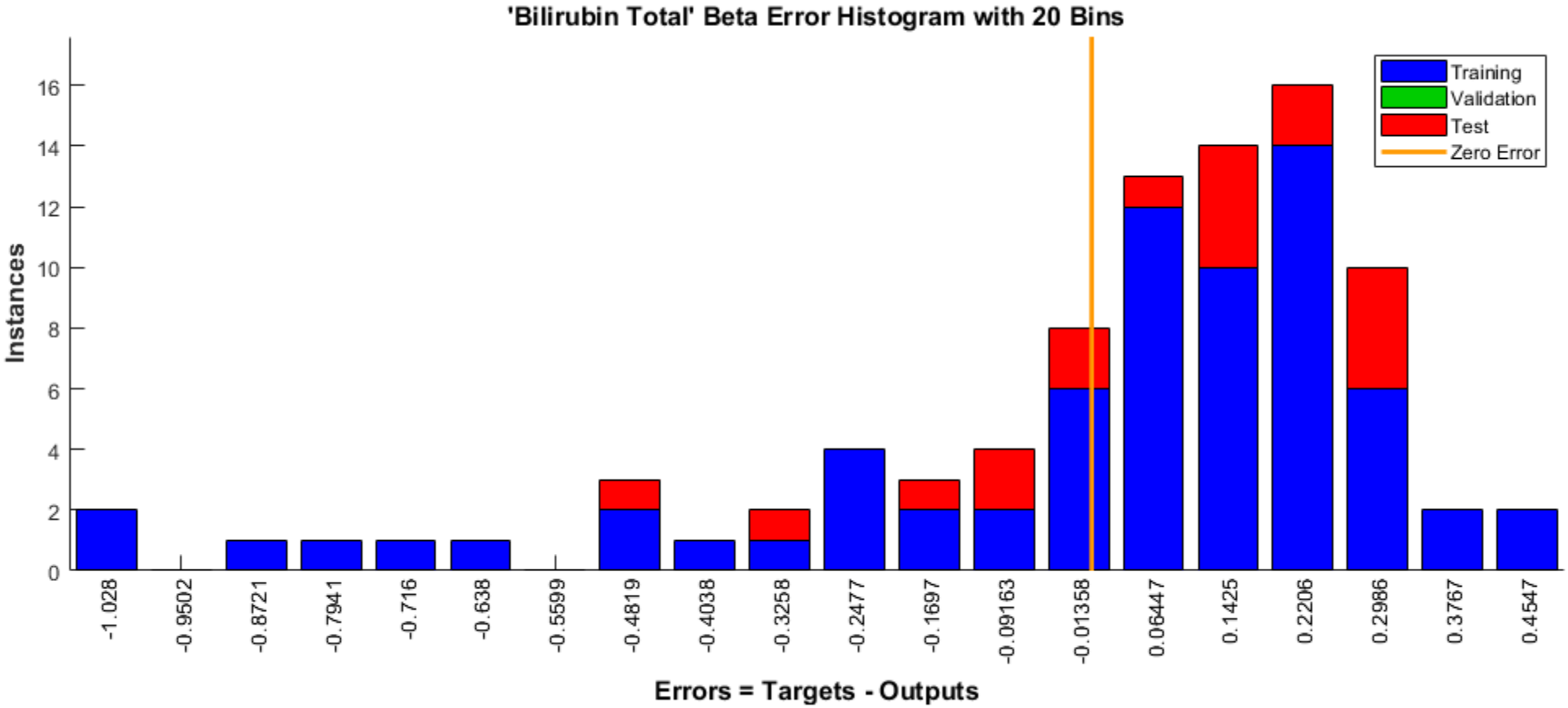

Figure 35 Bilirubin Total beta error histogram

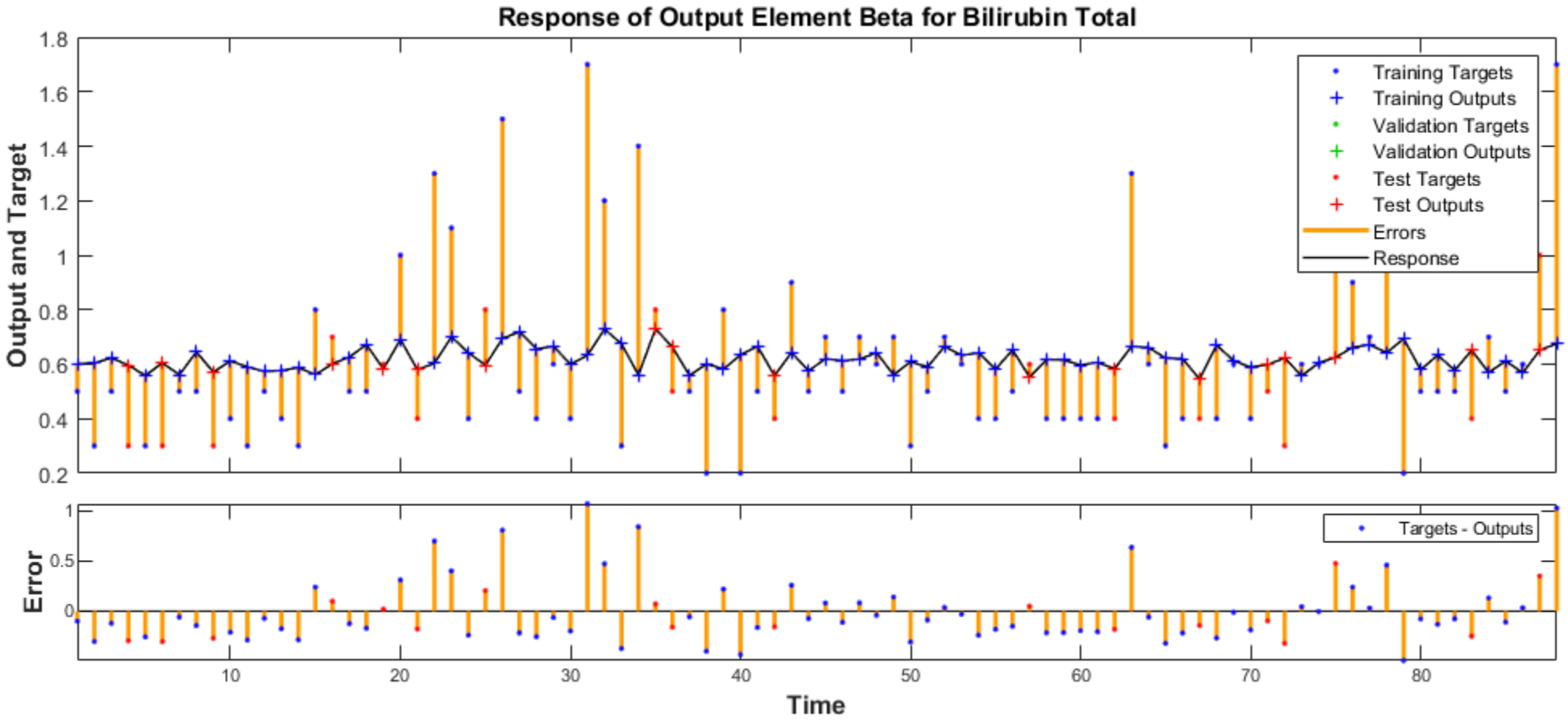

Figure 36 Bilirubin Total beta response and error plot

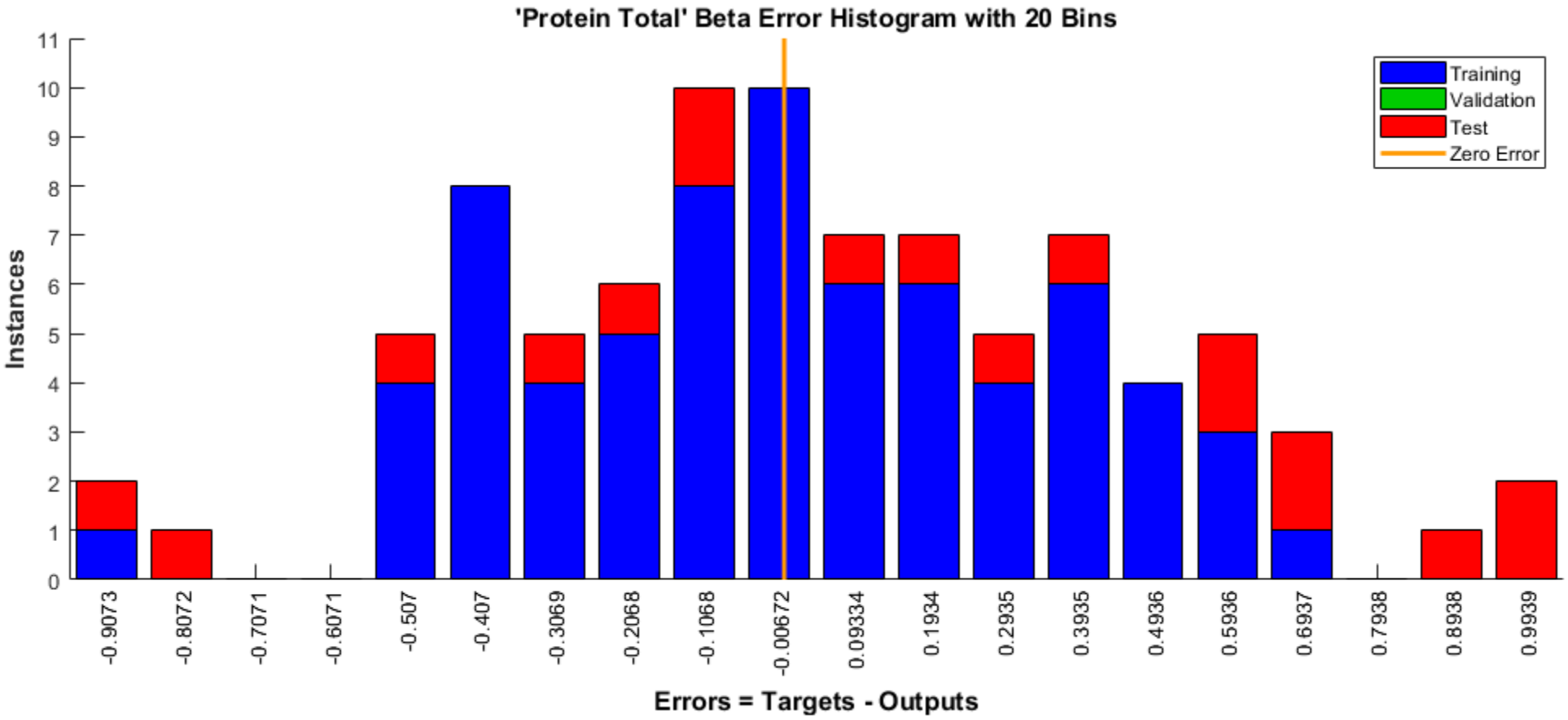

Figure 37 Protein Total beta error histogram

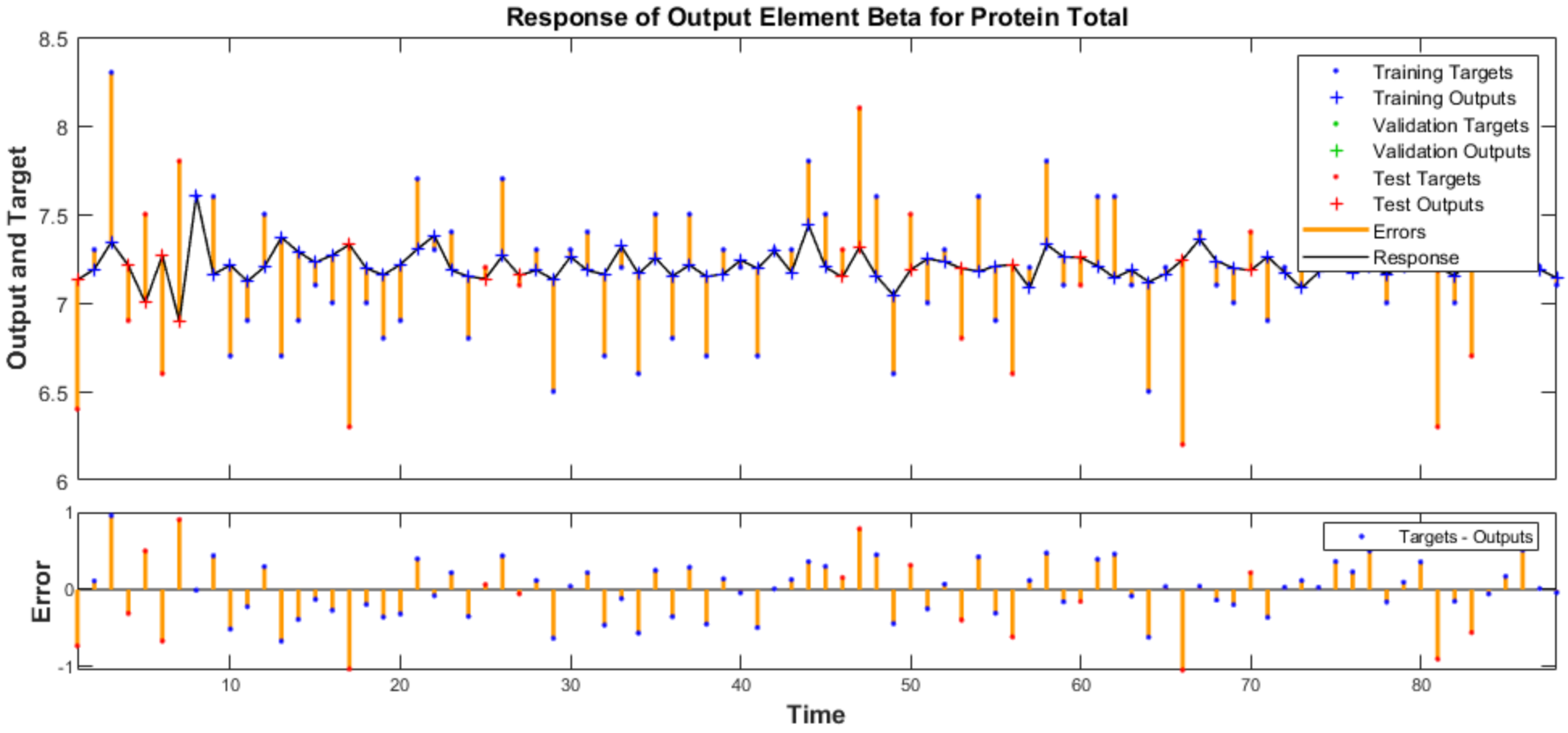

Figure 38 Protein Total beta response and error plot

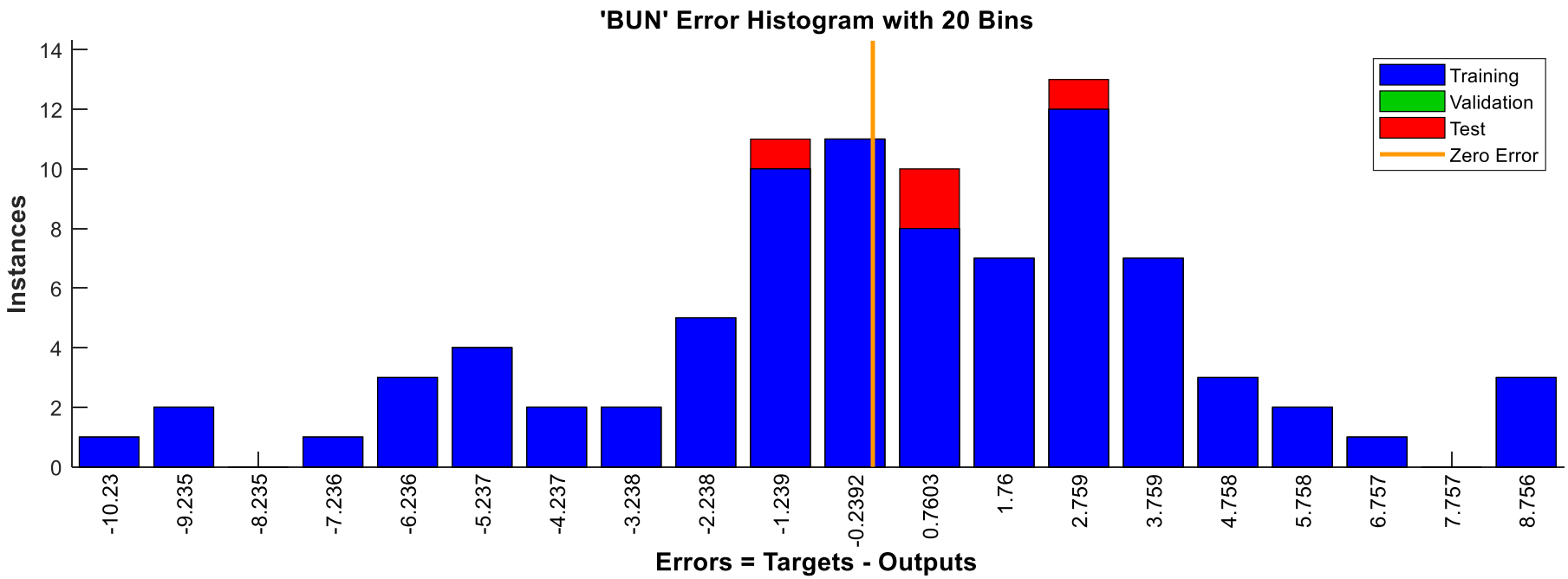

Figure 39. BUN error histogram

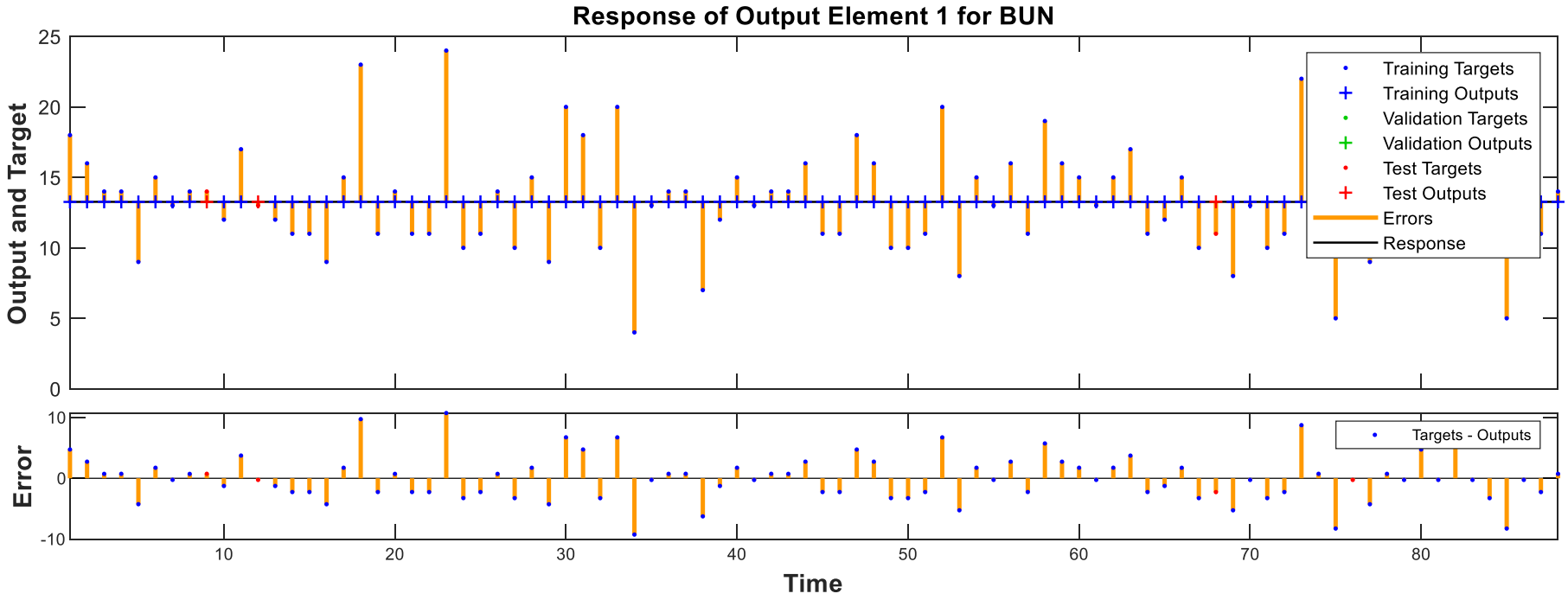

Figure 40. BUN response and error plot

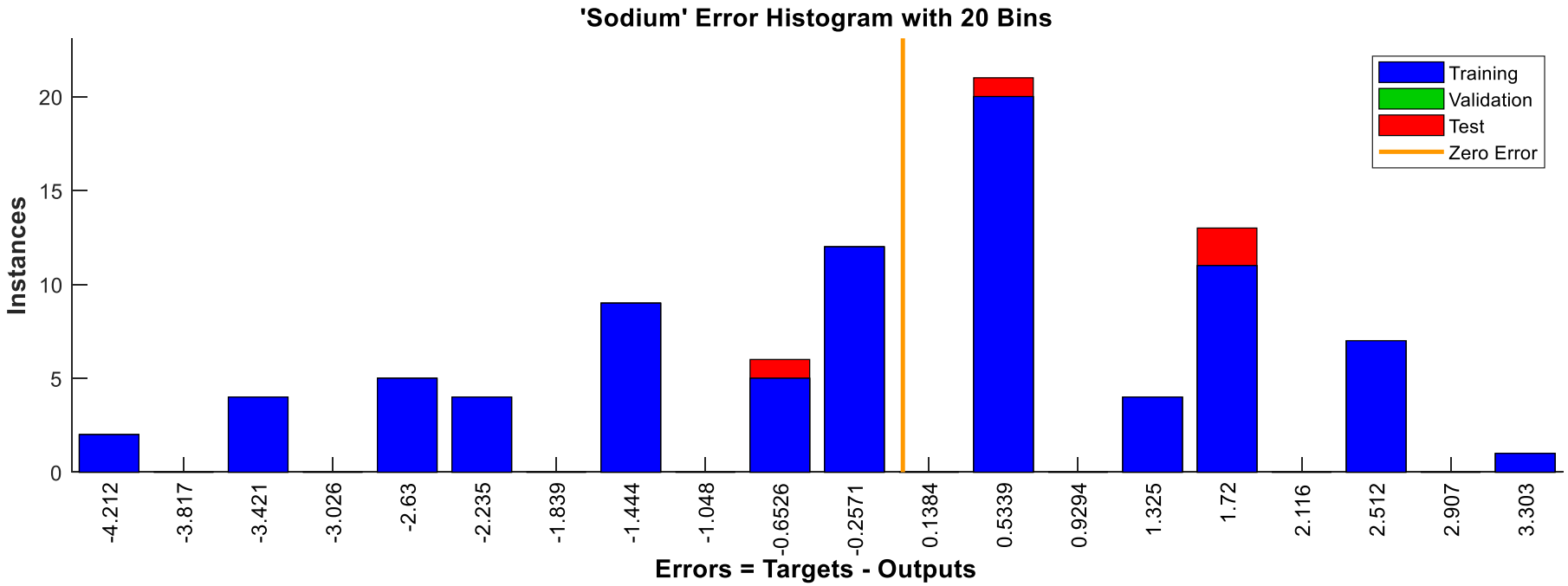

Figure 41. Sodium error histogram

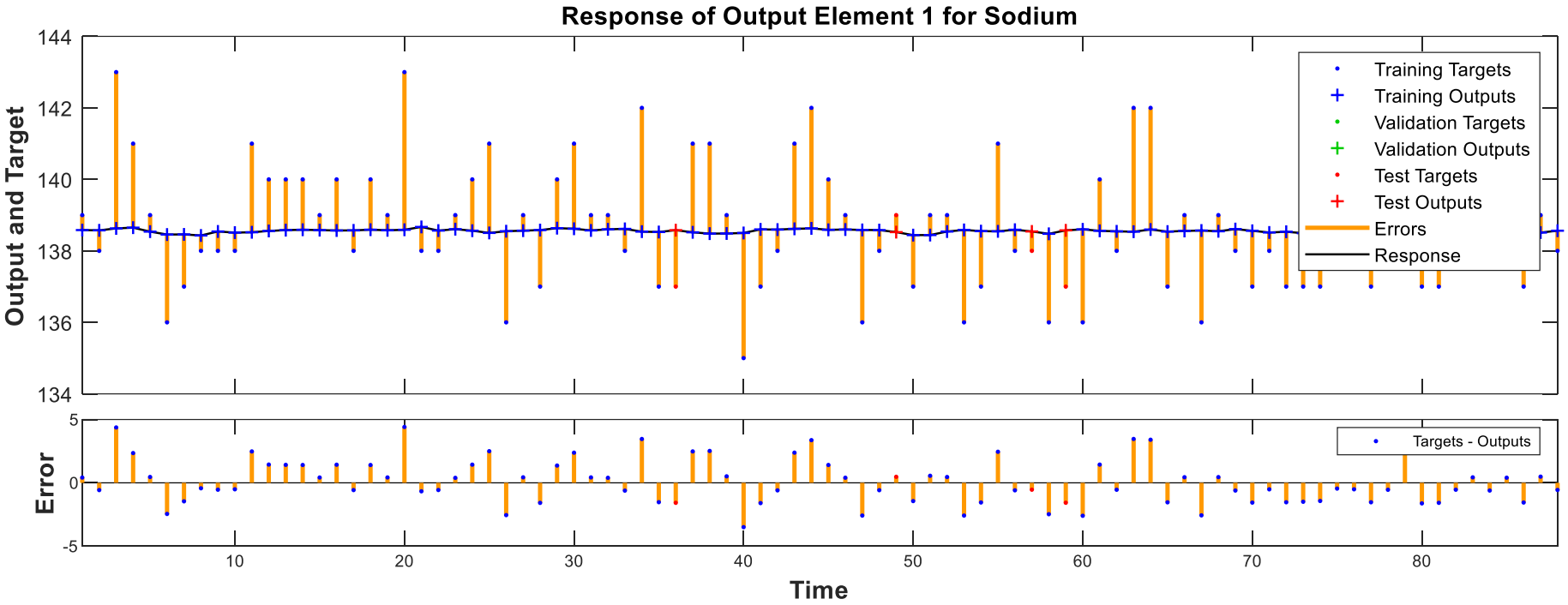

Figure 42. Sodium response and error plot

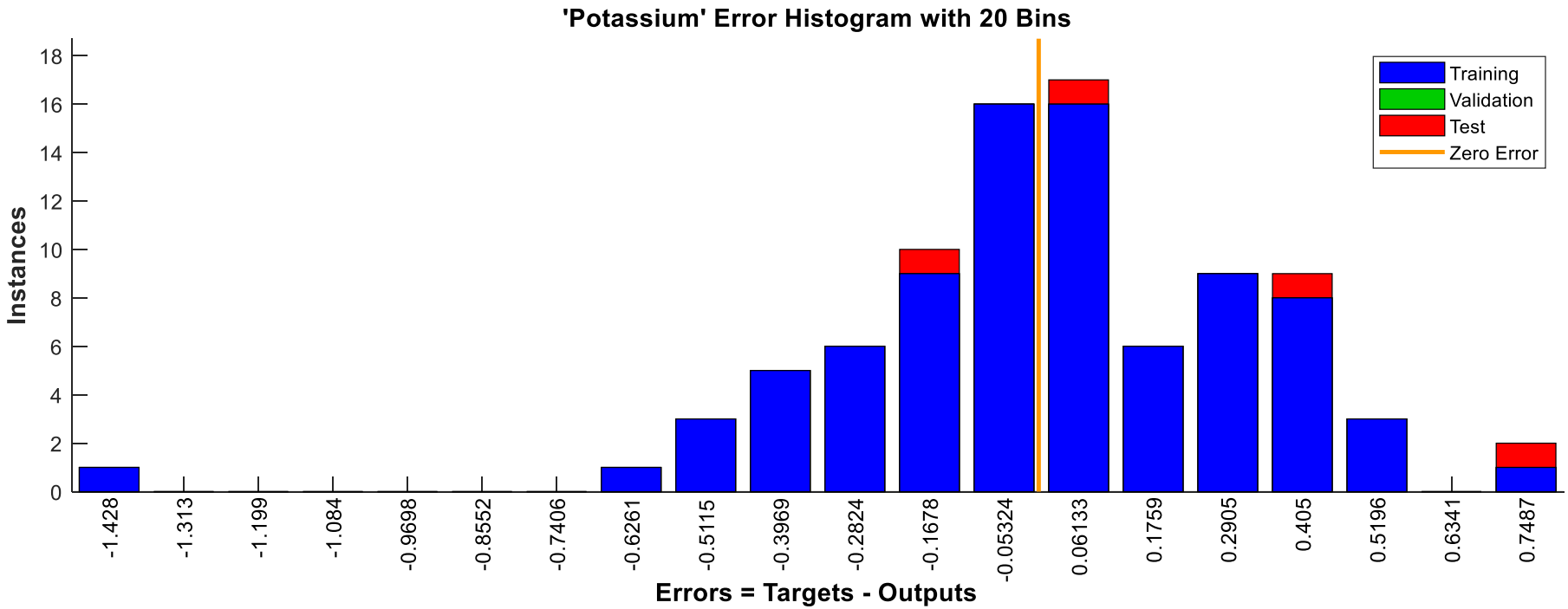

Figure 43. Potassium error histogram

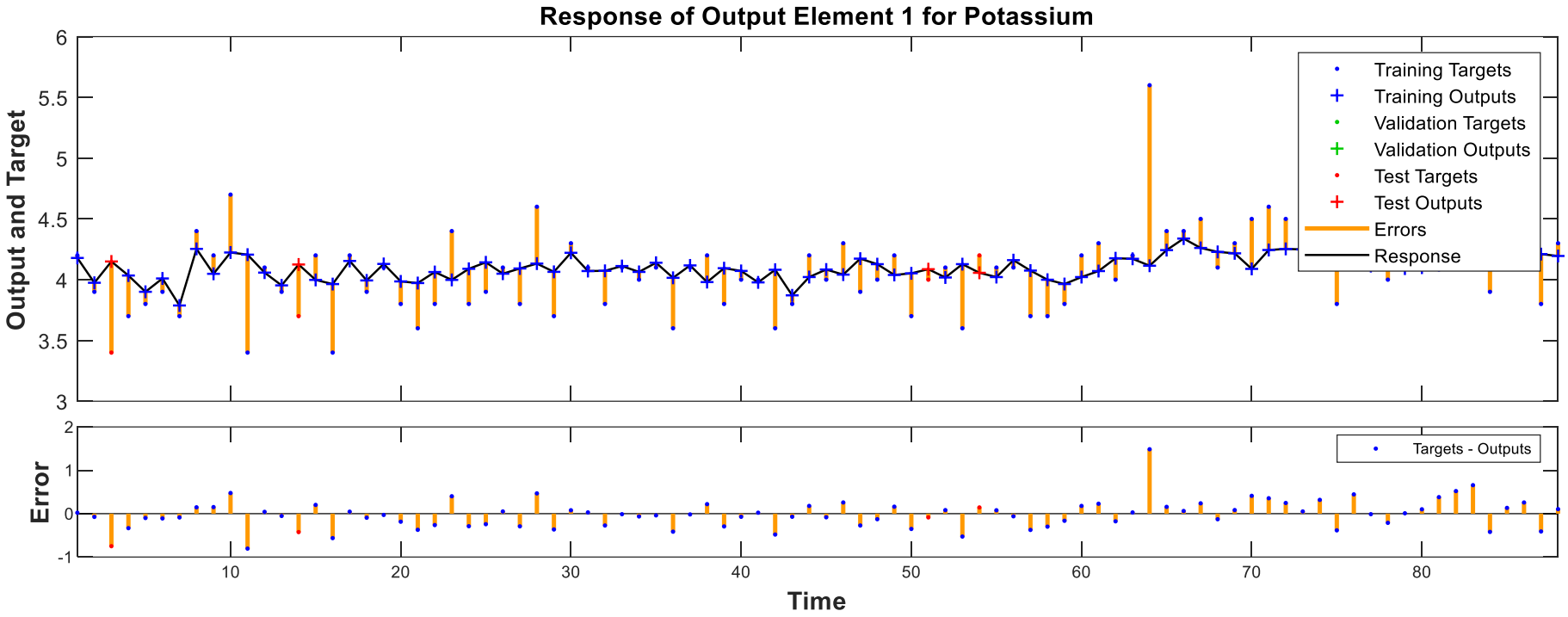

Figure 44. Potassium response and error plot

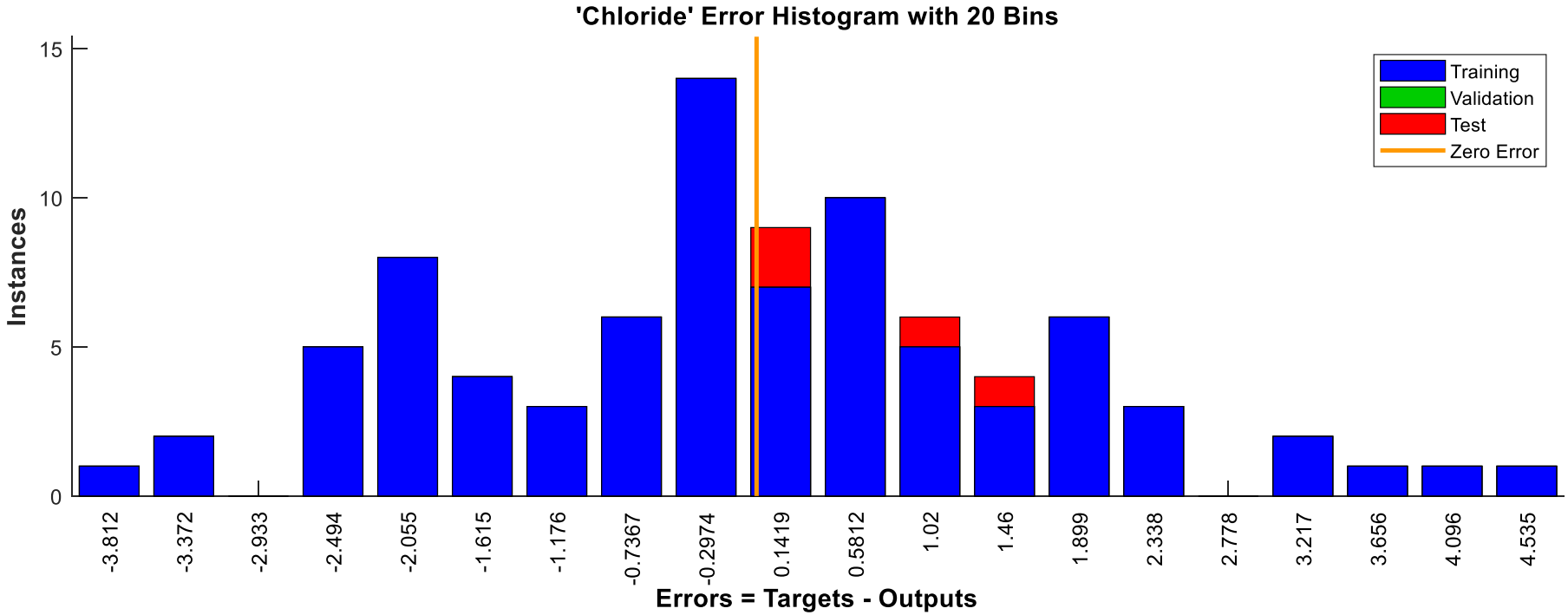

Figure 45. Chloride error histogram

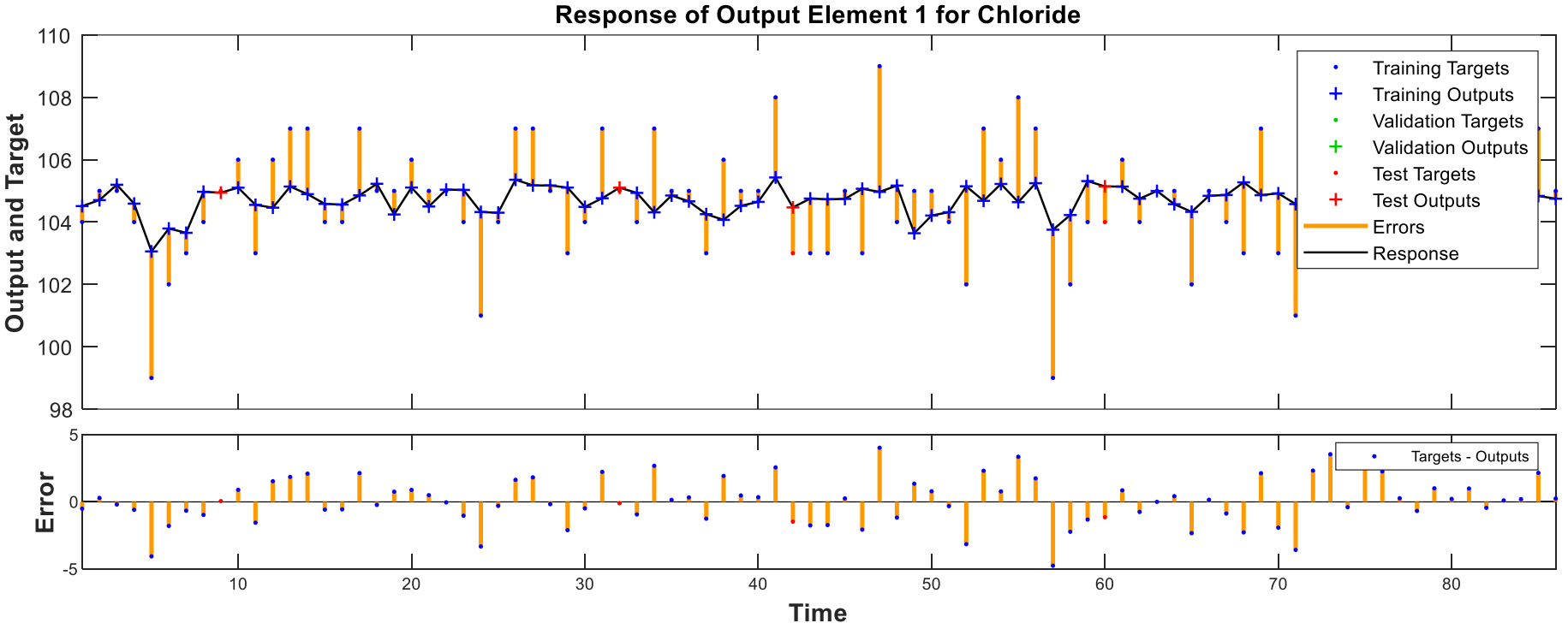

Figure 46. Chloride response and error plot

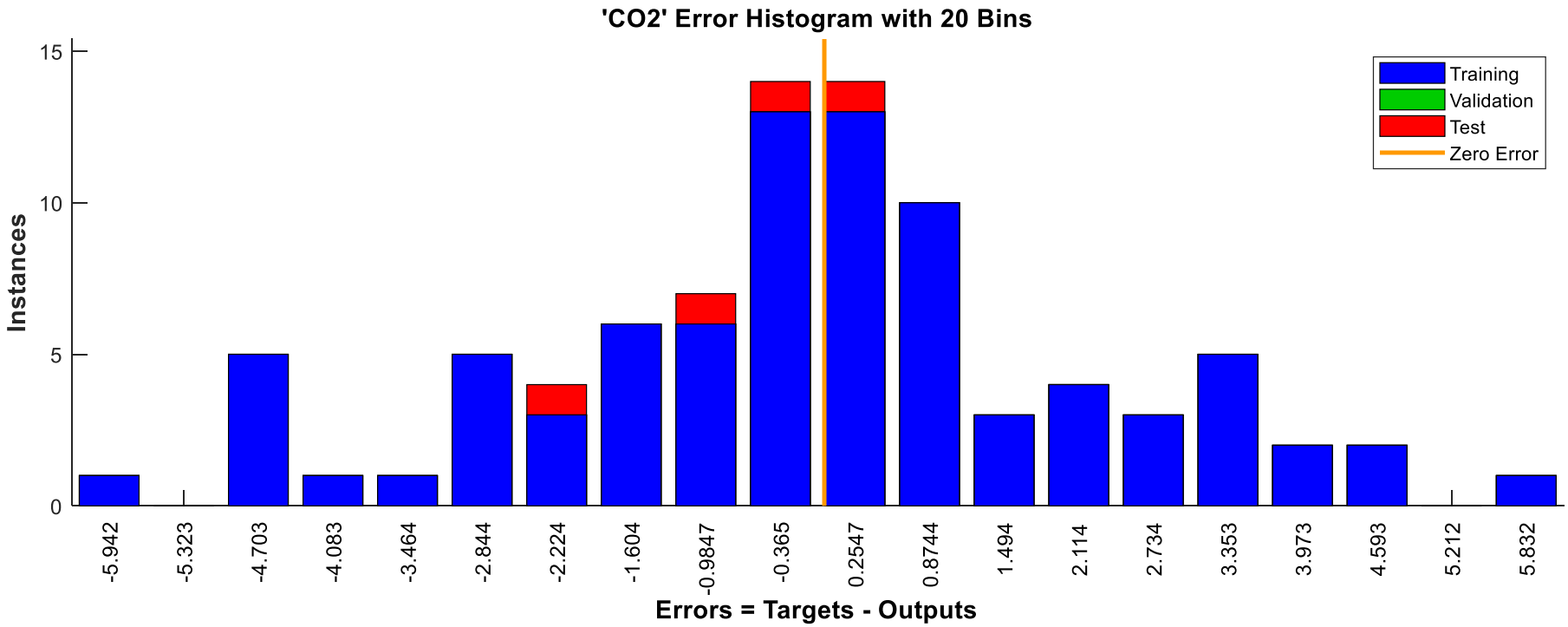

Figure 47. CO2 error histogram

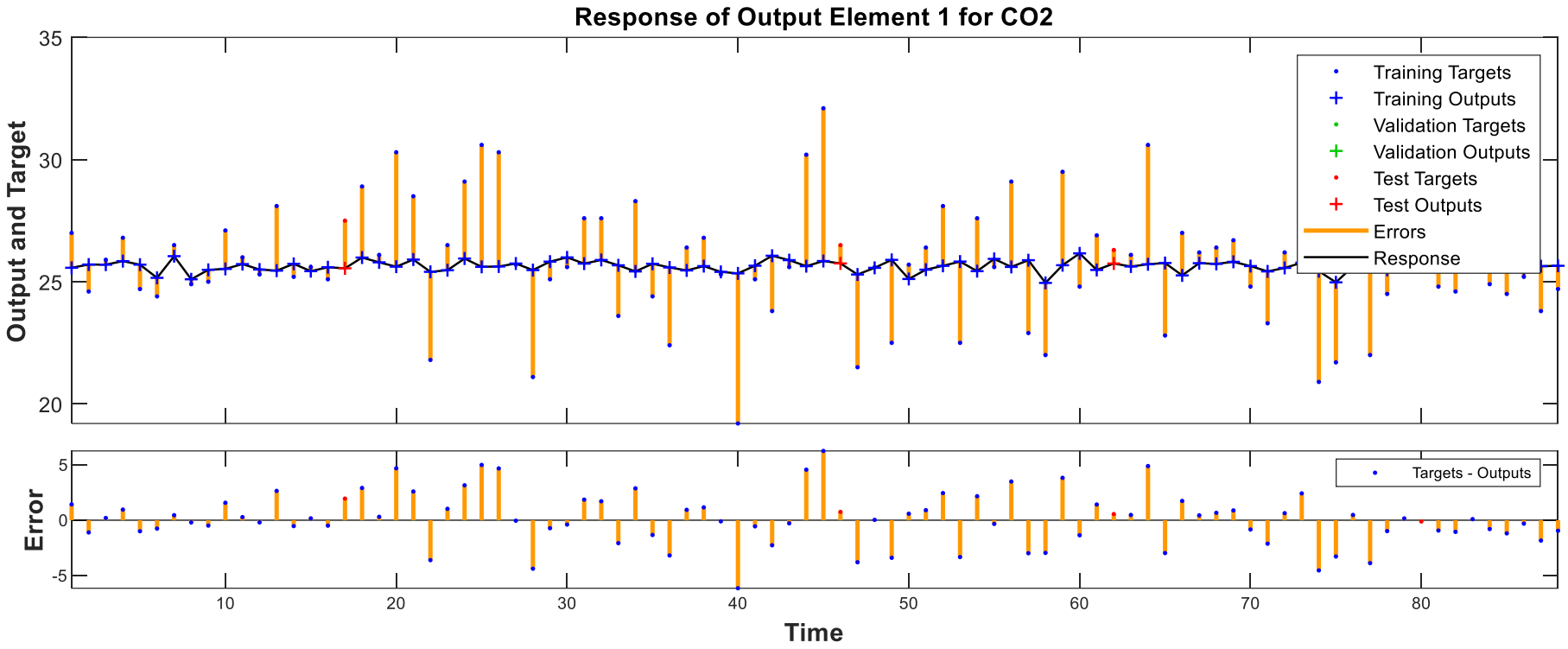

Figure 48. CO2 response and error plot

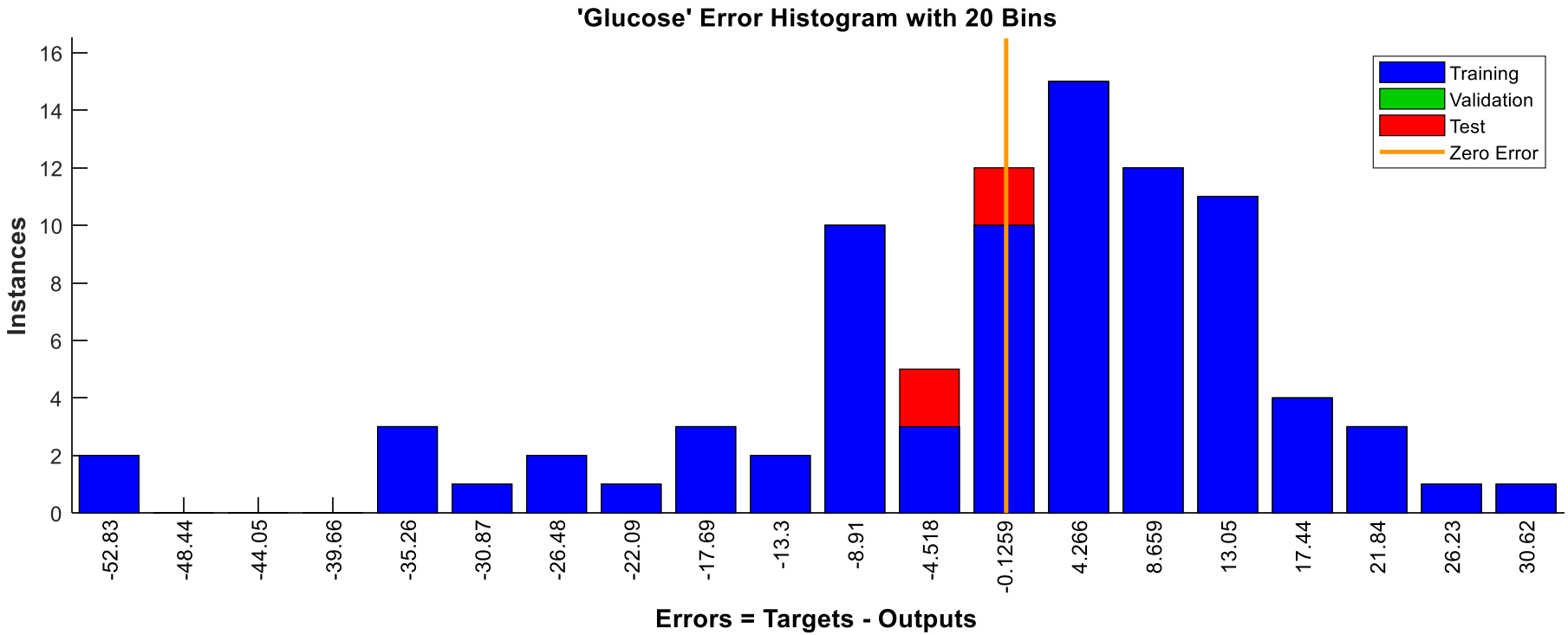

Figure 49. Glucose error histogram

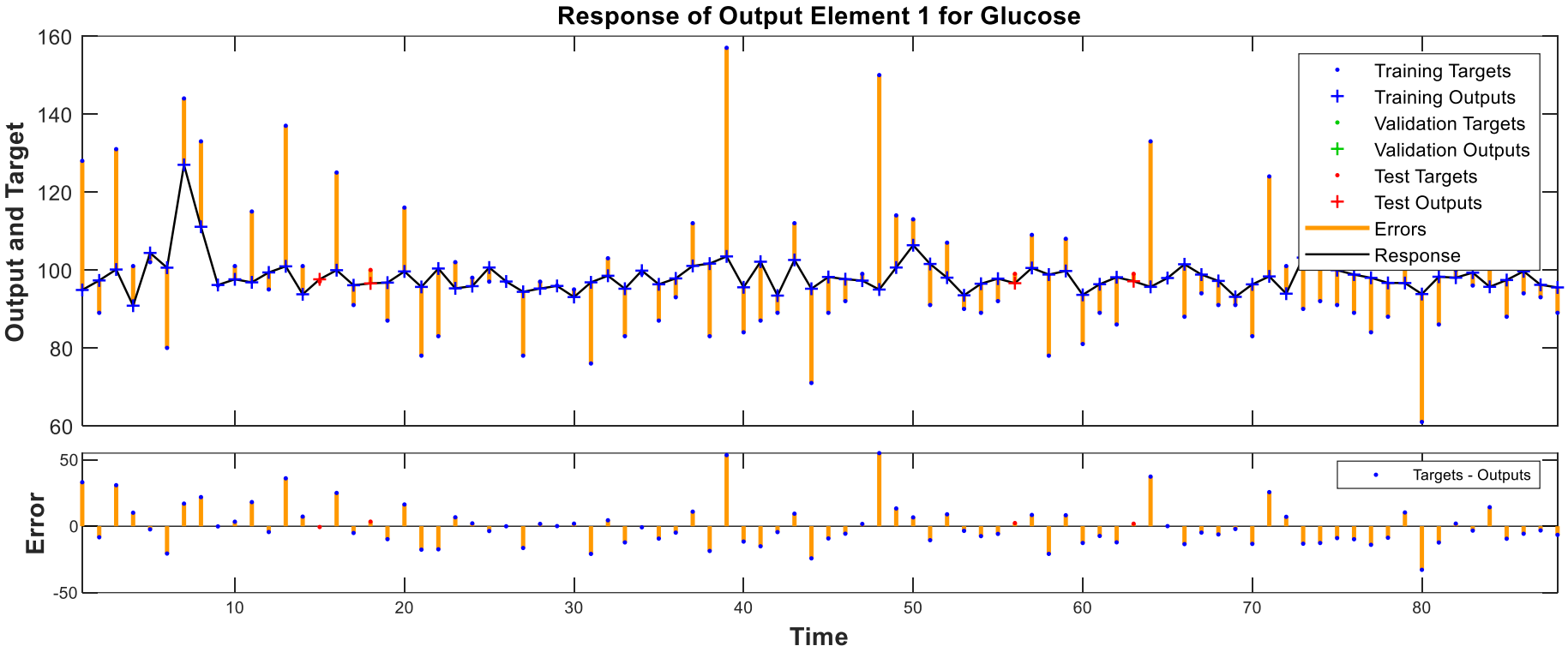

Figure 50. Glucose response and error plot

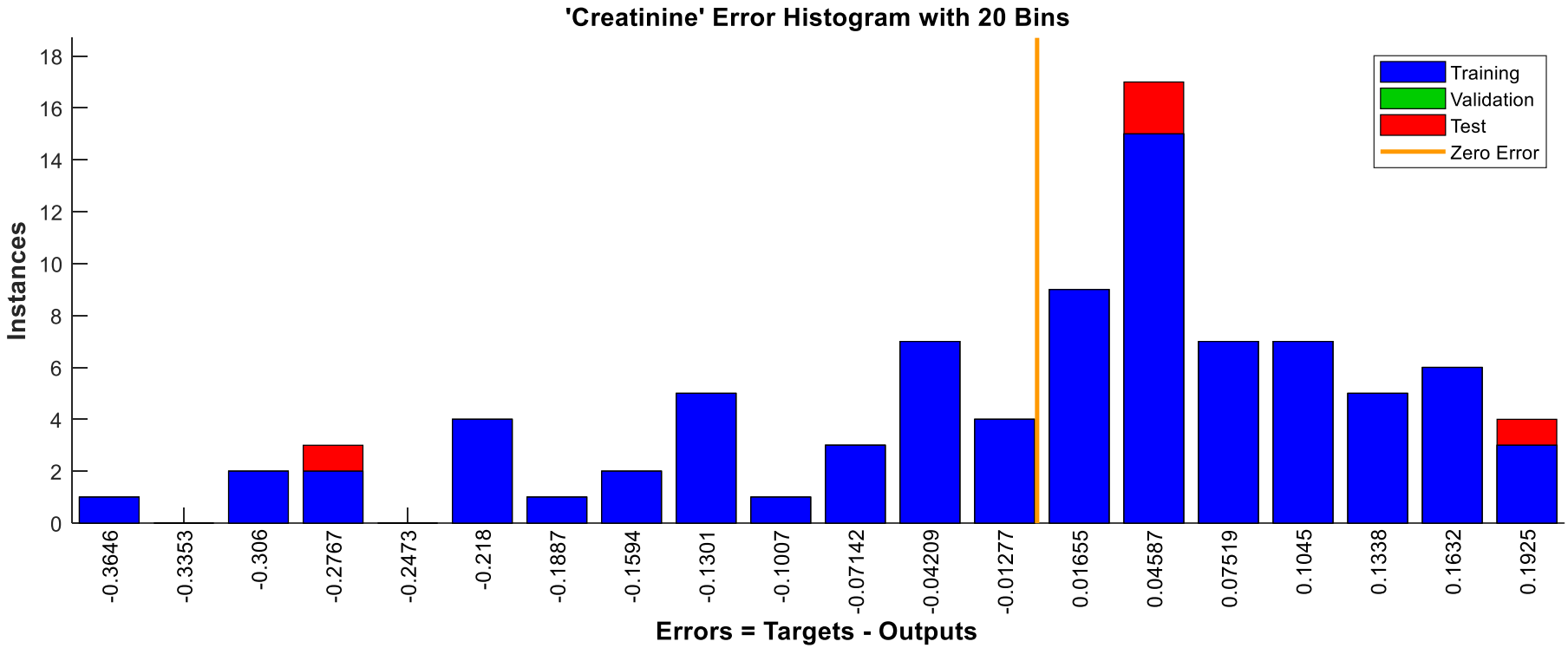

Figure 51. Creatinine error histogram

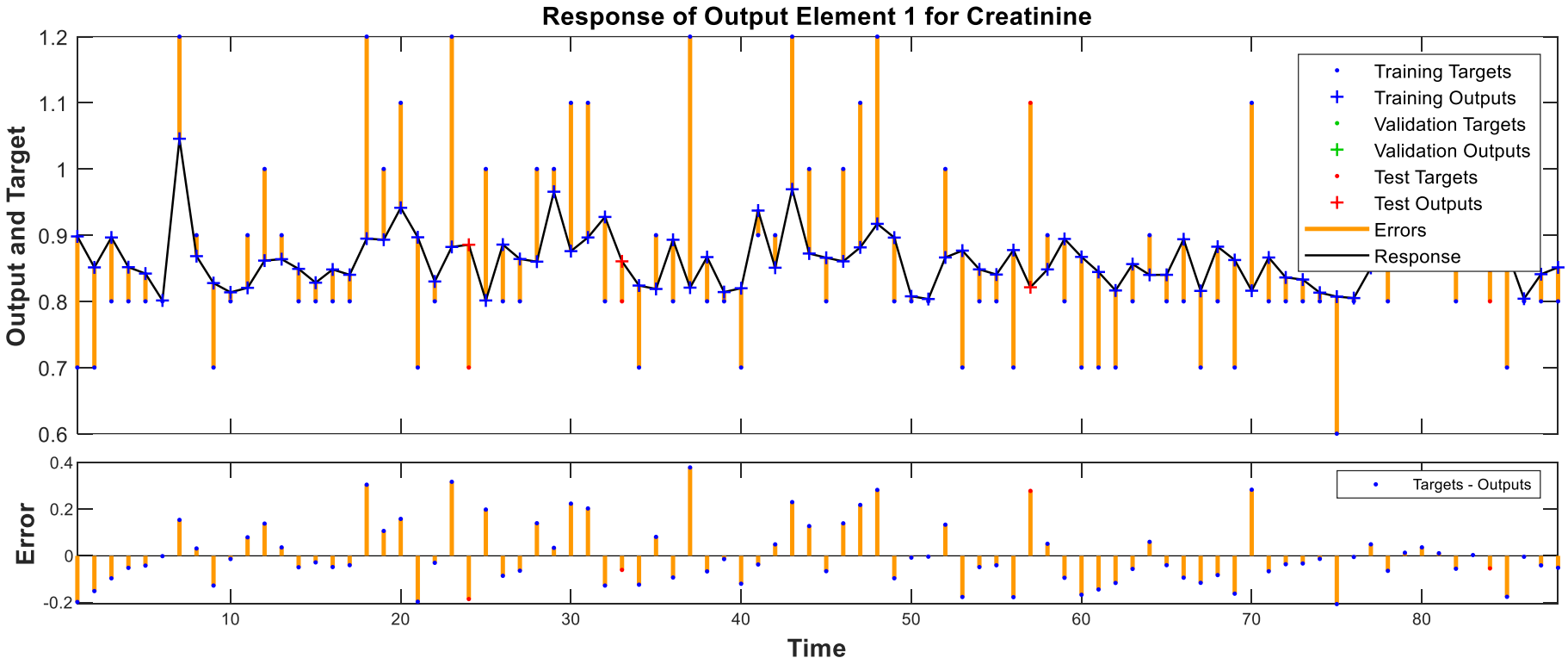

Figure 52. Creatinine response and error plot

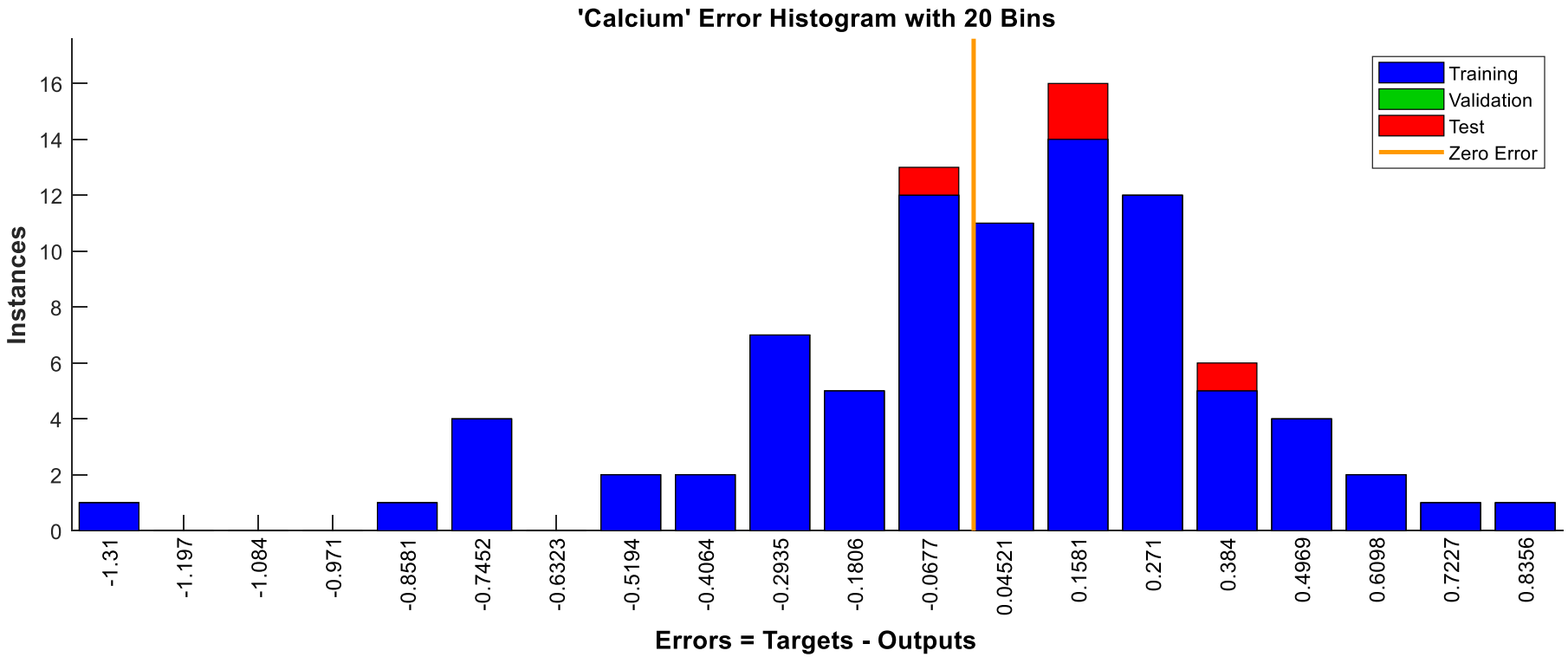

Figure 53. Calcium error histogram

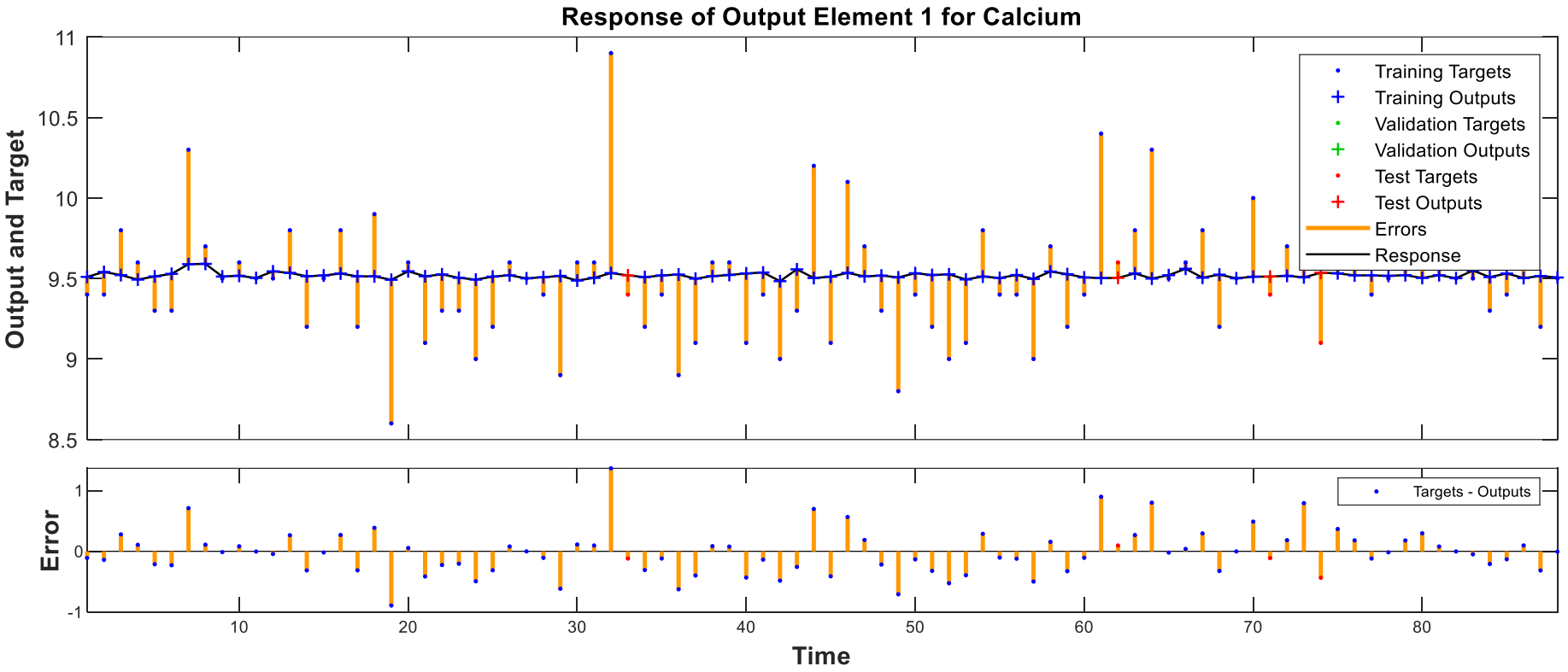

Figure 54. Calcium response and error plot

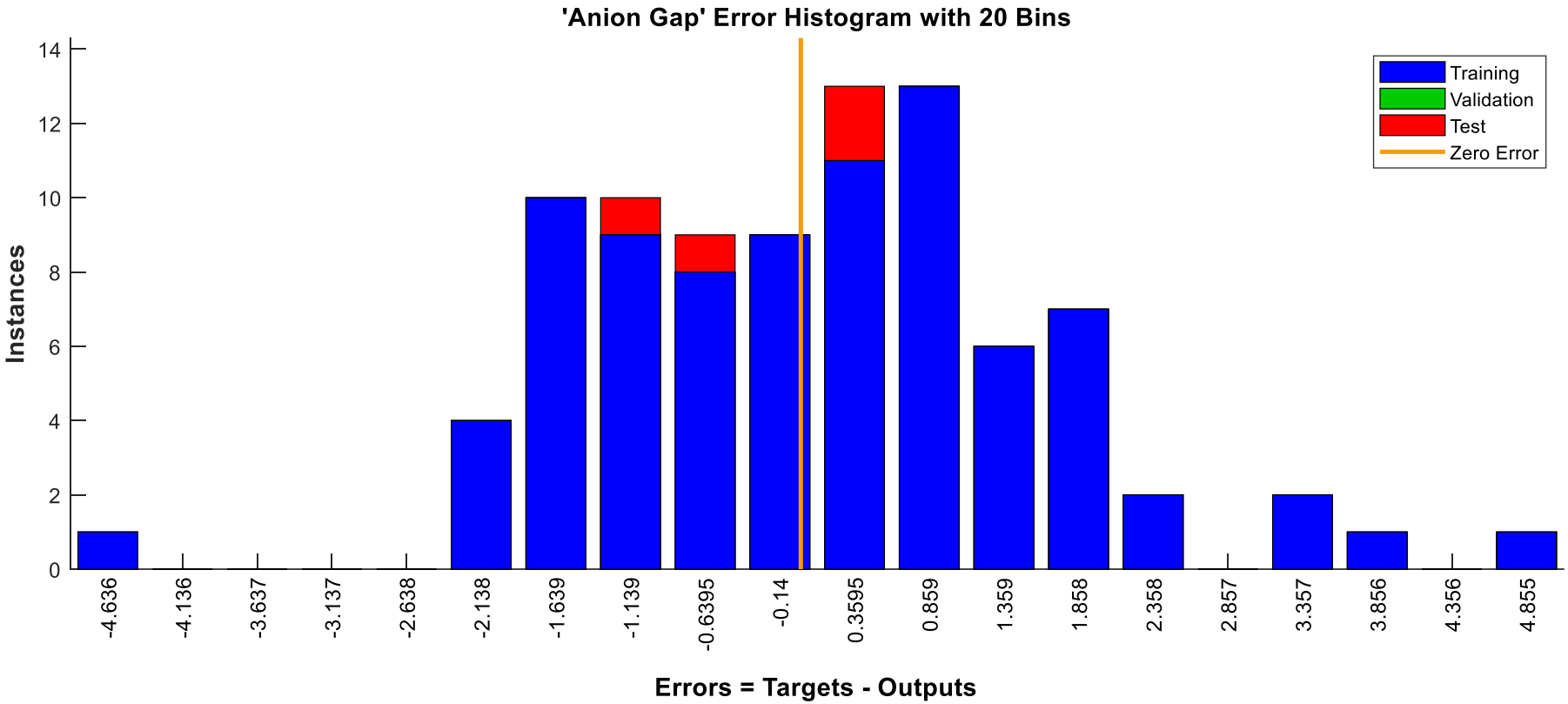

Figure 55. Anion Gap error histogram

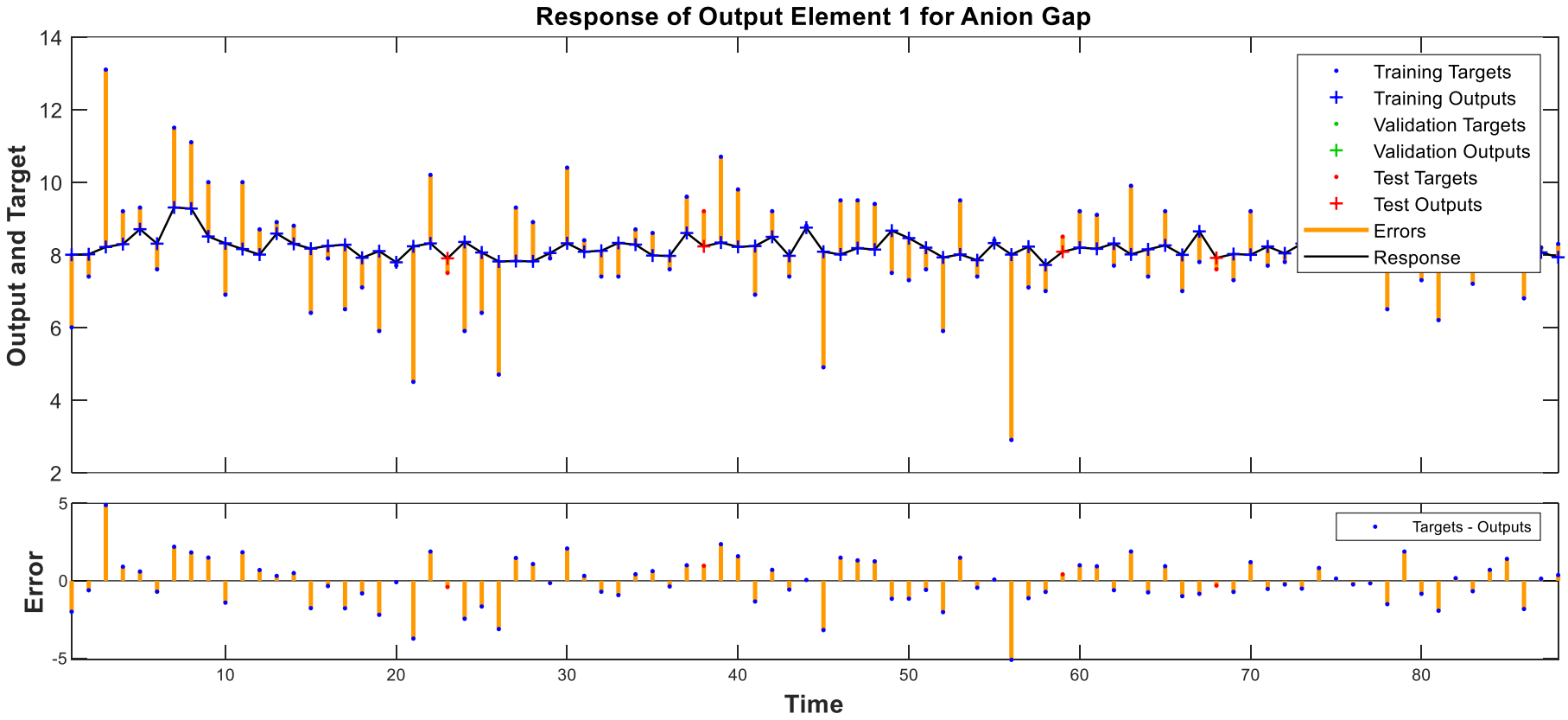

Figure 56. Anion Gap response and error plot

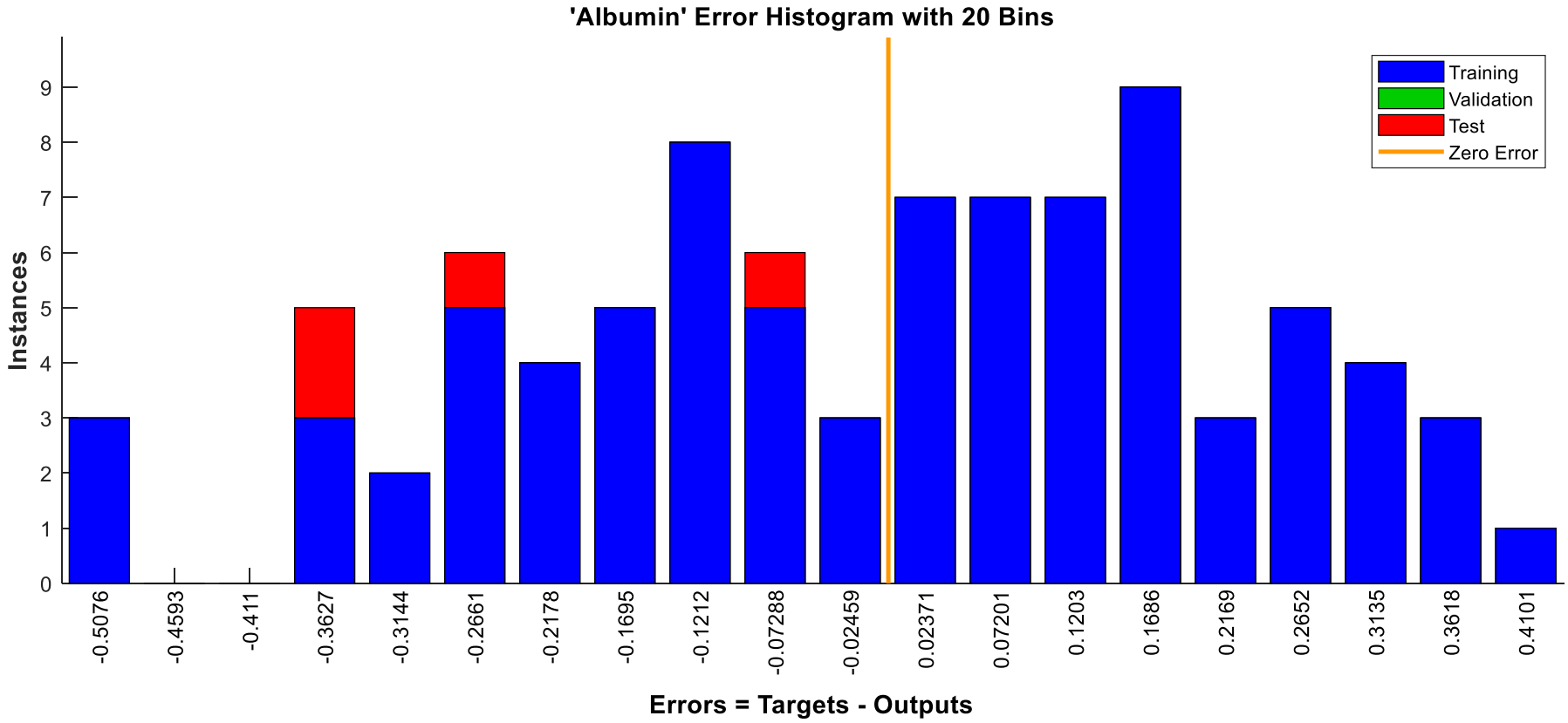

Figure 57. Albumin error histogram

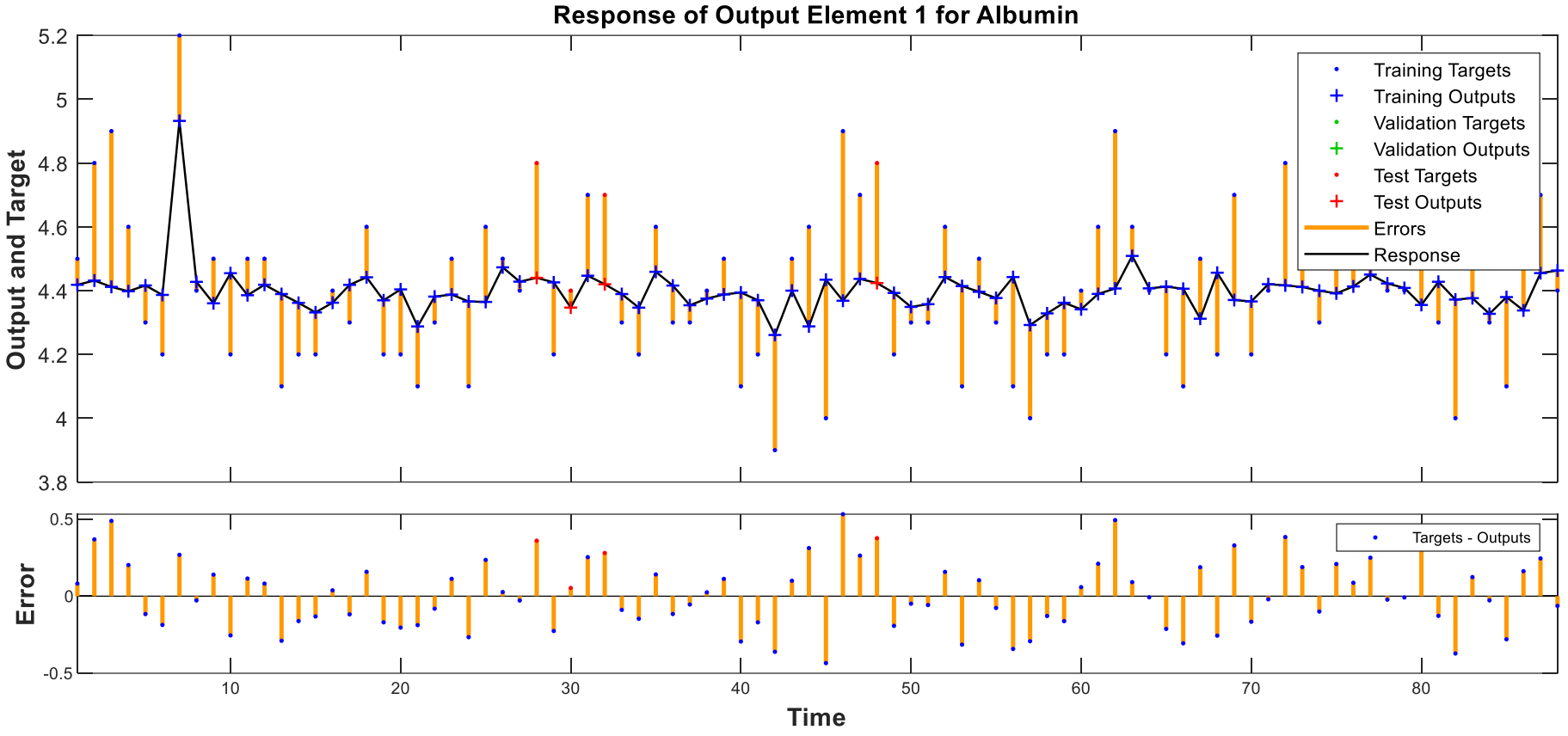

Figure 58. Albumin response and error plot

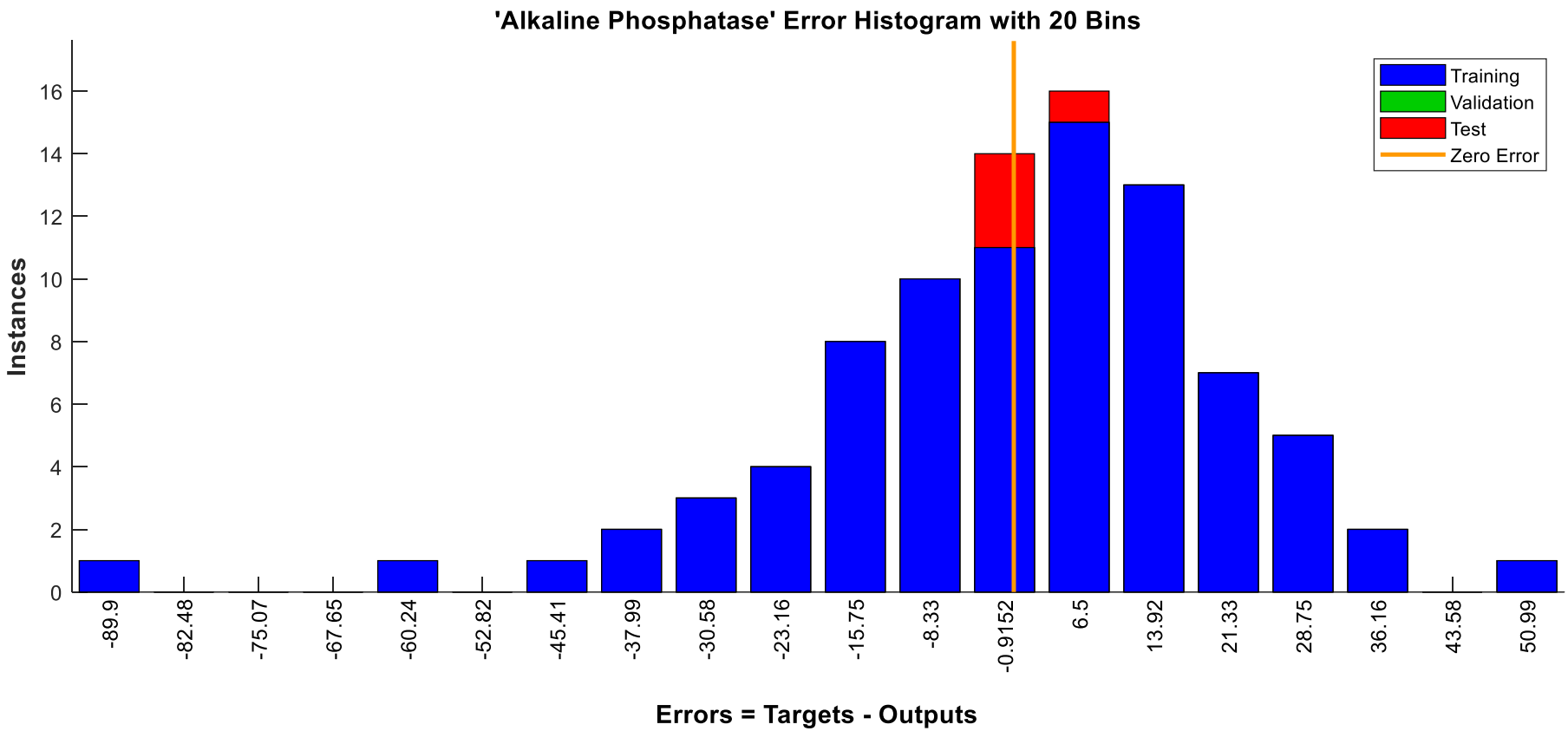

Figure 59. Alkaline Phosphatase error histogram

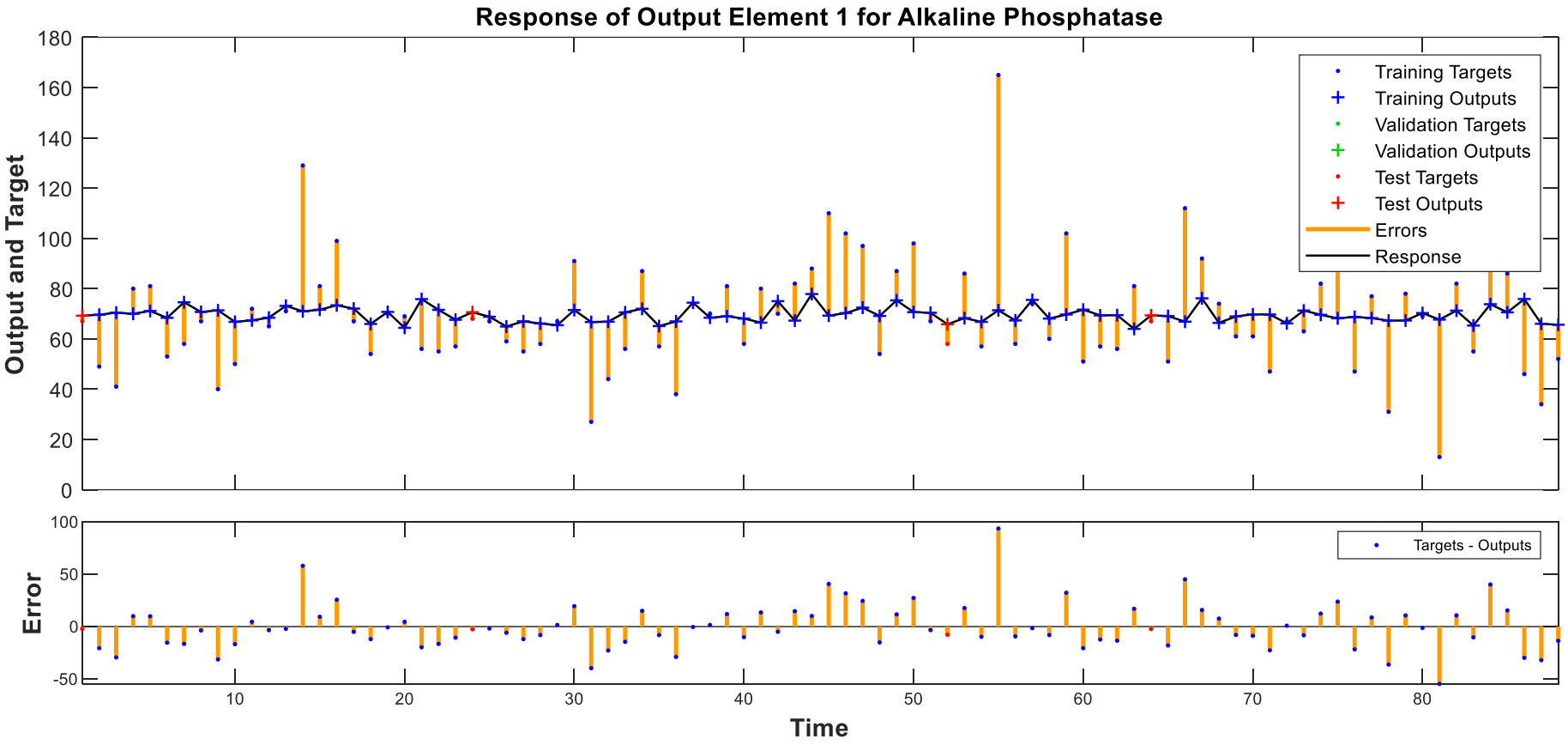

Figure 60. Alkaline Phosphatase response and error plot

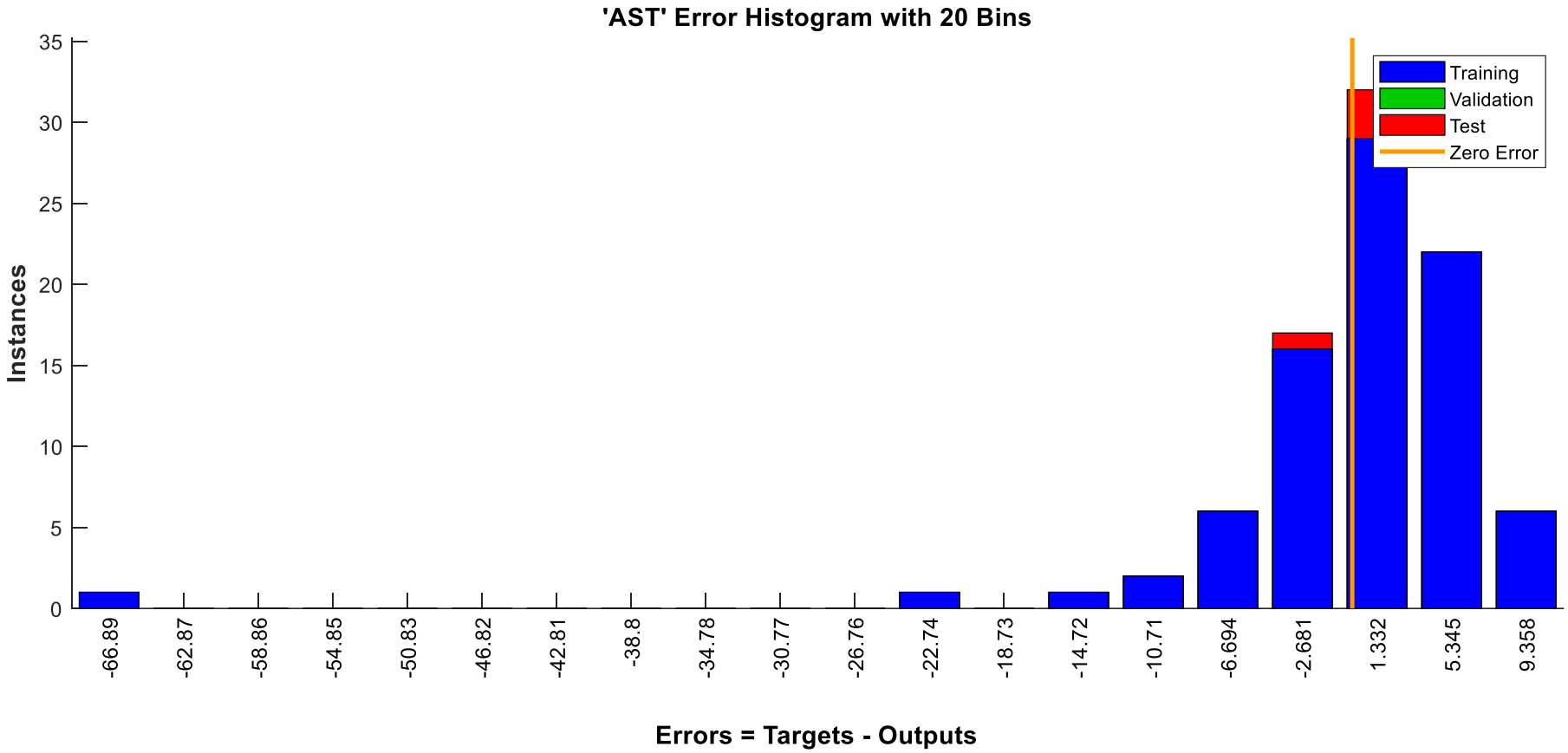

Figure 61. AST error histogram

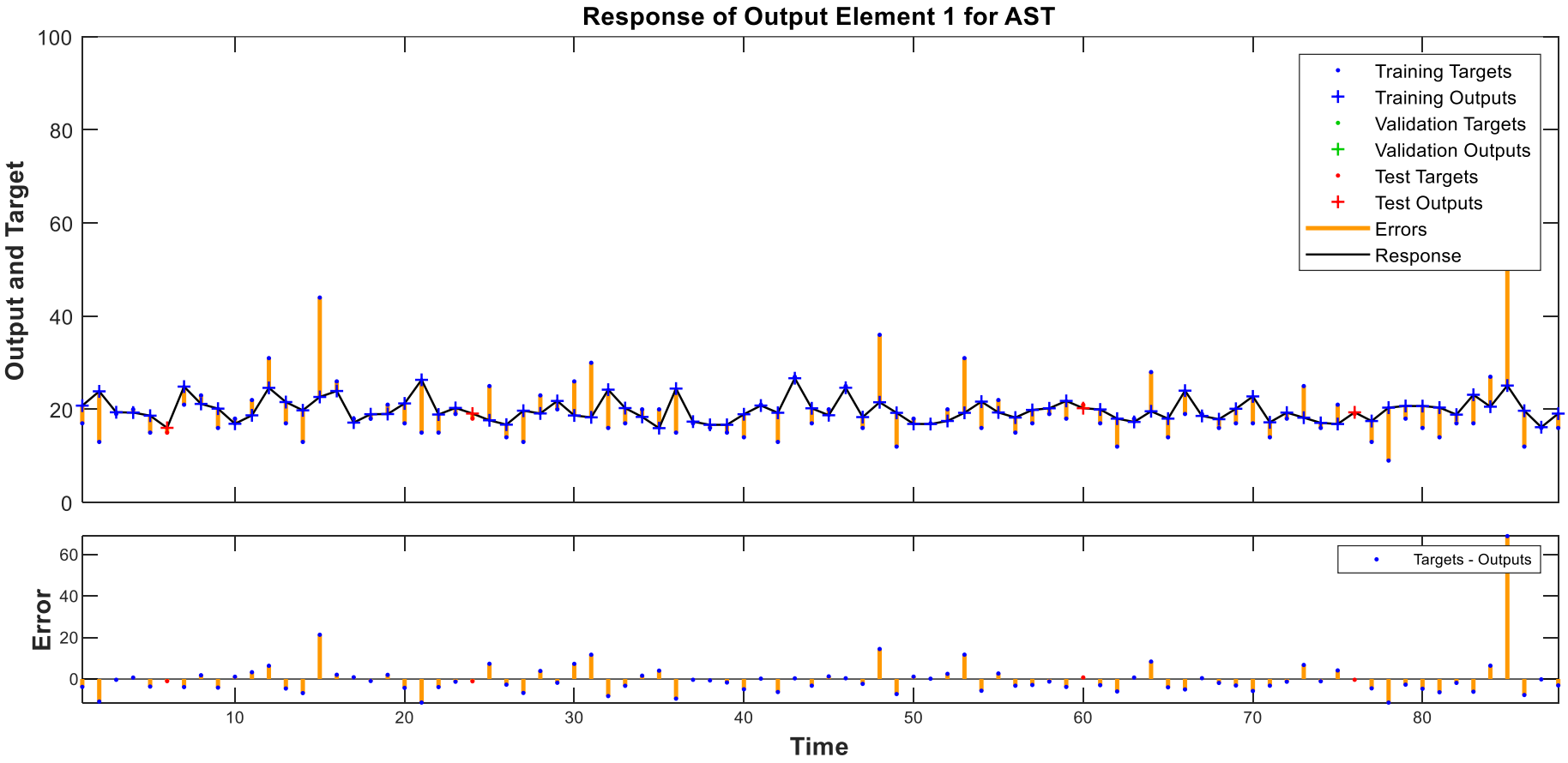

Figure 62. AST response and error plot

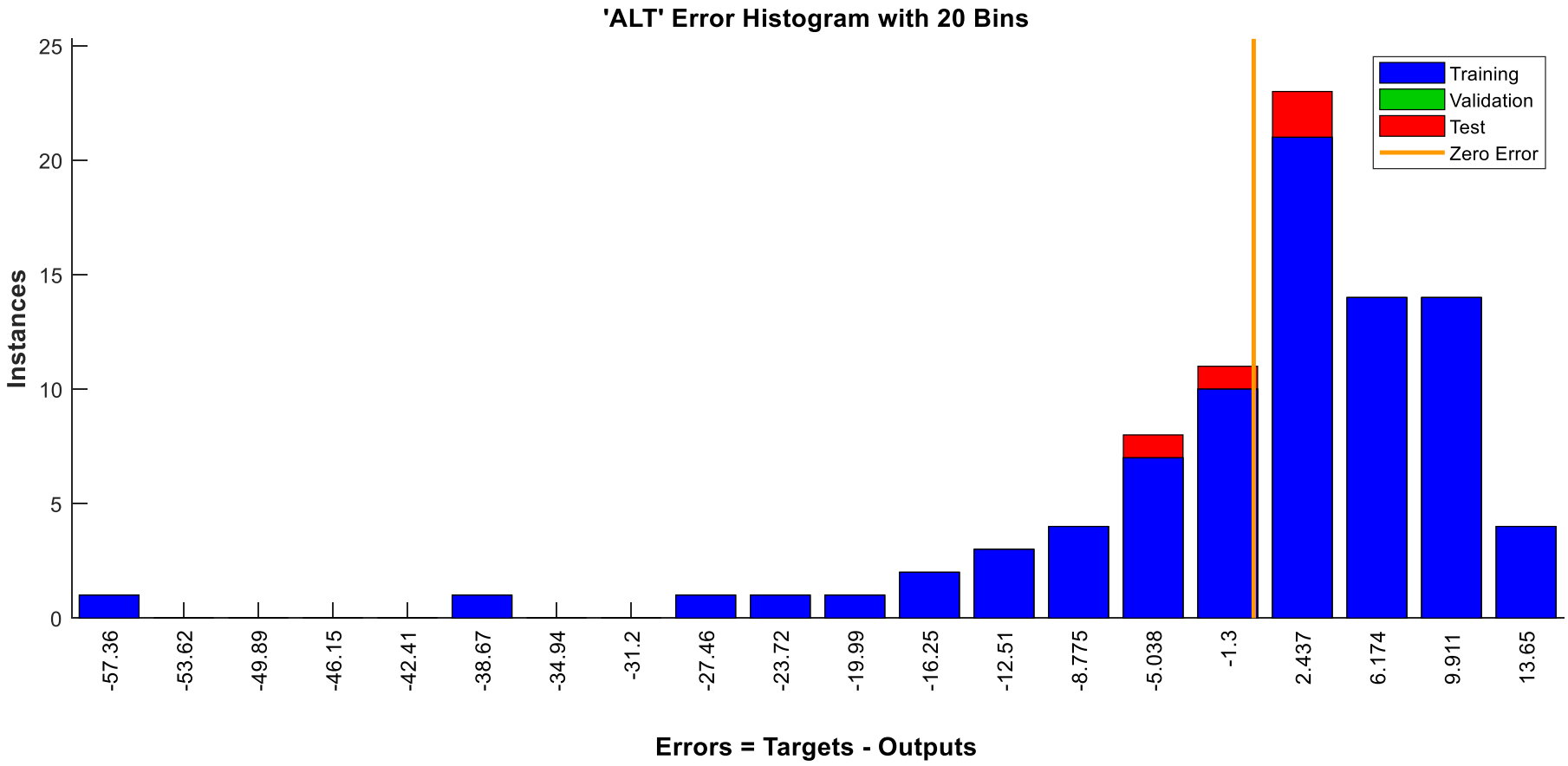

Figure 63. ALT error histogram

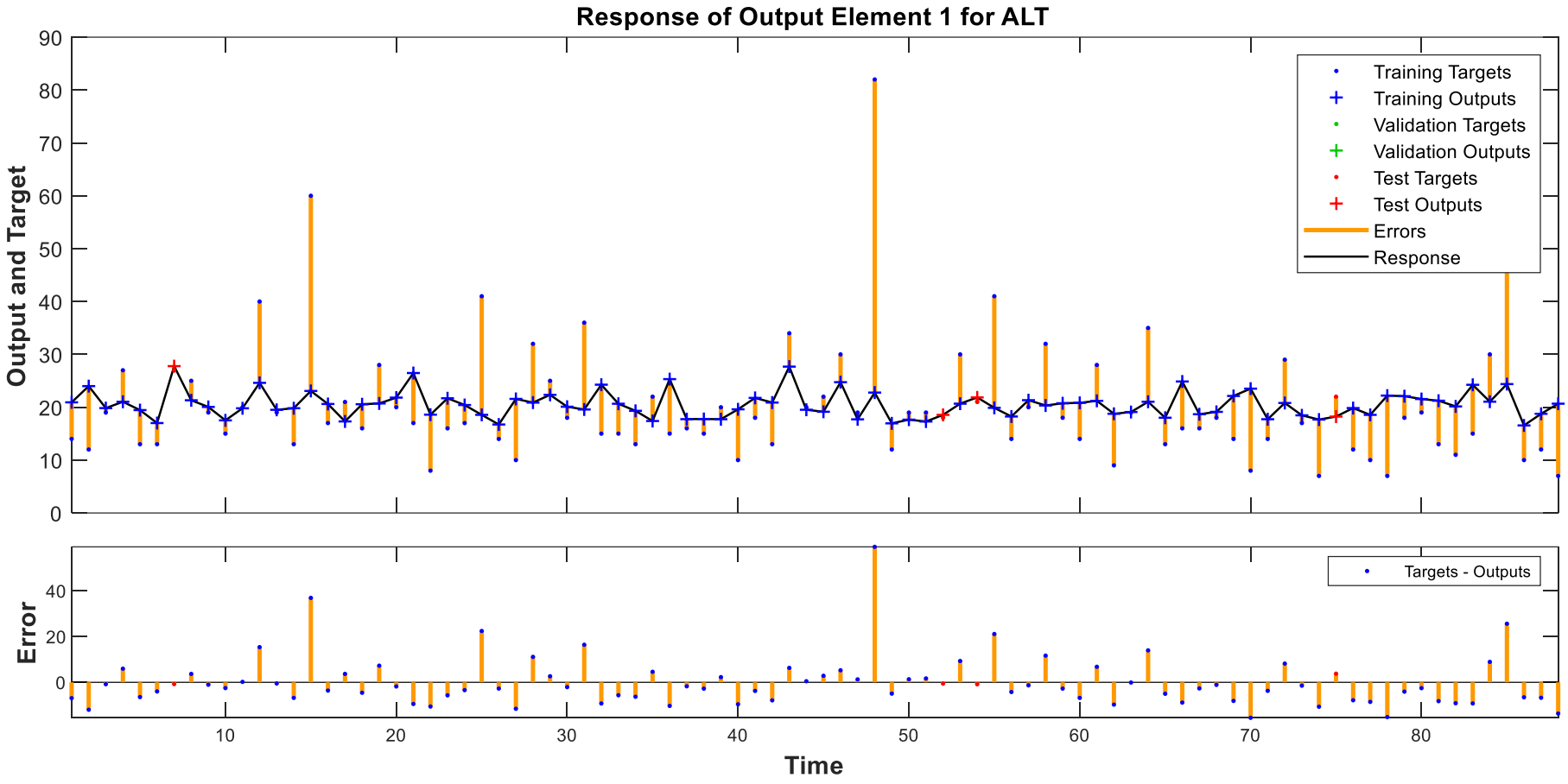

Figure 64. ALT response and error plot

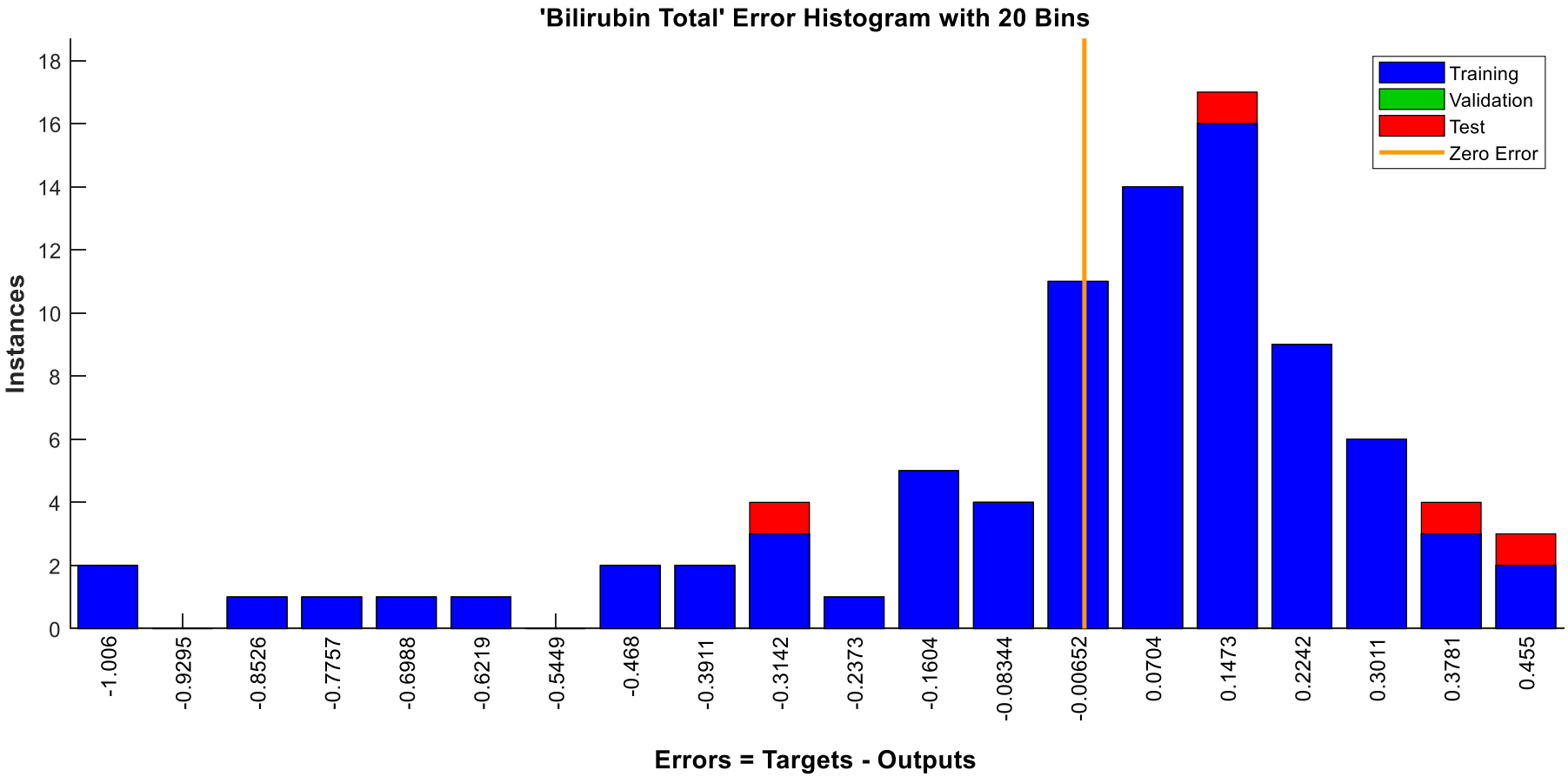

Figure 65. Bilirubin Total error histogram

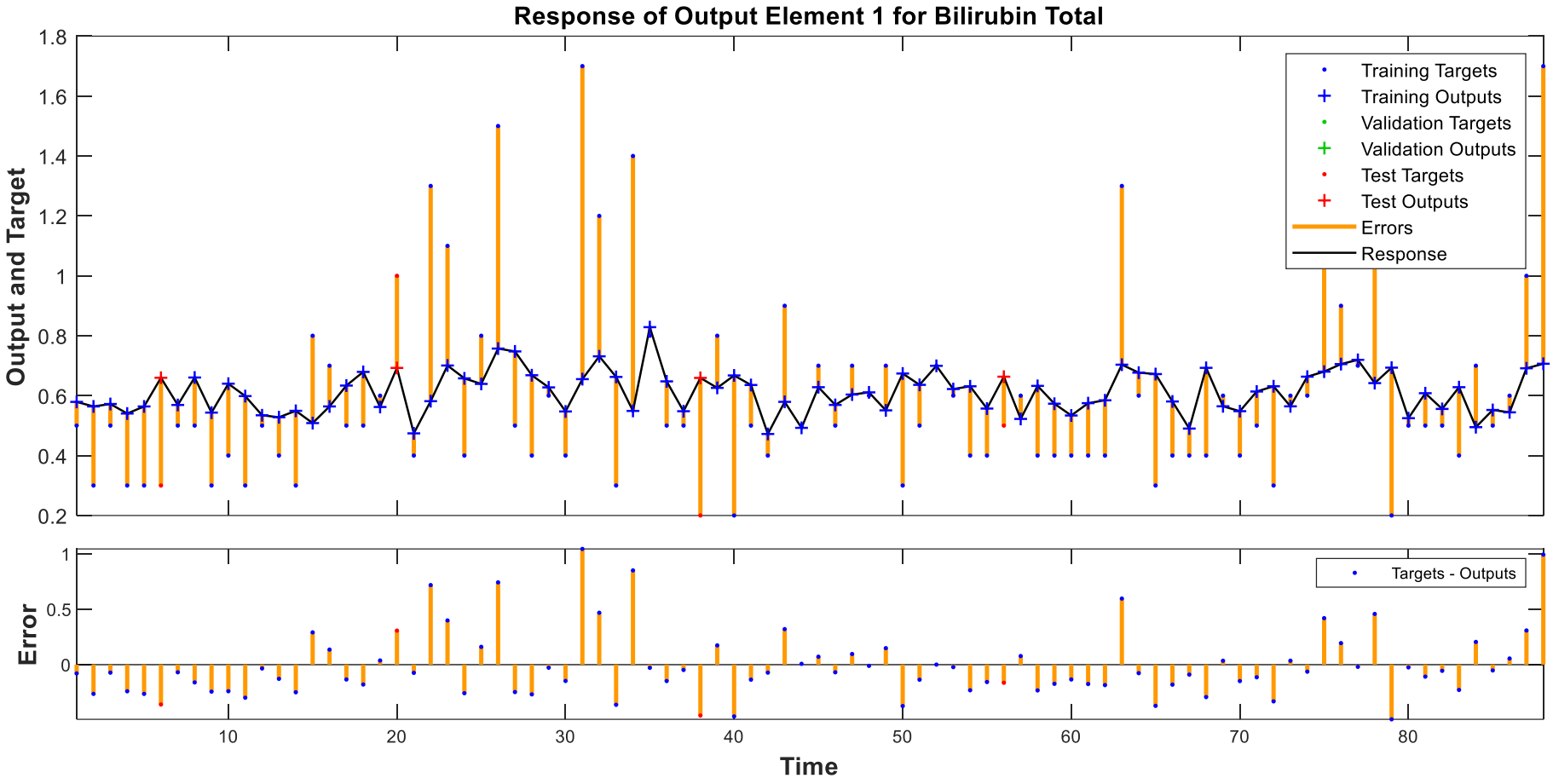

Figure 66. Bilirubin Total response and error plot

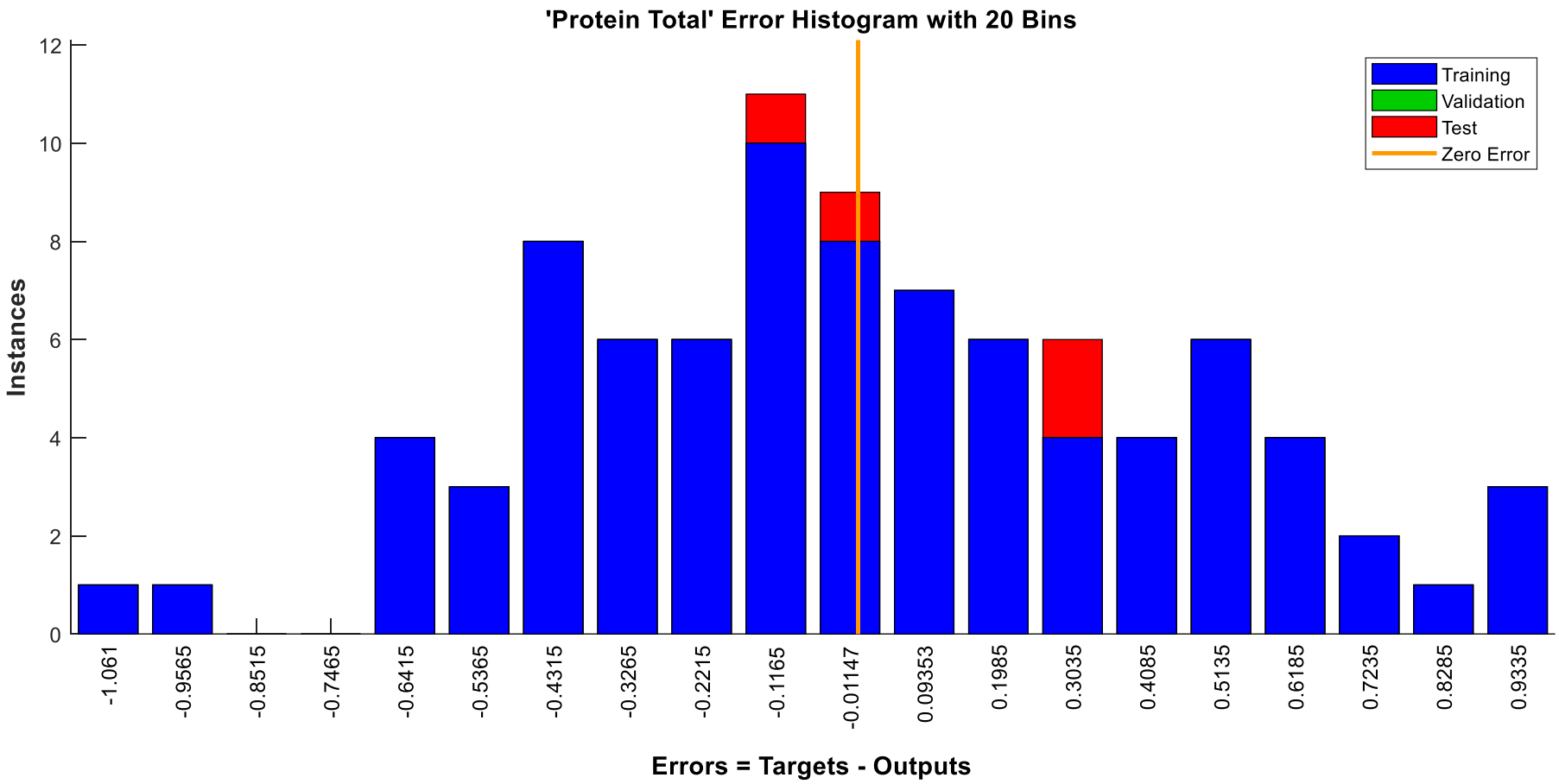

Figure 67. Protein total error histogram

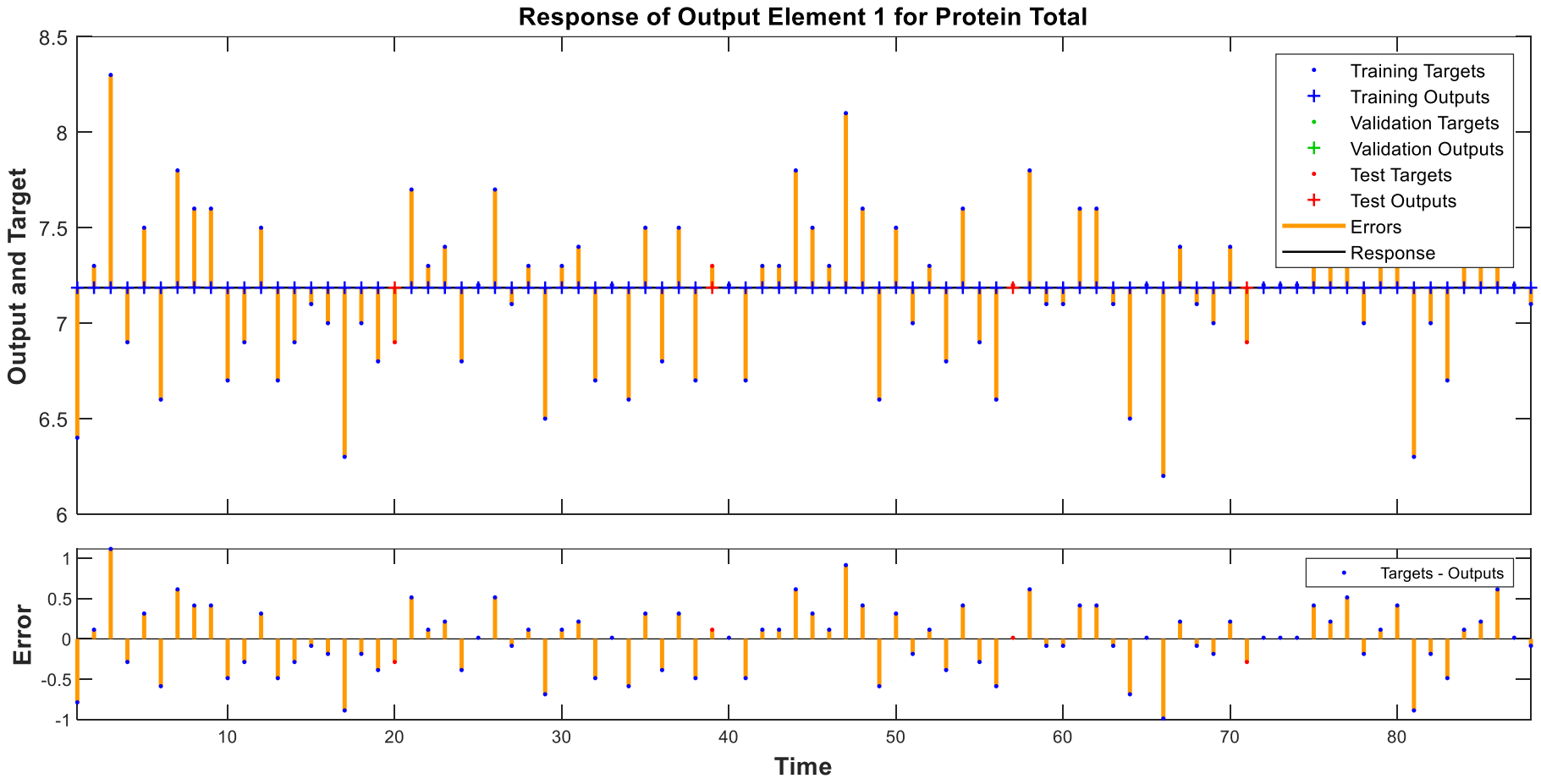

Figure 68. Protein Total response and error plot

4.2 *Binary Image Error Distribution*

Figure 39 below displays the binary image of the original grayscale spectral image in figure 8, given certain thresholds. Table 4 includes the binary image values, given the binary threshold conversion of the original grayscale spectral image.

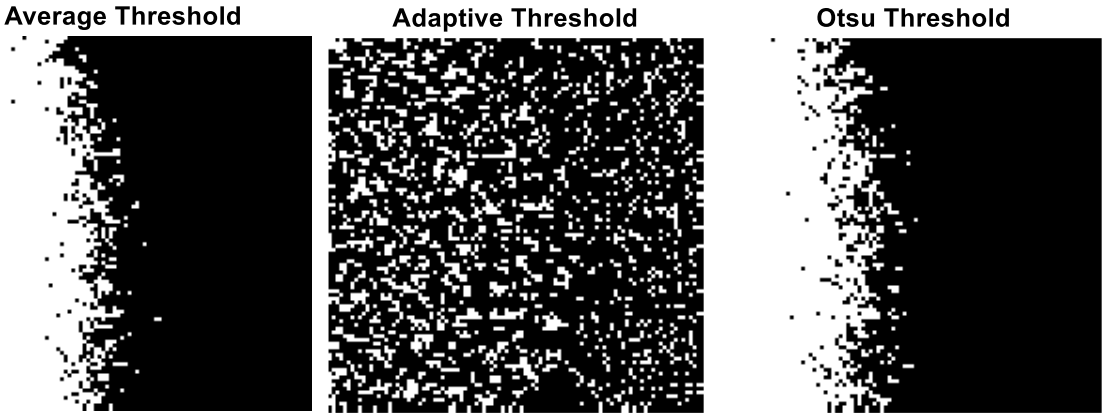

Figure 69. Certain binary images of the original grayscale spectral image as a result of the threshold conversion

TABLE XV
BINARY IMAGE VALUES

Average	Adaptive	Otsu
4169	2143	3544

Table 15 Binary image values of the original grayscale spectral image given the thresholds

Tables 5, 7, and 9 display the regression model types and corresponding errors resulting from the binary conversion and input variable transformation analysis. Tables 6, 8, and 10 display the binary image regression model errors resulting from the binary conversion and variable transform along with the error distribution, relative to the CMP parameter mean standard deviation.

TABLE XVI

AVERAGE THRESHOLD REGRESSION MODEL TYPE AND ROOT MEAN SQUARED ERROR

CMP	Average	RMSE	Reciprocal	RMSE	Logarithm	RMSE	Cube Root	RMSE	Square Root	RMSE	Square	RMSE
BUN	SVM	3.78100	LR	3.88300	SVM	3.91970	LR	3.84950	SVM	3.77870	SVM	3.88600
Sodium	LR	1.75440	SVM	1.74630	LR	1.79850	LR	1.76410	LR	1.75690	SVM	1.75280
Potassium	Tree	0.34508	SVM	0.35314	LR	0.34202	LR	0.34994	GPR	0.34592	LR	0.35223
Chloride	SVM	1.92050	SVM	1.88360	LR	1.87690	SVM	1.88610	LR	1.89830	SVM	1.88940
CO2	Tree	2.37430	Tree	2.35910	Tree	2.38980	SVM	2.37210	SVM	2.37560	SVM	2.37920
Glucose	GPR	17.0010	GPR	16.52200	GPR	17.04900	Tree	16.97300	GPR	16.78700	GPR	17.07500
Creatinine	LR	0.14983	GPR	0.15057	GPR	0.15209	LR	0.15112	LR	0.15133	Tree	0.14837
Calcium	GPR	0.37899	Tree	0.37536	GPR	0.37853	LR	0.37596	SVM	0.37555	GPR	0.37564
Anion Gap	LR	1.59040	Tree	1.59340	LR	1.59270	SVM	1.57570	SVM	1.56880	Tree	1.56460
Albumin	GPR	0.25922	SVM	0.25542	Tree	0.26128	Tree	0.25845	LR	0.25954	LR	0.26315
Alkaline Phosphatase	LR	23.13300	LR	22.75000	Tree	22.62600	SVM	22.62300	LR	22.66300	LR	23.03700
AST	SVM	9.66090	LR	9.76510	SVM	9.64580	LR	9.67490	LR	9.77120	LR	9.72550
ALT	LR	11.82700	SVM	11.84800	LR	12.02300	LR	11.84200	LR	11.77700	SVM	11.83800
Bilirubin Total	LR	0.32557	LR	0.32023	GPR	0.32110	Ensemble	0.31331	Ensemble	0.31807	GPR	0.31987
Protein Total	LR	0.41947	LR	0.42239	SVM	0.42250	SVM	0.41992	SVM	0.41571	SVM	0.42166

Table 16. Average binary input transform regression model error (n=90)

TABLE XVII

AVERAGE THRESHOLD ROOT MEAN SQUARED ERROR AND STANDARD DEVIATION COMPARISON

CMP	Average	Reciprocal	Logarithm	Cube Root	Square Root	Square	1 SD (%)	2 SD (%)	3 SD (%)
BUN	3.78100	3.88300	3.91970	3.84950	3.77870	3.88600	33	100	100
Sodium	1.75440	1.74630	1.79850	1.76410	1.75690	1.75280	100	100	100
Potassium	0.34508	0.35314	0.34202	0.34994	0.34592	0.35223	100	100	100
Chloride	1.92050	1.88360	1.87690	1.88610	1.89830	1.88940	83	100	100
CO2	2.37430	2.35910	2.38980	2.37210	2.37560	2.37920	100	100	100
Glucose	17.00100	16.52200	17.04900	16.97300	16.78700	17.07500	50	100	100
Creatinine	0.14983	0.15057	0.15209	0.15112	0.15133	0.14837	100	100	100
Calcium	0.37899	0.37536	0.37853	0.37596	0.37555	0.37564	100	100	100
Anion Gap	1.59040	1.59340	1.59270	1.57570	1.56880	1.56460	100	100	100
Albumin	0.25922	0.25542	0.26128	0.25845	0.25954	0.26315	100	100	100
Alkaline Phosphatase	23.13300	22.75000	22.62600	22.62300	22.66300	23.03700	67	100	100
AST	9.66090	9.76510	9.64580	9.67490	9.77120	9.72550	50	100	100
ALT	11.82700	11.84800	12.02300	11.84200	11.77700	11.83800	17	100	100
Bilirubin Total	0.32557	0.32023	0.32110	0.31331	0.31807	0.31987	0	100	100
Protein Total	0.41947	0.42239	0.42250	0.41992	0.41571	0.42166	0	100	100
Standard Deviation Total							67	100	100

Table 17. Average binary input transform error and standard deviation distribution (n=90)

TABLE XVIII

ADAPTIVE THRESHOLD REGRESSION MODEL TYPE AND ROOT MEAN SQUARED ERROR

CMP	Adaptive	RMSE	Reciprocal	RMSE	Logarithm	RMSE	Cube Root	RMSE	Square Root	RMSE	Square	RMSE
BUN	Tree	3.87600	SVM	3.81640	SVM	3.81200	SVM	3.89260	SVM	3.85350	SVM	3.83470
Sodium	Tree	1.68440	Ensemble	1.70170	SVM	1.73080	LR	1.69180	Tree	1.69950	LR	1.69290
Potassium	LR	0.35428	Tree	0.35192	LR	0.35640	LR	0.35407	SVM	0.35519	LR	0.35063
Chloride	SVM	1.87390	SVM	1.87390	SVM	1.88650	SVM	1.87240	LR	1.87750	SVM	1.87330
CO2	SVM	2.36950	SVM	2.35970	SVM	2.33080	SVM	2.35590	SVM	2.36650	SVM	2.34840
Glucose	LR	17.15100	LR	17.28800	LR	17.42600	LR	16.95600	LR	17.48600	LR	17.04200
Creatinine	LR	0.15066	LR	0.15288	GPR	0.15198	LR	0.15080	Ensemble	0.14731	LR	0.15144
Calcium	LR	0.38162	LR	0.37754	LR	0.37489	LR	0.37583	LR	0.37517	SVM	0.36892
Anion Gap	GPR	1.55210	GPR	1.54110	Tree	1.52900	GPR	1.55080	Tree	1.65140	GPR	1.53420
Albumin	Tree	0.25991	LR	0.25779	SVM	0.25774	SVM	0.25949	GPR	0.26071	LR	0.26115
Alkaline Phosphatase	LR	22.74900	LR	22.71500	SVM	23.14800	LR	22.84200	GPR	23.03900	SVM	22.63000
AST	SVM	9.75170	LR	9.68430	LR	9.79200	LR	9.73460	LR	9.74890	Tree	9.75550
ALT	Tree	11.81000	LR	11.87100	Tree	11.78500	LR	11.88900	GPR	11.86500	GPR	11.97600
Bilirubin Total	LR	0.32360	LR	0.32175	LR	0.32122	LR	0.32470	LR	0.31925	GPR	0.32078
Protein Total	SVM	0.41976	LR	0.42361	LR	0.42005	LR	0.42747	LR	0.42064	LR	0.42293

Table 18. Adaptive binary input transform regression model error (n=90)

TABLE XIX

ADAPTIVE THRESHOLD ROOT MEAN SQUARED ERROR AND STANDARD DEVIATION COMPARISON

CMP	Adaptive	Reciprocal	Logarithm	Cube Root	Square Root	Square	1 SD (%)	2 SD (%)	3 SD (%)
BUN	3.87600	3.81640	3.81200	3.89260	3.85350	3.83470	0	100	100
Sodium	1.68440	1.70170	1.73080	1.69180	1.69950	1.69290	100	100	100
Potassium	0.35428	0.35192	0.35640	0.35407	0.35519	0.35063	100	100	100
Chloride	1.87390	1.87390	1.88650	1.87240	1.87750	1.87330	100	100	100
CO2	2.36950	2.35970	2.33080	2.35590	2.36650	2.34840	100	100	100
Glucose	17.15100	17.28800	17.42600	16.95600	17.48600	17.04200	17	100	100
Creatinine	0.15066	0.15288	0.15198	0.15080	0.14731	0.15144	100	100	100
Calcium	0.38162	0.37754	0.37489	0.37583	0.37517	0.36892	100	100	100
Anion Gap	1.55210	1.54110	1.52900	1.55080	1.65140	1.53420	83	100	100
Albumin	0.25991	0.25779	0.25774	0.25949	0.26071	0.26115	100	100	100
Alkaline Phosphatase	22.74900	22.71500	23.14800	22.84200	23.03900	22.63000	50	100	100
AST	9.75170	9.68430	9.79200	9.73460	9.74890	9.75550	17	100	100
ALT	11.81000	11.87100	11.78500	11.88900	11.86500	11.97600	17	100	100
Bilirubin Total	0.32360	0.32175	0.32122	0.32470	0.31925	0.32078	0	100	100
Protein Total	0.41976	0.42361	0.42005	0.42747	0.42064	0.42293	0	100	100
Standard Deviation Total							59	100	100

Table 19. Adaptive binary input transform error and standard deviation distribution (n=90)

TABLE XX

OTSU THRESHOLD REGRESSION MODEL TYPE AND ROOT MEAN SQUARED ERROR

CMP	Otsu	RMSE	Reciprocal	RMSE	Logarithm	RMSE	Cube Root	RMSE	Square Root	RMSE	Square	RMSE
BUN	LR	3.84910	SVM	3.84410	SVM	3.98130	SVM	3.85030	SVM	3.84550	SVM	3.82650
Sodium	GPR	1.78070	GPR	1.78590	Ensemble	1.74020	GPR	1.76640	LR	1.79600	LR	1.75970
Potassium	SVM	0.35473	SVM	0.35176	SVM	0.35003	Tree	0.35232	SVM	0.34870	LR	0.35121
Chloride	SVM	1.87370	SVM	1.87390	LR	1.92680	SVM	1.89280	Tree	1.82260	SVM	1.90510
CO2	LR	2.39680	SVM	2.35510	Tree	2.40490	Tree	2.39600	LR	2.39110	LR	2.40680
Glucose	SVM	17.00000	LR	17.08200	GPR	17.07200	Ensemble	16.91000	LR	17.43200	SVM	16.86200
Creatinine	GPR	0.15155	GPR	0.15046	LR	0.15052	GPR	0.15183	GPR	0.14827	Tree	0.14885
Calcium	LR	0.37566	LR	0.37826	GPR	0.37877	LR	0.37588	GPR	0.37467	LR	0.38395
Anion Gap	SVM	1.59190	GPR	1.56680	GPR	1.58040	LR	1.57160	LR	1.58770	SVM	1.56330
Albumin	LR	0.25798	LR	0.25740	LR	0.25825	LR	0.25820	LR	0.25734	Tree	0.26336
Alkaline Phosphatase	SVM	22.89800	Tree	23.20300	LR	22.75500	SVM	22.99000	GPR	22.72500	LR	22.93300
AST	SVM	9.65880	GPR	9.72960	LR	9.64730	GPR	9.67730	SVM	9.75140	LR	9.70550
ALT	LR	11.98500	SVM	12.04800	LR	11.90400	LR	11.81900	GPR	11.86700	LR	11.93100
Bilirubin Total	LR	0.32307	LR	0.32426	LR	0.32261	Ensemble	0.31318	Tree	0.31169	Tree	0.31298
Protein Total	SVM	0.41149	SVM	0.41991	GPR	0.42024	SVM	0.42587	GPR	0.41935	SVM	0.42407

Table 20. Otsu binary input transform regression model error (n=90)

TABLE XXI

OTSU THRESHOLD ROOT MEAN SQUARED ERROR AND STANDARD DEVIATION COMPARISON

CMP	Otsu	Reciprocal	Logarithm	Cube Root	Square Root	Square	1 SD (%)	2 SD (%)	3 SD (%)
BUN	3.84910	3.84410	3.98130	3.85030	3.84550	3.82650	0	100	100
Sodium	1.78070	1.78590	1.74020	1.76640	1.79600	1.75970	100	100	100
Potassium	0.35473	0.35176	0.35003	0.35232	0.34870	0.35121	100	100	100
Chloride	1.87370	1.87390	1.92680	1.89280	1.82260	1.90510	67	100	100
CO2	2.39680	2.35510	2.40490	2.39600	2.39110	2.40680	67	100	100
Glucose	17.00000	17.08200	17.07200	16.91000	17.43200	16.86200	33	100	100
Creatinine	0.15155	0.15046	0.15052	0.15183	0.14827	0.14885	100	100	100
Calcium	0.37566	0.37826	0.37877	0.37588	0.37467	0.38395	100	100	100
Anion Gap	1.59190	1.56680	1.58040	1.57160	1.58770	1.56330	100	100	100
Albumin	0.25798	0.25740	0.25825	0.25820	0.25734	0.26336	100	100	100
Alkaline Phosphatase	22.89800	23.20300	22.75500	22.99000	22.72500	22.93300	33	100	100
AST	9.65880	9.72960	9.64730	9.67730	9.75140	9.70550	50	100	100
ALT	11.98500	12.04800	11.90400	11.81900	11.86700	11.93100	0	100	100
Bilirubin Total	0.32307	0.32426	0.32261	0.31318	0.31169	0.31298	0	100	100
Protein Total	0.41149	0.41991	0.42024	0.42587	0.41935	0.42407	0	100	100
Standard Deviation Total							57	100	100

Table 21. Otsu binary input transform error and standard deviation distribution (n=90)

5. DISCUSSION

The machine learning approach considers the average grayscale image texture values, given 100-200 frames per sample. The analysis performs the GLCM on each image in the sample and averages the values to generate the six spectral feature variables and their corresponding values. Subsequently, the approach employs an artificial neural network to train a predictive model with the average grayscale texture values as the input variables with known CMP data as output variables. This method provides a comprehensive analysis to generate a predictive model capable of predicting CMP outcomes, given a different set of input values. NICMP predictive model *beta* produces an accuracy level of 20%, given the predictive model MSE is within 80% of the CMP reference values. NICMP predictive model *one* produces a 95% accuracy level since the MSE is within 5%, relative to the reference values. Table 21 displays the FDA's accuracy key with respect to self-monitoring blood glucose test systems as a point of reference [55]. The NI glucose measurement average error is five mg/dL (+/-5%), relative to the laboratory result. The NICMP average error is two units (+/-5%), relative to the laboratory metabolic blood panel result. The NICMP predictive model *one* coefficient of determination is 0.9 which suggests that the spectral data altogether explains 90% of the variations in the output value. Additionally, the accuracy level increases faster with subsequent training data, perhaps exponentially, relative to the increase of training data. The NICMP predictive model *beta* training data set includes 80% of the total available data, or 72 endpoints, while predictive model *one* includes 95% of the available data, or 85 endpoints. This 15% increase in the training data set accounts for a 75% increase in accuracy, relative to the test/target data set. Moreover, the ratio and distribution of positive and negative values in each of the corresponding covariance and correlation coefficient matrices are equivalent, given a cross-sectional approach (i.e., sample covariance and population correlation coefficient).

The average correlation coefficient for each of the CMP results and NICMP predictive model outputs are very close to 0 which implies that interrelationships between each metabolic parameter does not exist. This analysis is expected with regards to the CMP blood test as different reagents are used to detect the various metabolic analytes. The machine learning and digital image processing technique proves to decouple the respective analyte concentrations, given a single input (i.e., grayscale image intensity value). Moreover, the concentration of any one particular analyte does not influence image intensity values in such a way that could affect the concentration prediction, or outcome, of another analyte with respect to machine learning. This effect might be partly attributed to each metabolic analyte being assigned a corresponding predictive model that is independent, relative to the predictive models of the other analytes. In other words, the NICMP predictive model actually contains separate neural networks that describes the relationship between the spectral parameter and the metabolic analyte of interest. This approach is similar to a certain reagent being used to detect the presence and concentration of a particular analyte (i.e., one reagent can not detect multiple analytes). Each analyte has a certain reagent that is useful for detecting that particular analyte, given a blood sample. In the case of non-invasive detection, each analyte has a certain predictive model used to detect its concentration. Efficiency is created as multiple neural networks, one for each analyte, can detect the concentration of each particular analyte with a single grayscale spectral image, and eliminates the need for several reagents.

TABLE XXII

FDA ACCURACY KEY FOR SELF-MONITORING BLOOD GLUCOSE SYSTEMS

Accuracy key	**Percentages listed are meter result as compared to laboratory results**
Accurate Results	Meter result is +/-15% of laboratory result
More Accurate Results	Meter result is +/-10% of laboratory result
Most Accurate Results	Meter result is +/-5% of laboratory result

Table 22. Qualitative accuracy description for over-the counter blood glucose systems relative to laboratory results

Binary conversion and transformation is useful to further analyze the relationship between the spectral image and CMP data. One image was taken from the 100-200 images per sample, from each sample, to convert the grayscale image intensity to a binary value. The binary value undergoes transformation to analyze the change in the relationship, given multiple types of data transform. The binary values along with their corresponding transformations serve as input variables in regression modeling techniques with the CMP data as the output variables. The regression learner application develops models through a series of different methods to generate the minimal error. The error is useful to determine the distribution with respect to the binary conversion, given only one image per sample. This analysis considers the fundamental, or underlying, relationship to substantiate the machine learning predictive model which considers an average of 100-200 grayscale images. In accordance to the empirical rule (68-95-99.7), the average binary error distribution is normal since 67% of the data is within one standard deviation, and 100% within 2 standard deviations. The machine learning predictions are reliable because the underlying error distribution is normal.

The spectral images represent relative RBC mean and velocity. The CMP is a function of RBC volume and velocity, since a correlation exists between metabolic analyte concentration and the spectral images. This suggests that certain metabolic analyte concentration affects RBC production factors (e.g. erythropoietin), influences physiological states that relate to blood pressure, and other factors that relate to RBC velocity (e.g. nitric oxide).

6. CONCLUSION AND FUTURE WORK

Spectroscopy, specifically LSCI, and machine learning are useful to remotely detect metabolic analyte concentration. The predictive model coefficient of determination proves that a significant relationship between the spectral Doppler signal and chemical concentration in the blood exists. The overall contribution includes the introduction of the innovative approach with regards to the application of machine learning to include subjects as their own control, relative to the predictive model development. Subsequently, the novel method enables the non-invasive capability to detect analyte concentration. This research and methodology serves to contribute to an important area of research that has proven to be extremely challenging. Additionally, the method is novel in the sense that it is applicable to other clinical testing applications, thus enabling diverse and potentially continuous detection medical applications to remotely sense biological parameters relevant to clinical evaluation. The next generation version should include a digital image monitor to ensure sufficient pressure is applied on the optical sensor by the subject to capture consistent spectral data, a correlation coefficient analysis including the entire data set, and a spectral reading with both palms to assess the predictive model performance with regards to precision. Additionally, digital image pre-processing might be applicable to enhance the grayscale spectral images to further improve reproducibility. Future work includes applying the method to

certain clinical tests that require needles and venipuncture blood draws (i.e., continuous blood pressure monitoring, thyroid hormone stimulating, cholesterol, etc.). The NICMP serves as a platform technology, and potentially a predicate device with regards to regulatory approval. Future work also includes machine deep learning to extract certain image texture features to generate a more accurate and precise model by eliminating or reducing multicollinearity. The current predictive model considers six grayscale texture feature variables; which all six feature variables are predictors in the machine learning training process. Interference as a result of predictors correlating with each other can inhibit the accuracy and performance of the predictive model. Additionally, this research considers one to two seconds of blood perfusion with a relatively small sample size (i.e. proof of concept). Subsequent releases of the application should consider at least three to four seconds of microvascular perfusion to train and develop next generation predictive models, and a larger sample size. The particular enhancement regarding perfusion time would consider three to four cycles of microvascular perfusion instead of current one to two cycles, given an average resting heart rate of 60 beats per minute. This enhancement provides more relevant data to train a commercial version predictive model. The predictive model accuracy, precision, and reliability are subject to increase, given the enhancements. Moreover, future statistical analysis ought to include an error distribution analysis that considers the standard deviation of the population, NI glucose measurement response plot via an Error Grid, and error plots via Bland-Altman plot to determine the bias and limits of agreement. Limitations include a stationary device with an analysis on the palm of either hand due to the data collection method. This limitation may be overcome and provide a portable sensor (e.g. smartwatch) by including a gamma parameter to consider differences in constant spectral values between the initial region of interest and other areas such as the wrist. Additionally, previous research indicates that spectral device training data

from a particular sample are typically able to produce accurate results with test data that share similar characteristics as the training data. In this case, another limitation is that the NICMP results are valid only with a “healthy” population. Future releases should contain training data that is more representative of the general population. One study indicates that 95% of the world’s population has health problems, with over a third having more than five ailments [56]. Subsequent versions should collect data from a diagnosed population to be more representative of the global population and eliminate the limitation regarding accurate results, relative to a group with similar characteristics as the training data set.

7. REFERENCES

[1] A. J. |. Bandodkar Joseph, "Non-invasive wearable electrochemical sensors: a review," *Trends in Biotechnology*, vol. 32, *(7)*, pp. 363-371, 2014. Available: https://www.clinicalkey.es/playcontent/1-s2.0-S0167779914000699.

[2] A. Raluca Maria, S. Pasca and R. Strungaru, "Heart rate monitoring by using non-invasive wearable sensor," in Jun 2017, pp. 587-590.

[3] A. Mehta, "Increase compute power to enable AI," vol. 2018, *(Nov 20,)*, 2018. Available: https://inform.tmforum.org/data-analytics-and-ai/2018/03/36883/.

[4] Anonymous "Comprehensive Metabolic Panel (CMP) Testing," vol. 2018, *(Nov 3,)*, .

[5] Anonymous "Comprehensive Metabolic Panel (CMP) Definition," vol. 2018, *(Nov 3,)*, Available: https://aidsinfo.nih.gov/understanding-hiv-aids/glossary/2992/comprehensive-metabolic-panel.

[6] HHS OIG DATA BRIEF, "Department of Health and Human Services OFFICE OF INSPECTOR GENERAL," .

[7] Anonymous "Aging populations are a captive market for the medical device industry," vol. 2018, *(Nov 3,)*, .

[8] S. Majumder, T. Mondal, and M. J. Deen, “Wearable Sensors for Remote Health Monitoring,” vol. 17, no. 1, p. 130, Jan. 2017.

[9] A. J. Bandodkar, W. Jia and J. Wang, "Tattoo-Based Wearable Electrochemical Devices: A Review," *Electroanalysis*, vol. 27, *(3)*, pp. 562-572, 2015. Available: https://onlinelibrary.wiley.com/doi/abs/10.1002/elan.201400537.

[10] T. Lin, "Non-Invasive Glucose Monitoring: A Review of Challenges and Recent Advances," *Current Trends in Biomedical Engineering & Biosciences*, vol. 6, *(5)*, 2017.

[11] F. B. Hu, A. Satija and J. E. Manson, "Curbing the diabetes pandemic," *JAMA, the Journal of the American Medical Association,* vol. 313, *(23),* pp. 2319, 2015. Available: https://www.ncbi.nlm.nih.gov/pmc/articles/PMC5291074/.

[12] Anonymous "What is Diabetes? | NIDDK," vol. 2018, *(Nov 21,),* Available: https://www.niddk.nih.gov/health-information/diabetes/overview/what-is-diabetes.

[13] B. C. Wilson, M. Jermyn and F. Leblond, "Challenges and opportunities in clinical translation of biomedical optical spectroscopy and imaging," *J Biomed Opt,* vol. 23, *(3),* pp. 1-13, 2018.

[14] A. Ciudin, C. Hernandez and R. Simo, "Non-invasive methods of glucose measurement: current status and future perspectives," *Current Diabetes Reviews,* vol. 8, *(1),* pp. 48, 2012. Available: https://www.ncbi.nlm.nih.gov/pubmed/22414058.

[15] E. B. Hanlon, R. Manoharan, T. W. Koo, K. E. Shafer, J. T. Motz, M. Fitzmaurice, J. R. Kramer, I. Itzkan, R. R. Dasari and M. S. Feld, "Prospects for in vivo Raman spectroscopy," *Phys Med Biol,* vol. 45, *(2),* pp. 1, 2000.

[16] P. G. Steffes, "Laser-based measurement of glucose in the ocular aqueous humor: an efficacious portal for determination of serum glucose levels," *Diabetes Technol. Ther.,* vol. 1, *(2),* pp. 129-133, 1999.

[17] M. S. Borchert, M. C. Storrie-Lombardi and J. L. Lambert, "A noninvasive glucose monitor: preliminary results in rabbits," *Diabetes Technol. Ther.,* vol. 1, *(2),* pp. 145-151, 1999.

[18] J. Lipson, J. Bernhardt, U. Block, W. R. Freeman, R. Hofmeister, M. Hristakeva, T. Lenosky, R. McNamara, D. Petrasek, D. Veltkamp and S. Waydo, "Requirements for

calibration in noninvasive glucose monitoring by Raman spectroscopy," *J Diabetes Sci Technol*, vol. 3, *(2)*, pp. 233-241, 2009.

[19] M. R. Riley, M. Rhiel, X. Zhou, M. A. Arnold and D. W. Murhammer, "Simultaneous measurement of glucose and glutamine in insect cell culture media by near infrared spectroscopy," *Biotechnol. Bioeng.*, vol. 55, *(1)*, pp. 11-15, 1997.

[20] M. R. Riley, M. A. Arnold, D. W. Murhammer, E. L. Walls and N. DelaCruz, "Adaptive calibration scheme for quantification of nutrients and byproducts in insect cell bioreactors by near-infrared spectroscopy," *Biotechnol. Prog.*, vol. 14, *(3)*, pp. 527-533, 1998.

[21] M. A. Arnold and G. W. Small, "Determination of physiological levels of glucose in an aqueous matrix with digitally filtered Fourier transform near-infrared spectra," *Anal. Chem.*, vol. 62, *(14)*, pp. 1457-1464, 1990.

[22] G. Lu, X. Zhou, M. A. Arnold and G. W. Small, "Multivariate Calibration Models Based on the Direct Analysis of Near-Infrared Single-Beam Spectra," *Appl. Spectrosc. , AS*, vol. 51, *(9)*, pp. 1330-1339, 1997.
Available: https://www.osapublishing.org/as/abstract.cfm?uri=as-51-9-1330.

[23] M. J. McShane, G. L. Cote and C. Spiegelman, "Variable Selection in Multivariate Calibration of a Spectroscopic Glucose Sensor," *Appl. Spectrosc. , AS*, vol. 51, *(10)*, pp. 1559-1564, 1997. Available: https://www.osapublishing.org/as/abstract.cfm?uri=as-51-10-1559.

[24] L. Heinemann, "Glucose Sensors: Current Status and Further Developments," *IFAC Proceedings Volumes*, vol. 33, *(3)*, pp. 23-29, 2000.
Available: https://www.sciencedirect.com/science/article/pii/S1474667017354836.

[25] S. Saha, H. Cano-Garcia, I. Sotiriou, O. Lipscombe, I. Gouzouasis, M. Koutsoupidou, G. Palikaras, R. Mackenzie, T. Reeve, P. Kosmas and E. Kallos, "A Glucose Sensing System Based on Transmission Measurements at Millimetre Waves using Micro strip Patch Antennas," *Scientific Reports,* vol. 7, *(1),* pp. 6855-11, 2017. Available: https://www.ncbi.nlm.nih.gov/pubmed/28761121.

[26] K. Humphreys, C. Markham and T. E. Ward, "A CMOS camera-based system for clinical photoplethysmographic applications," in 2005/06/01, pp. 88-96Available: https://www.spiedigitallibrary.org/conference-proceedings-of-spie/5823/0000/A-CMOS-camera-based-system-for-clinical-photoplethysmographic-applications/10.1117/12.604822.short.

[27] A. Thomas, L. Heinemann, A. Ramírez and A. Zehe, "Options for the Development of Noninvasive Glucose Monitoring," *J Diabetes Sci Technol,* vol. 10, *(3),* pp. 782-789, 2015. Available: https://www.ncbi.nlm.nih.gov/pmc/articles/PMC5038528/.

[28] Nurul Akmal Binti Abd Salam, Wira Hidayat bin Mohd Saad, Zahariah Binti Manap and Fauziyah bte Salehuddin, "The Evolution of Non-invasive Blood Glucose Monitoring System for Personal Application," vol. 8, .

[29] S. K. Vashist, "Non-invasive glucose monitoring technology in diabetes management: A review," *Analytica Chimica Acta,* vol. 750, pp. 16-27, 2012. Available: https://www.sciencedirect.com/science/article/pii/S0003267012004606.

[30] Anonymous "Spectroscopy | science," vol. 2018, *(Nov 24,),* Available: https://www.britannica.com/science/spectroscopy.

[31] B. Dr. Mattson, J. D. Myers and P. Newman, "What Do Spectra Tells Us?" *(Nov 28, 2018),* May 5, 2016.

[32] B. Dr. Mattson, J. D. Myers and P. Newman, "What is Spectroscopy?" *(Nov 28, 2018)*, Mar 8, 2017.

[33] Anonymous "MRI (magnetic resonance imaging)," vol. 2018, *(Nov 24,)*, Available: http://www.mayfieldclinic.com/pe-mrspectroscopy.htm.

[34] J. Micheels, B. Alsbjorn and B. Sorensen, "Laser doppler flowmetry. A new non-invasive measurement of microcirculation in intensive care?" *Resuscitation*, vol. 12, *(1)*, pp. 31-39, 1984.

[35] D. H. Park, J. W. Hwang, K. S. Jang, D. G. Han, K. Y. Ahn and B. S. Baik, "Use of laser Doppler flowmetry for estimation of the depth of burns." *Plast Reconstr Surg*, vol. 101, *(6)*, pp. 1516-1523, 1998. Available: http://europepmc.org/abstract/med/9583481.

[36] M. Leutenegger, E. Martin-Williams, P. Harbi, T. Thacher, W. Raffoul, M. André, A. Lopez, P. Lasser and T. Lasser, "Real-time full field laser Doppler imaging," *Biomedical Optics Express*, vol. 2, *(6)*, pp. 1470-1477, 2011. Available: https://www.ncbi.nlm.nih.gov/pubmed/21698011.

[37] G. Michelson, B. Schmauss, M. J. Langhans, J. Harazny and M. J. Groh, "Principle, validity, and reliability of scanning laser Doppler flowmetry," *J. Glaucoma*, vol. 5, *(2)*, pp. 99-105, 1996.

[38] S. Eriksson, J. Nilsson and C. Sturesson, "Non-invasive imaging of microcirculation: a technology review," *Medical Devices (Auckland, N.Z.)*, vol. 7, pp. 445-452, 2014. Available: https://www.ncbi.nlm.nih.gov/pubmed/25525397.

[39] D. A. Boas and A. K. Dunn, "Laser speckle contrast imaging in biomedical optics," *Journal of Biomedical Optics*, vol. 15, *(1)*, pp. 011109, 2010. Available: http://dx.doi.org/10.1117/1.3285504.

[40] M. Roustit, C. Millet, S. Blaise, B. Dufournet and J. L. Cracowski, "Excellent reproducibility of laser speckle contrast imaging to assess skin microvascular reactivity," *Microvasc. Res.*, vol. 80, *(3)*, pp. 505-511, 2010.

[41] N. Houreld and H. Abrahamse, "Laser light influences cellular viability and proliferation in diabetic-wounded fibroblast cells in a dose- and wavelength-dependent manner," *Lasers Med Sci*, vol. 23, *(1)*, pp. 11-18, 2008. Available: https://www.ncbi.nlm.nih.gov/pubmed/17361392.

[42] L. M. Richards, S. M. S. Kazmi, J. L. Davis, K. E. Olin and A. K. Dunn, "Low-cost laser speckle contrast imaging of blood flow using a webcam," *Biomedical Optics Express*, vol. 4, *(10)*, pp. 2269, 2013. Available: https://www.ncbi.nlm.nih.gov/pubmed/24156082.

[43] Anonymous "Laser Doppler Imaging - Perimed AB," vol. 2018, *(Dec 7,)*, Available: https://www.perimed-instruments.com/laser-doppler-imaging.

[44] S. B. Kotsiantis, "Supervised machine learning: a review of classification techniques," Jan 1, 2007.

[45] R. M. Haralick, K. Shanmugam and I. Dinstein, "Textural Features for Image Classification," *T-Smc*, vol. SMC-3, *(6)*, pp. 610-621, 1973. Available: https://ieeexplore.ieee.org/document/4309314.

[46] G. Preethi and V. Sornagopal, "MRI image classification using GLCM texture features," in Mar 2014, pp. 1-6.

[47] Bradley, D., G. Roth, "Adapting Thresholding Using the Integral Image," *Journal of Graphics Tools*. Vol. 12, No. 2, 2007, pp.13-21.

[48] Otsu, N., "A Threshold Selection Method from Gray-Level Histograms," *IEEE Transactions on Systems, Man, and Cybernetics*, Vol. 9, No. 1, 1979, pp. 62-66.

[49] S. Agatonovic-Kustrin and R. Beresford, "Basic concepts of artificial neural network (ANN) modeling and its application in pharmaceutical research," *Journal of Pharmaceutical and Biomedical Analysis*, vol. 22, *(5)*, pp. 717-727, 2000.

[50] Hang Xie, Hao Tang and Yu-He Liao, "Time series prediction based on NARX neural networks: An advanced approach," in Jul 2009, pp. 1275-1279.

[51] F. Dan Foresee and M. T. Hagan, "Gauss-newton approximation to bayesian learning," in 1997, pp. 1935 vol.3.

[52] David J. C. MacKay, "Bayesian Interpolation," *Neural Computation*, vol. 4, *(3)*, pp. 415-447, Available: http://www.mitpressjournals.org/doi/abs/10.1162/neco.1992.4.3.415.

[53] S. Manikandan, "Data transformation," *J Pharmacol Pharmacother*, vol. 1, *(2)*, pp. 126-127, 2010. Available: https://www.ncbi.nlm.nih.gov/pmc/articles/PMC3043340/.

[54] M. B. Editor, "How Important Are Normal Residuals in Regression Analysis?" vol. 2019, *(Jan 5,)*, Available: http://blog.minitab.com/blog/adventures-in-statistics-2/how-important-are-normal-residuals-in-regression-analysis.

[55] Anonymous "Self-monitoring blood glucose test systems for over-the-counter use; guidance for industry and food and drug administration staff; availability," Federal Information & News Dispatch, Inc, Washington, Tech. Rep. 81, Oct 11,. 2016. Available: https://www.fda.gov/downloads/medicaldevices/deviceregulationandguidance/guidancedocuments/ucm380327.pdf

[56] Anonymous "Over 95% of the world's population has health problems, with over a third having more than five ailments," vol. 2019, *(Jan 14,)*, Available: https://www.sciencedaily.com/releases/2015/06/150608081753.htm.